NTNU

Norwegian University of
Science and Technology

Compatibility Study of Carbon-Based Refractory Materials utilized in Silicomanganese Production Furnaces

Håvard Mølnås

Chemical Engineering and Biotechnology
Submission date: July 2011
Supervisor: Merete Tangstad, IMTE
Co-supervisor: Joalet Steenkamp, University of Pretoria

Norwegian University of Science and Technology
Department of Materials Science and Engineering

I hereby declare that this work has been carried out independently and in compliance with the examination regulations of the Norwegian University of Science and Technology, NTNU.

_____

Håvard Mølnås

Trondheim/Pretoria, July 2011

Preface

This report describes an investigation of tap hole refractory compatibility with process materials in an industrial silicomanganese furnace. It is the author's master thesis and serves as main evaluation basis for the course TMT4900 at the Norwegian University of Science and Technology, NTNU. The work was performed at the Department of Materials Science and Metallurgical Engineering, University of Pretoria, and some analyses were done at the Department of Geology and at external laboratories in Pretoria, South Africa.

First of all, I would like to thank my supervisor at NTNU, Professor Merete Tangstad, for introducing me to the world of manganese and for making my stay at the University of Pretoria, South Africa, possible. Her interest and excitement for manganese production is highly contagious and has motivated and inspired me throughout the past two years. Secondly, I am very grateful for the time and effort put forth by my supervisor at University of Pretoria, Senior lecturer Joalet Steenkamp, making this semester incredibly valuable and rewarding both academically and socially. She has done her outmost to make sure I would get the most out of these six months, far beyond what can be expected of a supervisor. I am truly thankful for everything she has introduced me to, sharing her academic interests as well as her great country with me this spring.

This investigation could not have been conducted without the help of Ph.D. candidate Robert Cromarty. His knowledge on practical matters is highly appreciated.

I would also like to thank Professor JPR de Villiers for input regarding experimental conditions and help interpreting results, Carel Coetzee for assistance with the SEM, Ph.D. candidate Teresa van den Berg for help with p_{O2} measurements, Jacques Müller for providing slag viscosity data and advice regarding Factsage™ calculations, Jacob Tsotetsi for assistance during gas calibrations and Neani Rambuda for help with logistics.

Last but not least I would like to thank students and staff at Department of Materials Science and Metallurgical Engineering, University of Pretoria, for their hospitality and interest. I felt very welcome from the day I arrived, and I highly appreciate the many valuable discussions we have had throughout this semester in South Africa.

Trondheim/Pretoria, July 2011

Håvard Mølnås

Abstract

Tap hole refractories constitute critical parts of the refractory lining in submerged arc furnaces. For several hours every day, molten slag and metal flow through the tap hole calling for thorough selection of refractory materials able to withstand the intense thermal, corrosive and erosive conditions present in this area. Carbon-based refractories have shown excellent thermal properties and high strength, as well as low wettability towards process materials, and are therefore utilized in silicomanganese production furnaces both as side lining, in the hearth, and in the tap hole area.

The aim of this investigation was to determine the compatibility of five refractory materials utilized in the tap hole area of an industrial silicomanganese furnace with two industrial silicomanganese slags:

- Investigate the suitability of the selected refractory materials for confining the process materials during industrial production of silicomanganese alloys.

- Identify critical refractory wear mechanisms upon slag-refractory interaction at industrial tapping temperatures.

Compatibilities were investigated through 12 static crucible tests and two static plate tests in a vertical tube furnace redesigned during this investigation. Slag-refractory interaction was studied after two and four hours holding time at 1367°C ± 1.8°C, 1464°C ± 2.1°C and 1600°C - 0.6°C /+ 0.2°C. Holding temperatures were verified through the wire-bridge method at the melting points of gold and palladium. Visual inspection, as well as optical microscopy and SEM, were utilized to examine the samples after heat treatment.

During compatibility experiments, dissolution of refractory matrix due to solubility of oxide refractory binder phases in silicomanganese slags was observed, as well as disintegration of refractory particles due to gas formation at slag-refractory interface, or expansion as a result of phase transformations in refractory material. Direct reduction of manganese oxide from slags and iron oxide present in refractories by carbon and silicon carbide was also observed. Establishment of partial slag-metal equilibriums between iron oxide and silicon metal originally present in slag was observed, as well as formation of silicon carbide at the slag-refractory interfaces. The latter may serve to protect the refractory from wear caused by slags.

Based on observations of extensive interaction between silicomanganese slag sample I and ramming paste at 1600°C, the ramming paste investigated cannot be recommended for usage during tap block repair in an industrial silicomanganese furnace. Incipient electrode paste disintegration by slags and silicon carbide tap block – slag interaction were observed after compatibility tests at 1464°C, calling for further investigations of these refractory materials. Tap hole clay and carbon tap block showed minimal signs of interaction with process materials at 1464°C.

Refractory porosity seemed to have a larger effect on refractory wear than refractory ash content. Contrary to industrial observations, silicomanganese slag sample I was more corrosive towards the ramming paste and electrode paste investigated than silicomanganese slag sample II.

List of figures

List of tables

Table of Contents

1. Introduction

1.1 Background

Silicomanganese, SiMn, is produced in circular, stationary and closed three-phase submerged-arc furnaces typically in the range 15 – 40 MW[1,2]. The alloy is utilized in steelmaking, both as alloying elements and as a deoxidizer and desulfurizer. In 2008, a total of 7.85 million metric tons of SiMn was produced[3].

Two main principles are utilized for the refractory lining of industrial SiMn production furnaces[4]: The insulating lining concept has traditionally been the producer's first choice, but since 1995, the freeze lining concept has gained industrial acceptance[5].

Selection of refractories should be based on scientific testing of relevant refractory materials as well as previous experience. Preferably, post mortem studies of refractories exposed to actual industrial conditions should be conducted[6]. The most dominant refractory wear mechanisms in submerged-arc furnaces are chemical wear, thermal stress and erosion[5]. In addition to well-founded selection of refractory materials, correct installation procedures and tapping routines need to be utilized in order to obtain as extensive refractory lifetime as possible[6]. Excessive oxygen lancing during tapping generates high temperatures above the sintering temperatures of the refractory materials, which will affect the structures and can lead to failure.

Tap hole refractories constitute the most critical part of the refractory lining in a SiMn furnace. For several hours every day, molten slag and metal flow through the tap hole calling for thorough selection and utilization of refractory materials able to withstand the intense thermal, corrosive and erosive conditions present in this area. Improper material selection can, and will in most cases, lead to premature refractory failure, possibly causing fatalities, severe material damage and major economic losses.

Carbon-based refractories have shown excellent thermal properties, high strength and low wettability towards process materials, and can be utilized in SiMn furnaces both as side lining and in the hearth. Silicon carbide, SiC, has been proven especially suitable for use as tap block material.

Several different tests can be utilized for refractory wear testing, both stationary and dynamic[7,8]. Selection of test(s) depends on sample properties, level of accuracy required and equipment available. Additionally, available time, ease of test conduction and funding should also be taken into account.

1.2 Aim of the investigation

The entry point of this thesis is a situation taking place in an industrial SiMn furnace: As a result of the recent economic crisis, the furnace was shut down for five weeks. During start-up, lancing was utilized to tap metal and slag from one of the tap holes, causing damage to the refractory lining. In the following year, this specific tap hole was repaired three times, while the other furnace tap hole has so far survived 15 years without a burn-through. The latter is believed to be a result of good maintenance practice.

The aim of this investigation is to determine the compatibility of five refractory materials utilized in the tap hole area of an industrial SiMn furnace with two SiMn slags:

- How suitable are the different refractory materials for confining the process materials during industrial production of SiMn alloys?

- Which refractory wear mechanisms are dominant?

Compatibilities will be investigated through 12 crucible tests and two static plate tests, mainly examining the effects of chemical wear and structural spalling on the refractories by industrial slag samples at industrial tapping temperatures. After heat treatment, macroscopic wear will be quantified visually, followed by microscopic inspection of selected areas using optical microscopy and SEM.

A critical aspect prior to experimental start-up will be to design and develop a furnace tube setup suitable for refractory testing. At the beginning of the investigation, the Carbolite PVT 18/80 vertical tube furnace intended for use is not operational, calling for imminent repair and redesign of furnace tube fittings. This will be done in close cooperation with furnace supplier and metal workshops.

2. Theory

2.1 Manganese – the anonymous element

Manganese, Mn, is the 12th most abundant element in the earth's crust with a concentration of nearly 0.1% by weight[1]. Although Mn is of great importance in today's society, the element's existence seems only to be known by a relatively small group directly involved in Mn production or in research involving Mn and its compounds. The element's properties have been exploited for thousands of years, but commercial production of Mn alloys only commenced following the establishment of Mn as a separate element in 1774.

2.1.1 Origin

Manganese can be found in more than 300 minerals, although only a few of them have sufficient Mn-content to be used in industrial production[1]. Of these, sedimentary oxide, hydroxide or carbonate deposits are most common. The richest land-based deposits consist of oxides such as:

- Braunite - $3(Mn,Fe)_2O_3 \cdot MnSiO_3$
- Braunite II - $7(Mn,Fe)_2O_3 \cdot CaSiO_3$
- Bixbyite - $(Mn,Fe)_2O_3$
- Hausmannite - $(Mn,Fe)_3O_4$
- Pyrolusite - MnO_2

Ores containing 35 - 50% Mn are classified as metallurgical ores[1], while ferruginous ores have Mn-content from 15 - 35%. Ferruginous ores also have high iron concentrations. Iron ores carrying 5 - 10% Mn are classified as manganiferous ores.

Ferromanganese nodules on the seabed of the Pacific Ocean make up the largest reserve on earth[9], carrying as much as 15 - 30% Mn as well as considerable amounts of iron, Fe, copper, Cu, nickel, Ni, and cobalt, Co. Of the world's land-based Mn reserves, 78% can be found in the Kalahari field located in the South African Northern Cape province[1]. South African ores are generally known for their high basicity and low O/Mn and Mn/Fe ratios, as well as low phosphorous, P, levels. Several mines are operated in the Northern Cape, producing metallurgical and ferruginous ores known as Mamatwan and Wessels. In Wessels ore, oxides braunite, braunite II, hausmannite, bixbyite and magnetite, Fe_3O_4, are the main constituents, while Mamatwan ore contains braunite and considerable amounts of carbonates calcite, $CaCO_3$, and dolomite, $CaMg(CO_3)_2$. Mines N'Chwaning and Gloria are also located in the Northern Cape, producing high basicity ores with a high content of carbonatic minerals.

Major Mn-ore producing countries with high grade ores are South Africa, Australia, Brazil and Gabon. China, India, Ukraine, Kazakhstan and Georgia have mines containing lower grade ores. Figure 2.1 shows production estimates for Mn-ore in 2008, presented as thousands of tons Mn-units produced in the respective countries and regions[3].

Africa & the Middle East and China had the highest production of Mn-ore in 2008: Out of the 13.9 million metric tons(MT) of Mn-units produced this year, Africa & the Middle East produced 35.8 %, while China produced 22.1 %. Since China has no high grade ore, the country relies greatly on blending domestic ore with high grade ore imported from other countries.

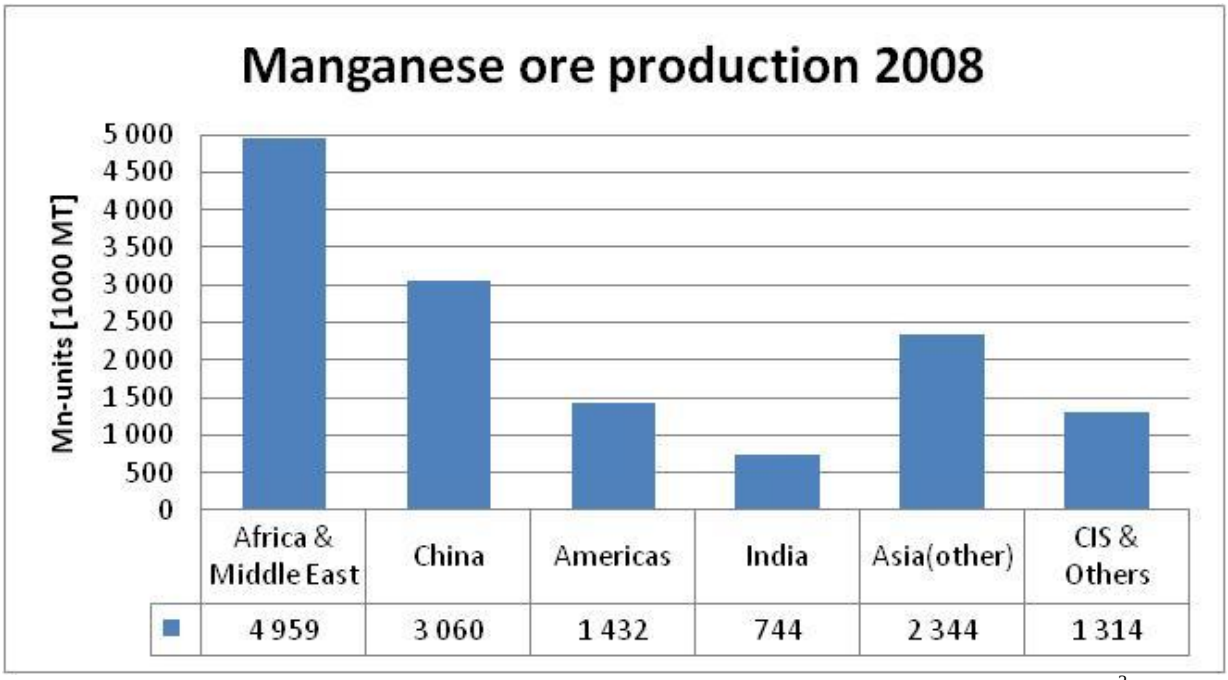

Figure 2.1: Manganese ore production in 2008. From International Manganese Institute[3]

In 2008, China produced 51.0 % of the total world production of Mn-alloys; more than 6.9 million MT out of a total of 13.6 million MT[3]. Figure 2.2 presents production estimates of Mn-alloys in 2008, presented as thousands of tons Mn-alloys silicomanganese, SiMn, refined ferromanganese, FeMn, and high carbon (HC) FeMn produced in the respective countries and regions:

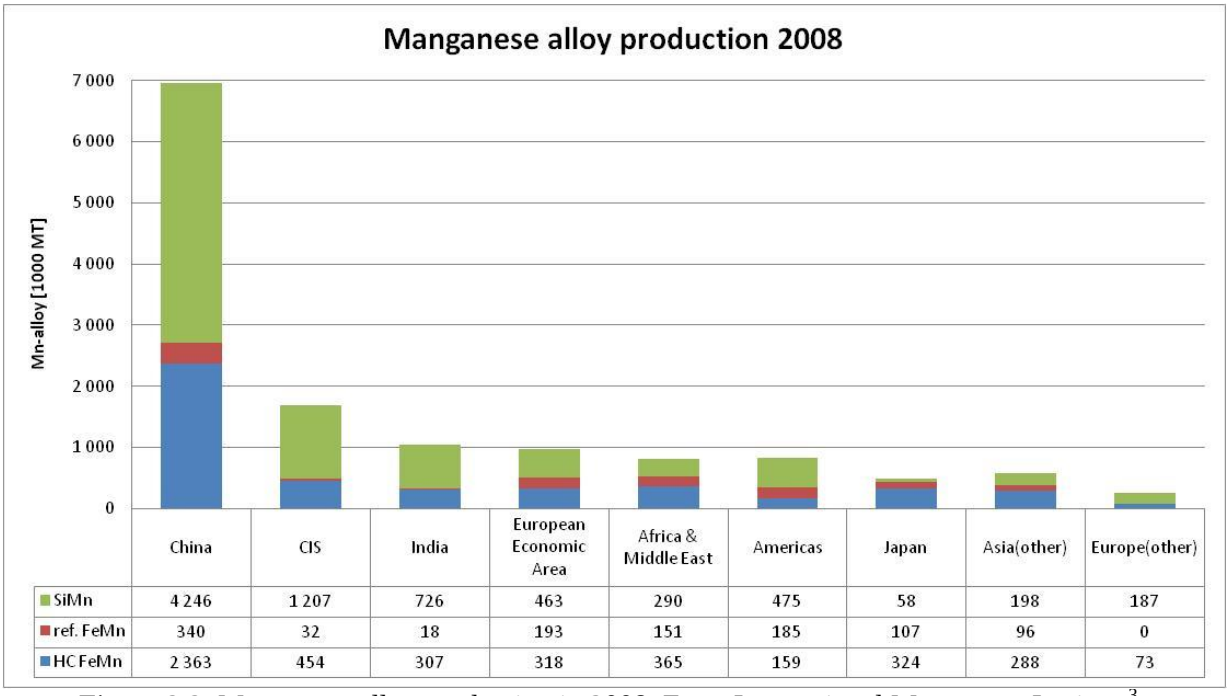

Figure 2.2: Manganese alloy production in 2008. From International Manganese Institute[3]

2.1.2 Utilization

Manganese and manganese oxides, MnO_x, have been in use for several thousand years, starting as pigment for paintings and glassware before the alloying properties of Mn in steel were discovered in ancient Greece. Nowadays, Mn consumption is highly correlated with

steel production, consuming more than 90% of the world Mn production. In 2009, an average gross weight of 10 kg Mn ferroalloys was consumed per metric ton steel produced[10].

Due to the great variety of steels produced, Mn-alloy requirements are different depending on the final product. Both FeMn, and SiMn, can be produced with varying carbon, C, contents: High carbon(HC), medium carbon(MC), low carbon(LC) and ultralow carbon(ULC). As observed in Figure 2.2, 7.85 million MT of the total 13.6 million MT Mn-alloy produced in 2008 was SiMn, 4.65 million MT was HC FeMn and 1.1 million MT was refined FeMn[3]. Table 2.1 shows typical Mn-alloy specifications:

Table 2.1: Typical manganese alloy specifications. From Olsen, Tangstad & Lindstad[1]

Grade	Mn [wt%]	C[wt%]	Si[wt%]	P[wt%]	S[wt%]	B [ppm]
HC FeMn	78	7.5	0.3	0.20	-	-
MC FeMn	80 - 83	1.0 – 1.5	0.6	0.20	-	-
LC FeMn	80 - 83	0.5	0.6	0.20	-	-
SiMn	67 - 68	1.5 – 2.0	17 - 20	0.10 – 0.15	0.02	200
LC SiMn	59 - 63	0.1 – 0.5	25 - 30	0.10	0.01	100
ULC SiMn	58 - 62	0.05	27 - 31	0.05	0.01	100

Approximately 70 % of all Mn added to steel serves as an alloying element increasing strength, toughness and hardness[1]. If special low carbon steels are produced, refined FeMn and SiMn can be utilized, thus avoiding additional decarburizing. The remaining 30 % is added as a deoxidizer and for sulfur, S, removal. According to the Ellingham diagram[11] shown as Figure A.1 in Appendix A.1, Mn is a milder deoxidizer than silicon, Si, but in combination with Si stable manganese silicates, Mn_2SiO_4, are formed[1]. Mn_2SiO_4 coalesces more easily than silicon dioxide, SiO_2, thus separates more easily from the molten steel. Originally, a mixture of HCFeMn and 75% FeSi was added to serve this purpose, but nowadays addition of SiMn is more common. SiMn contains less P, C, aluminum, Al, and nitrogen, N, than the ferromanganese-ferrosilicon mixture, so addition of SiMn results in higher purity as well as increased deoxidizer effectiveness.

During desulfurization of steel utilizing Mn, manganese sulphide, MnS, is formed instead of iron sulphide, FeS. Unlike FeS, MnS does not wet the grain boundaries and has a higher melting point, thereby avoiding metal cracking due to hot shortness[12].

When producing stainless steels, ~1% Mn is normally added, although Mn can completely replace the Ni content, bringing the Mn concentration up to a maximum of ~16 %[1]. Mn will also improve the corrosion resistance of Al and strengthen bronzes. Finally, the element can be utilized in non-metallurgical applications such as the oxidizer and disinfectant potassium permanganate, $KMnO_4$, in chemistry and medicine, respectively, or as MnO_2 in dry cell batteries.

2.1.3 Production of manganese ferroalloys

Manganese ferroalloys can be produced by carbothermic reduction of manganese ore in blast furnaces and electric furnaces. The first commercial production of manganese took place in a blast furnace producing pig iron with 10 – 20% manganese[1]. In 1875, commercial production of ~65 % Mn FeMn started in France, and in 1890 HC FeMn was produced in an electric furnace for the first time. Due to the large amounts of coke required to heat and reduce Mn-ore in the blast furnace as well as high Mn losses in slag and off gasses, electric furnaces have

become increasingly popular. In 2006, 75 % of the world production of Mn-alloys took place in electric furnaces[1]. Electric furnaces will be discussed further in Chapter 2.2.

Two different strategies are utilized when Mn-alloys are produced in an electric furnace[1]: Discard slag practice and high-MnO practice. The former produces HC FeMn and slag with 15 – 20 % MnO, which can be discarded. This process relies on addition of fluxes, and C and electricity consumption is high. Mn-recovery is ~80%. The latter combines FeMn and SiMn production, and is also known as fluxless operation. In the first step, HC FeMn is produced as well as a high-MnO slag with up to 50 % MnO. Secondly, the high-MnO slag is fed along with fresh Mn-ore to a SiMn-furnace in what is known as duplex processing. After SiMn production, the MnO-content of the slag is reduced to ~5%, and the total Mn-recovery can be as high as 95 %.

SiMn production will be the focus for the rest of this thesis. For details on the production of other manganese ferroalloys – *Production of Manganese Ferroalloys* by Olsen, Tangstad and Lindstad[1] provides an extensive practical and theoretical study of Mn production, and is currently the most in-depth publication in this field.

2.1.4 Silicomanganese production

Silicomanganese is produced in electric arc furnaces(EAF) operating in the range 15 – 40 MW giving 80 – 220 ton alloy per day[2]. The feed normally consists of a mixture of slag from HC FeMn production, Mn-ores, quartz and coke – HC FeMn slag consisting typically of oxides MnO, SiO_2, CaO, MgO and Al_2O_3. Some companies[13] feed their furnaces with Mn-ores as the only source of Mn, therefore relying on fluxes to bring the MnO content in the slag to a sufficiently low level. Electric energy is supplied through three graphite electrodes submerged into the charge. Process temperatures in the range 1600 - 1650°C produce on-spec alloy and slag sufficiently low in MnO with a specific power consumption of 3500 – 4500 kWh/ton alloy[2]. Power consumption is majorly affected by Si-content of the alloy and amount of slag produced.

In accordance with Olsen, Tangstad and Lindstad[1], the SiMn furnace can be divided into two areas: Prereduction zone and cokebed zone. In the prereduction zone, the charge is heated through exothermic reactions where higher manganese oxides are reduced to MnO. Reduction takes place in solid state through reaction with CO(g) according to equations (2.1), (2.2) and (2.3):

$$2MnO_2(s) + CO(g) = Mn_2O_3(s) + CO_2(g) \quad (2.1)$$

$$3Mn_2O_3(s) + CO(g) = 2Mn_3O_4(s) + CO_2(g) \quad (2.2)$$

$$Mn_3O_4(s) + CO(g) = 3MnO(s) + CO_2(g) \quad (2.3)$$

At a temperature of ~800°C, the strongly endothermic Boudouard reaction expressed as equation (2.4) becomes significant, and will run simultaneously with the reduction of higher manganese oxides, especially Mn_3O_4. The sum of equations (2.3) and (2.4) shown as equation (2.5) is known as direct reduction and is endothermic.

$$C(s) + CO_2(g) = 2CO(g) \quad (2.4)$$

$$Mn_3O_3(s,l) + C(s) = MnO(s) + CO(g) \quad (2.5)$$

As the temperature increases further downwards in the furnace, melting and mixing of HC FeMn slag and pre-reduced Mn-ore will take place in the temperature range 1250 - 1550°C.

At this stage, the mixture of MnO and SiO_2 will be molten, although separately, both oxides have higher melting points[12]. This can easily be observed from the MnO-SiO_2 phase diagram[14] shown as Figure A.2 in Appendix A.1.

Manganese ores contain alkali oxides, which, according to the Ellingham diagram[11] shown as Figure A.1 in Appendix A.1, will be reduced at high temperatures. Alkali metals such as potassium, K, will vaporize and ascend to the prereduction zone where reaction with CO(g) will take place according to the exothermic reaction shown in equation (2.6):

$$2K(g) + 3CO(g) = K_2CO_3(l) + 2C(s) \tag{2.6}$$

Above 1130°C equation (2.6) will proceed to the left, and K can again be found in elemental form[1]. This process serves to heat the charge in the prereduction zone and is known as alkali circulation. Potassium carbonate, K_2CO_3 also catalyzes the unwanted Boudouard reaction in equation (2.4).

The final reduction of MnO and SiO_2 to Mn and Si takes place at temperatures above 1600°C in the coke bed zone. According to the Ellingham diagram[11], shown as Figure A.1 in Appendix A.1, direct reduction with C(s) is required. Mn(l) and Si(l) are formed in correspondence with equations (2.7) and (2.8). Silicon carbide, SiC, is the stable carbon phase at Si-contents above 18%[12], so at high Si-levels the reduction of SiO_2 takes place through equation (2.9).

$$MnO(s,l) + C(s) = Mn(l) + CO(g) \tag{2.7}$$
$$SiO_2(s,l) + 2C(s) = Si(l) + 2CO(g) \tag{2.8}$$
$$SiO_2(s,l) + 2SiC(s) = 3Si(l) + 2CO(g) \tag{2.9}$$

The reversible slag/metal exchange reaction shown in equation (2.10) is considered to be much faster than the direct carbothermic reduction reactions expressed as equations (2.7) and (2.8), thus partial slag-metal equilibrium can be assumed established[1]:

$$2Mn(l) + SiO_2(l) = Si(l) + 2MnO(l) \tag{2.10}$$

At complete equilibrium, the Mn distribution between metal and slag is highly dependent on the process temperature, CO(g) pressure and slag composition. This can be observed from the equilibrium constant expression, shown in equation (2.11):

$$K_{Mn} = \frac{a_{Mn} \cdot p_{CO}}{a_{MnO} \cdot a_C} \rightarrow \frac{x_{MnO}}{x_{Mn}} = \frac{\gamma_{Mn} \cdot p_{CO}}{\gamma_{MnO} \cdot K_{Mn} \cdot a_C} \tag{2.11}$$

K_{Mn} is the equilibrium constant for MnO reduction through equation (2.7), p_{CO} is the partial pressure of CO(g), and x_i, a_i, γ_i are the mol fraction, activity and the activity coefficient of species i, respectively. It can be observed that high temperatures and low CO(g) pressures give a low MnO-content in the slag. The partial pressure of CO(g) is normally assumed equal to unity in a typical SiMn production furnace[1].

Similarly, the Si-content in the metal is dependent on the process temperature and activity of SiO_2 assuming $a_C = a_{SiC} = p_{CO} = 1$. Equations (2.12) and (2.13) show the correlation for low-Si and high-Si contents, respectively:

$$K_{Si,C} = \frac{a_{Si} \cdot (p_{CO})^2}{a_{SiO_2} \cdot (a_C)^2} \rightarrow a_{Si} = K_{Si} \cdot a_{SiO_2} \quad (2.12)$$

$$K_{Si,SiC} = \frac{(a_{Si})^3 \cdot (p_{CO})^2}{a_{SiO_2} \cdot (a_{SiC})^2} \rightarrow a_{Si} = \sqrt[3]{K_{Si,SiC} \cdot a_{SiO_2}} \quad (2.13)$$

The activity of SiO_2 is highly dependent on the R-ratio, expressing the ratio $\frac{CaO + MgO}{Al_2O_3}$ in the slag. For a given slag SiO_2-content, a low R-ratio will result in a higher equilibrium Si-content[1]. In an ordinary SiMn process, the maximum achievable Si content from carbothermal reduction of quartzite, SiO_2, is in the range 20 – 22%.

2.2 Industrial smelting practice

Traditionally, electric arc furnaces are utilized in smelting of ferroalloys due to flexibility in control and energy input, ability to produce a wide range of products, self-regulating nature and high throughput capacity and productivity[4,15]. Since the furnaces can be sealed, the environmental impact can be reduced to a minimum with adequate off gas handling. Rapidly increasing electricity prices and new legislation has lead to increased focus on furnace design development and better energy utilization.

2.2.1 Smelting modes

Four different types of electric furnaces are described in the literature[15], shown in Figures 2.3 and 2.4:

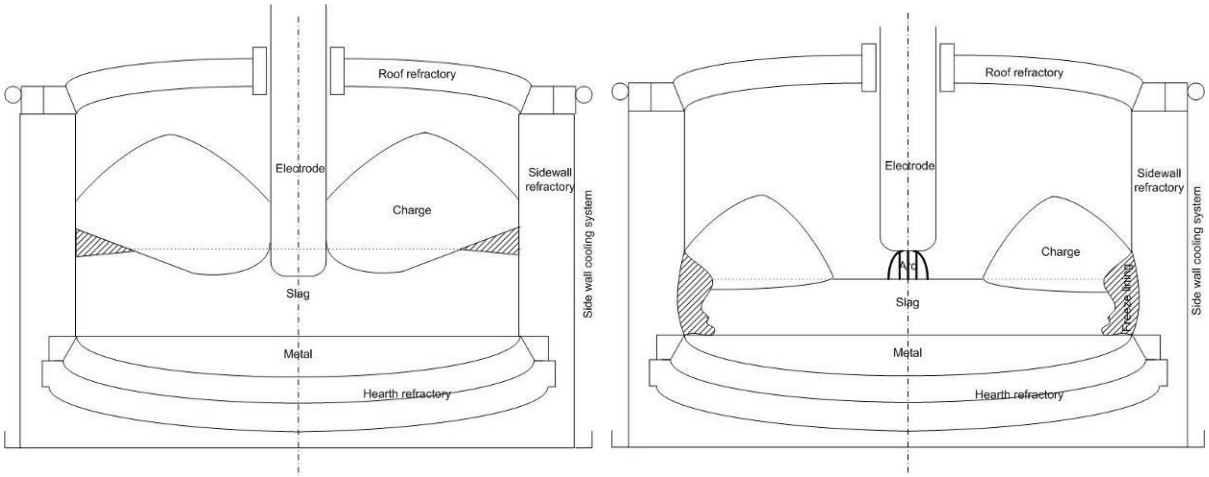

Figure 2.3: Industrial smelting methods. Left: Immersed-electrode. Right: Open-arc. From Steenkamp[16] after Matyas et al.[15]

Immersed-electrode smelting, shown in Figure 2.3 left, is utilized in production of matte and slag from Ni-Cu-PGM concentrate[16], where the electric energy is mainly used for melting the charge. The electrode tips are dipped in the slag bath, and electric energy is liberated through resistance heating. Due to natural and electromagnetically forced convection, sidewall refractories are subject to excessive wear.

Open-arc smelting, shown in Figure 2.3 right, is utilized in melting of metal with insufficient resistance to liberate electric energy through resistance heating, and in reduction of fine,

sinterable feed where gas evolution prohibits covering the arc with charge[15]. In this smelting mode, high voltages create arcs above the molten bath, liberating energy to the furnace freeboard. The energy is then transferred to the charge through radiation, resulting in refractory wear in furnace roof and upper side wall.

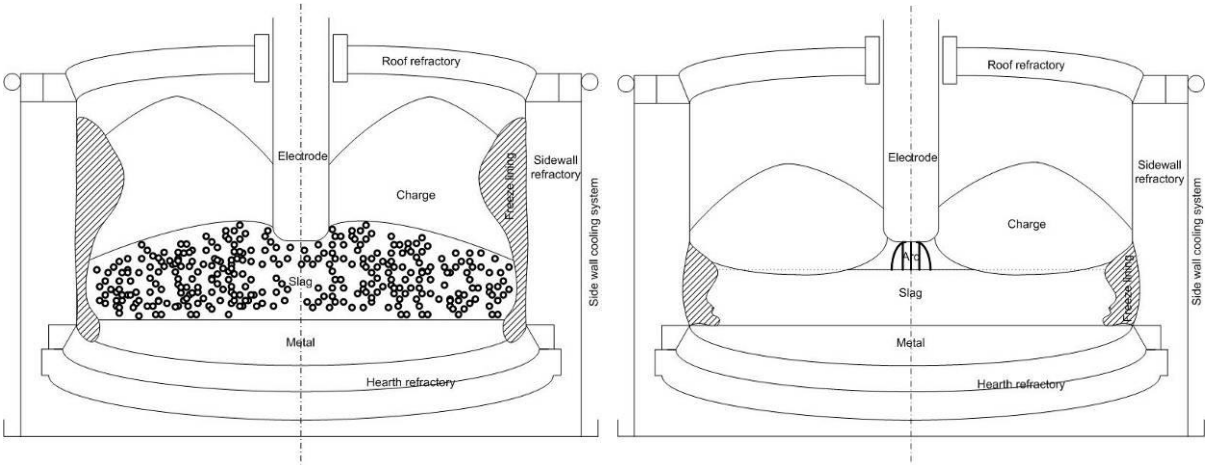

Figure 2.4: Industrial smelting methods. Left: Submerged-arc. Right: Shielded-arc. From Steenkamp[16] after Matyas et al.[15]

Submerged-arc smelting, shown in Figure 2.4 left, is utilized in production of ferroalloys, pig iron, metallic silicon and elemental phosphorus[15]. The electrode tips are covered with charge, and micro arcing liberates electric energy to a coke bed incorporated in the molten slag. Low voltages and high currents are required in order to obtain a sufficient power level input to the conductive charge mix. High current requirements lead to a limitation on furnace power level, limiting the productivity of the submerged-arc furnace. Another challenge is good electrode position control: Overheating and charge sintering are results of a too high electrode position, possibly resulting in gas eruptions.

Shielded-arc smelting, shown in Figure 2.4 right, enables higher power intensity without introducing problems with sidewall refractory erosion[15]. The electrode tip is completely covered with charge, and long, powerful arcs liberate electric energy to the slag surface. High voltages and low currents are possible due to low coke levels resulting in insufficient charge conductivity. In this mode, high productivity can be obtained without encountering problems controlling the electrode position, sintering of charge banks and dangerous gas blows as battled in submerged-arc smelting. Shielded-arc smelting has since its development by Falconbridge in the 1960's been utilized in nickel laterite ore smelting[16].

SiMn alloys are normally produced in circular, three-phase submerged-arc furnaces with three Söderberg electrodes positioned in an equilateral triangle arrangement[1]. Furnaces can be open or closed, rotating or stationary depending on the size of the furnace. The furnaces producing the main volume of SiMn alloys today are stationary and closed variations of the submerged-arc furnace shown in Figure 2.4 left.

2.2.2 Tapping

SiMn furnaces have to be tapped on a regular basis. Tapping takes place through tap holes located at the bottom of the furnace, and the tapping schedule depends on the furnace size and power input. For a 30 MW furnace, typical tap times are 20 – 40 minutes and tap-to-tap time is ~2 hours, giving 10 – 11 taps per day[17]. Slag and metal can be tapped through the same tap

hole, or dedicated tap holes for slag or metal can be utilized. Due to density differences, slag will float on top of the metal, so in the case of dedicated tap holes, the slag tap hole is located above the metal tap hole. Common practice is to have at least two tapping locations in order to decrease wear on the tap hole refractories. Figure 2.5 shows the location of the two tap holes in an industrial SiMn furnace, and Figure 2.6 shows a possible tap hole design. New, improved tap hole designs usually include copper coolers above and on both sides of the graphite or SiC tap block[15,17].

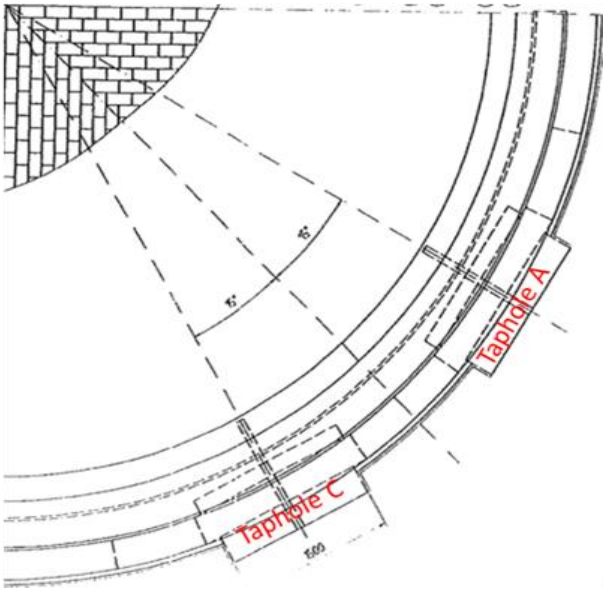

Figure 2.5: Tap hole locations, SiMn furnace

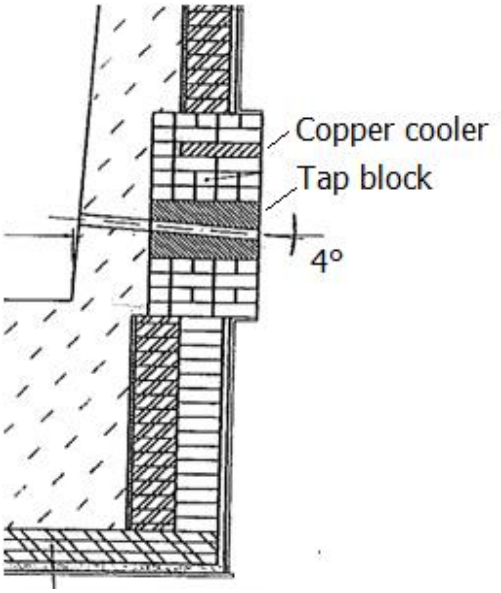

Figure 2.6: Tap hole design

From Steenkamp[17]

The tap hole is usually opened with a drill, kept open during tapping with a poker and plugged using a mud gun at the end of the tap[17]. Oxygen lancing can be used if, after drilling the full length of the drill, the furnace still cannot be tapped. Lancing should generally be avoided due to high temperatures causing excessive wear on tap hole refractories.

Tap holes need to be maintained on a regular basis in order to obtain long tap hole refractory life time. Common practice is to do weekly maintenance where heated electrode paste is plugged into tap hole using a mud gun[17]. Electrode paste is also rammed into the tap hole – mud gun interface in order to ensure proper connection between the mud gun and tap hole when plugging the tap hole with clay. The repaired tap hole is cured through heating with an external heat source and through skipping a tap. Figure 2.7 shows a well maintained tap hole:

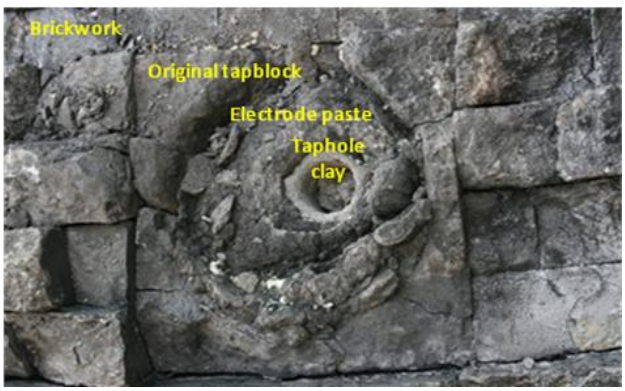

Figure 2.7: Weekly maintained tap hole

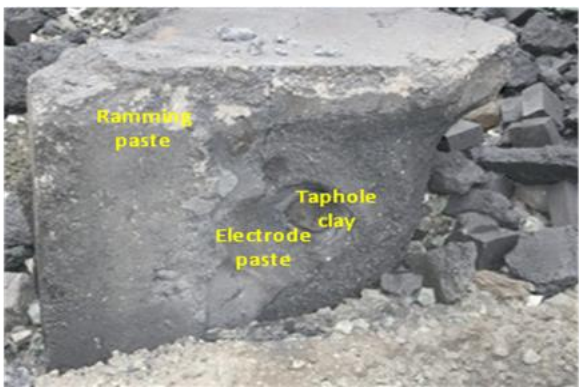

Figure 2.8: Ramming paste tap block

From Steenkamp[17]

In the case of a breakdown such as a burn-through, the tap hole needs to be repaired: The common practice for this procedure is to remove a large section of damaged refractory, preferably within the boundaries provided by copper coolers[17]. Cold ramming paste is rammed into position and cured, tying into the undamaged refractories. Upon curing, a new tap hole is drilled. Repairing the tap hole can take anywhere from a few hours up to three weeks[18]. The new ramming paste tap block has to be maintained according to the common practice described above. Figure 2.8 shows a maintained ramming paste tap block created as a result of a burn-through in the tap hole area.

2.3 Refractories

With the discovery of fire many thousand years ago arose the challenge of how to use the available combustion energy in a controllable manner. New materials were required, withstanding heat as well as high temperature contact with the materials being heated. This challenge was first overcome by Chinese bakers some 30 000 years ago; lining their baking ovens with primitive refractory linings made of clay and natural rocks[4]. In year 4000 B.C., the first use of refractories in metal production took place as Egyptians used clay crucibles to melt gold. Since then, production and use of refractories has developed into a major industry; today representing a critical factor for profitable furnace operation.

One of the biggest challenges today is the selection of refractories, greatly affecting furnace performance. Infelicitous choice of refractories results in down-time, loss of production and costly repairs. Hancock[6] states that: "*All too frequently, the current refractory is replaced by a more expensive product on the basis that increased initial lining costs should result in longer life."* Based on refractory discussions in Chapters 2.3 and 2.4, this refractory policy is shown to be obsolete.

2.3.1 Introduction to refractories

Refractories must be able to withstand extreme heat and corrosion conditions as well as show resistivity towards load, impact, abrasion and erosion. Table 2.2 defines corrosion, erosion and abrasion of refractories in accordance with Hancock[6] and Chesters[19]:

Table 2.2: Refractory wear definitions

Refractory wear	Definition
Corrosion of refractories	Deterioration or wearing away of refractories at their surfaces through chemical attack[6].
Erosion of refractories	Mechanical wearing away of the surface of refractory bodies in service by the washing action of moving liquids, such as molten slag or metals[6].
Abrasion of refractories	The wearing away of a surface due to a rubbing action, e.g. by dust-laden gases, or slabs on a hearth[19].

Most refractories are produced as dense bricks, insulation or monolithic structures[6], and consist of a combination of high-melting crystalline oxides with additions of carbides, carbon and graphite. Apart from physical form and chemical composition, refractories can be classified according to application, or parameters such as maximum service temperature, porosity or strength. Nonetheless, the most suitable combination of refractory materials for a given furnace geometry with defined temperature and chemistry has to be selected based on a combination of scientific data and previous experience.

Many different compounds have shown suitable refractory properties under different process conditions. Table 2.3 shows the major refractory groups, subgroups and their main components:

Table 2.3: Major refractory groups. From Hloben[4]

Group	Type	Main component(s)
Silica refractories	Silica glass	98 - 100 % SiO_2
	Silica(ganister)	93 – 98 % SiO_2
	Silica with additives	85 - 93 % SiO_2
Aluminosilicates	Corundum	90 – 100 % Al_2O_3
	Bauxite	75 – 90 % Al_2O_3
	Mullite (andalusite)	55 – 70 % Al_2O_3
	Fireclay (A1, A2, A3, A4)	36 – 45 % Al_2O_3
Magnesia-based	Magnesia	85 – 99 % MgO
	Dolomagnesia	60 – 85 % MgO, 10 – 40 % CaO
	Dolomite	35 – 60 % MgO, 40 – 65 % CaO
Magnesia-alumina	Magnesia-spinel	6 – 33 % Al_2O_3
	Spinel-magnesia	33 – 65 % Al_2O_3
	Spinel	65 – 90 % Al_2O_3
Magnesia-chrome	Magnesia-chromite	MgO ≥ 55 %, 6 – 27 % Cr_2O_3
	Chromagnesia	MgO ≤ 55 %, 18 – 40 % Cr_2O_3
	Picrochromite	Cr_2O_3 ≥ 70 %
	Chromite	MgO ≤ 25 %, Cr_2O_3 ≥ 35 %
Magnesia-silica	Magnesia-forsterite	MgO ≥ 55 %
	Forsterite	MgO ≤ 55 %, 20 – 45 % SiO_2
Zirconia-containing	Zirconia-based	ZrO_2 ≥ 85
	Zircon-based	50 – 85 % ZrO_2, SiO_2 ≤ 45%
	Baddeyeite - corundum	15 – 60 % ZrO_2, Al_2O_3 ≥ 30 %
	Mullite-zircon	4 – 15 % ZrO_2, Al_2O_3 ≤ 85%
Carbonaceous	Graphite	C ≥ 96 %
	Carbon	C ≥ 85 %
Silicon carbide	Direct bond	SiC ≥ 90 %
	Ceramic bond	SiC ≤ 90 %
	Other bonds (sialon, Si_3N_4, etc.)	SiC ≥ 75 %
Oxide-carbon	Magnesia/alumina-carbon	5 – 40 % C

A detailed description of each type of refractory is beyond the scope of this thesis. The focus for the rest of this chapter will therefore be on the C-based refractories utilized in industrial SiMn production furnaces.

2.3.2 Carbon

With a melting point of 3500°C, carbon is "the nature's best refractory" and has several advantageous properties[4,20]:

- High thermal conductivity
- High refractoriness under non-oxidizing conditions
- High electrical conductivity
- Low thermal expansion
- Good compression strength
- Excellent thermal shock resistance
- Low wettability towards molten slags and metals
- Increased strength at elevated temperatures

Production of C-refractories takes place through mixing of carbonaceous fillers such as calcined anthracite coal, petroleum coke or carbon black with binder materials like petroleum pitch or coal tar. The mixture is then molded or extruded and later heat treated in order to carbonize the binder. Depending on the baking temperature and further heat treatment, different degrees of graphitization can be achieved. In the literature, four variations of "pure" C-refractories exhibiting slightly different properties are described[4]:

Baked carbon is produced as large blocks baked at temperatures in the range 800 – 1400°C. These blocks are known to be quite porous due to binder carbonization and volatile evaporation, but can be densified through addition of additional binders. Addition of artificial graphite and fine ground metallic Si results in formation of a microporous material[20], characterized by 90 % of the pores having a diameter less than 1 μm. Graphite inclusions, formation of SiC and decreased average pore diameter compared to regular carbon blocks provide increased resistance to alkalis and oxidation exposure.

Through further heat treatment of baked carbon at temperatures in the range 2400 – 3000°C, carbon and binder can be completely graphitized, resulting in a product with enhanced thermal conductivity and increased resistance to chemical attack: *Graphite*. This carbon polymorph yields the highest thermal conductivity of the four "pure" C-refractory variations.

Semigraphite and semigraphitized material are products exhibiting properties between those of baked carbon and graphite: *Semigraphite* is produced from artificial graphite mixed with carbonaceous binders baked in the temperature range 800 – 1400°C. This results in C-bonded graphite with a higher thermal conductivity than baked carbon. For greater abrasion resistance and lower permeability, semigraphite can be impregnated with metallic Si or SiC.

The binder is normally attacked first when C-refractories are exposed to alkalis or oxidizing conditions. Chemical resistance can therefore be improved further through graphitization of the binder: *Semigraphitized material* contains C-particles and C-binder heat treated in the temperature range 1600 – 2400°C in order to achieve semigraphitized particles and binder. This way, higher thermal conductivity and resistance to chemical attack is achieved, exceeding that of both baked carbon and semigraphite.

In many industrial refractory applications, C is often utilized in combination with oxides such as MgO, Al_2O_3 and ZrO_2. MgO-C has had a big influence on the steel industry, finding usage in steelmaking furnace linings, while Al_2O_3-C can for example be used in continuous steel

casting[4]. ZrO_2-C can be used in areas especially exposed to severe erosion and corrosion in continuous casting[8].

2.3.3 Silicon carbide

Silicon carbide can be formed synthetically by heating mixtures of silica sand and petroleum coke to temperatures in the range 1600 – 2000°C. Since its discovery in 1891, SiC has been known for properties exceeding those of carbon and graphite[4]:

- Hardness surpassed only by diamond, cubic boron nitride, c-BN, and boron carbide, BC
- Excellent abrasion resistance
- Very high thermal conductivity
- Very good resistance to thermal shock
- Good load-bearing properties at high temperatures: High strength, low creep, low thermal expansion coefficient.

The compound resists chemical attack better than graphite and has a superior oxidation resistance due to the formation of SiO_2 at 1000°C. The glass formed in correspondence with equation (2.14) protects SiC up to 1500°C in oxidizing atmospheres:

$$SiC(s) + O_2(g) = SiO_2(s) + C(s) \tag{2.14}$$

In contact with high-MnO slags, SiC will oxidize according to equation (2.15). SiC should therefore not be utilized in FeMn production.

$$3MnO + SiC(s) = 3Mn + SiO_2(s) + CO(g) \tag{2.15}$$

The material is particularly useful as a tap hole refractory due to its excellent corrosion and abrasion properties. Monolithic pre-fabricated fired SiC blocks should however be utilized instead for SiC brick to avoid metal penetration at the joints.

2.3.4 Industrial lining concepts

Carbon-based refractories can be used under non-oxidizing conditions such as the reducing CO(g) atmosphere found in industrial SiMn furnaces described in Chapter 2.1.4. With a C-content close to saturation, Mn-alloys are not expected to interact majorly with C, and C-based refractories are therefore suitable for use as inner furnace lining[1].

According to Hloben[4], two lining concepts are used industrially: Insulating and freeze lining concepts. The insulating concept applies the mass versus time principle with primary purpose being to protect the furnace shell[5]. The lining consists mainly of big C blocks which are eroded over time. Figure 2.9 shows a cross section of the furnace wall where the temperature gradients in each material are indicated.

The furnace bottom, as well as the side lining up to a height well above the normal slag level, are usually C-based and built from two layers of machined blocks or C ramming mixtures fit tightly together. Some areas are difficult to ram satisfactorily, so pre-extruded slabs are utilized. Ceramic refractory brickwork separates the C lining and the steel shell, extending above the C lining to the top of the furnace. The thickness of the C hearth varies in the range 1.0 – 1.8 meters[4]. SiC-based bricks can be used under the C hearth to avoid excessive overheating of the sub-hearth ceramic lining.

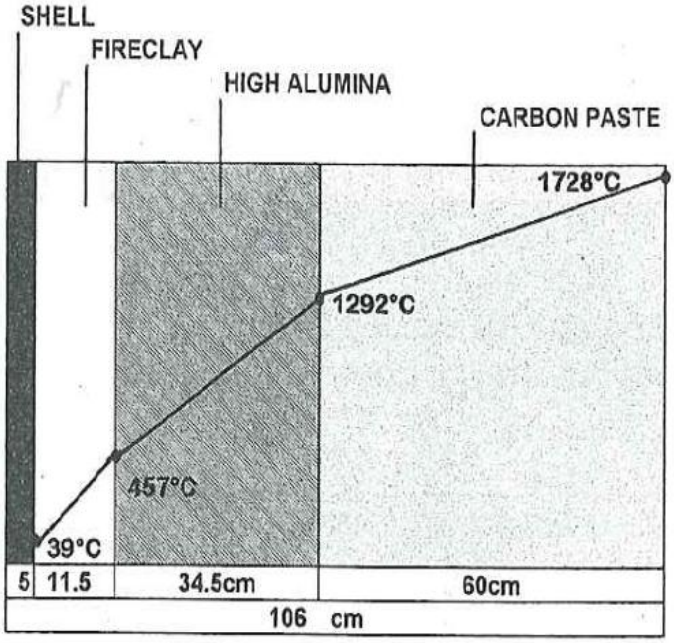

Figure 2.9: Insulating lining concept. From Hloben[4]

The freeze lining concept has been industrially accepted since 1995[5], and relies on a frozen layer of process material, skull, protecting the refractory lining from the common wear mechanisms described in Chapter 2.4. In order to obtain the skull, the refractory system has to be able to transport heat swiftly and efficiently away from the hot phase, resulting in a hot phase temperature sufficiently lower than the solidus temperature of the process materials. The skull then serves as the working lining of the furnace. Figure 2.10 shows the freeze lining concept including temperature gradients in the different materials, and Figure 2.11 shows a typical freeze lining configuration in a submerged-arc furnace before start-up:

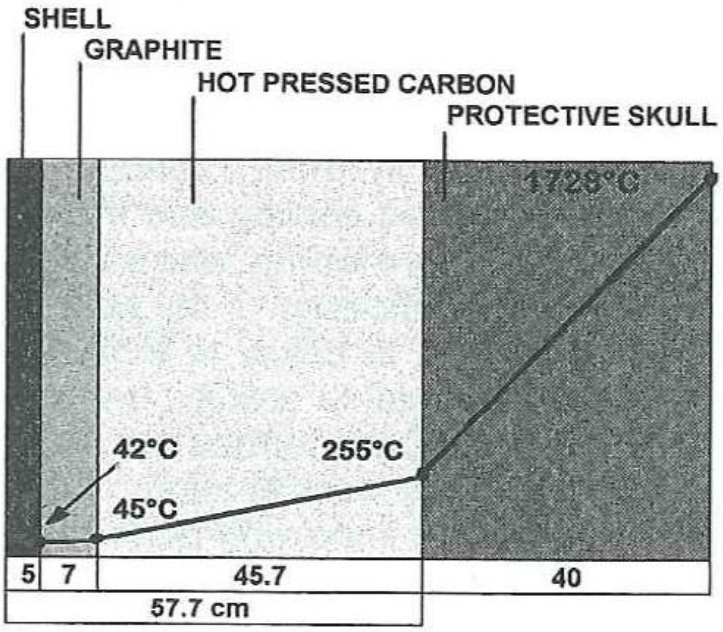

Figure 2.10: Freeze lining concept. From Hloben[4]

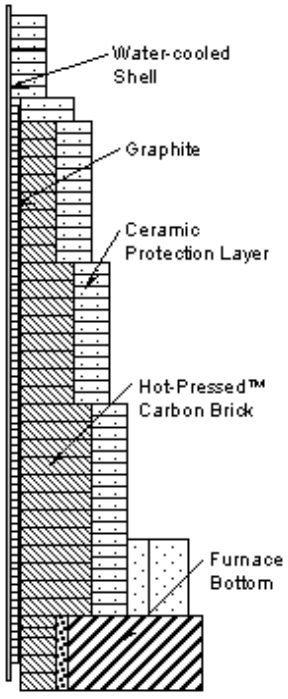

Figure 2.11: Freeze lining configuration. From Duncanson & Toth[5]

The refractory wall is composed of graphite tiles and hot-pressed C bricks as shown in Figure 2.11, with side wall thickness varying from 300 mm to 527 mm[5]. Both C-based materials have high thermal conductivities, and heat is therefore transported away from the hot phase. A continuous water film on the steel shell absorbs the transferred heat, and a sacrificial ceramic layer is commonly installed to protect the carbon lining during furnace start-up.

In a freeze lining, the total heat flux, q_{tot}, needs to be closely controlled[5]. Heat flux through a material, q_i, is normally given as $\left[\frac{W}{m^2}\right]$ and can be expressed through the one-dimensional expression shown in equation (2.16):

$$q_i = \frac{k_i \cdot (T_2 - T_1)}{l_i} \tag{2.16}$$

k_i is the thermal conductivity of the material given as $\left[\frac{W}{m \cdot K}\right]$, T is the temperature and l_i is the distance of heat transfer. One-dimensional heat transfer is commonly understood through an analogy between heat flux and electric current, I. I is the rate of energy transfer given as $[A] = \left[\frac{C}{s}\right]$ and can be expressed through Ohm's law shown in equation (2.17):

$$V = R \cdot I \quad \rightarrow \quad \mathrm{I} = \frac{V}{R} \tag{2.17}$$

In equation (2.17), V is the voltage and R is the resistance. Comparing equations (2.16) and (2.17), the thermal resistance, R_{th}, can be expressed as equation (2.18):

$$\frac{1}{R_{th}} = \frac{k}{l} \quad \rightarrow \quad R_{th} = \frac{l}{k} \tag{2.18}$$

Thermal resistance due to convection must also be considered in the total heat flux, and can be expressed as the inverse convection coefficient, h, as shown in equation (2.19):

$$R_{th,convection} = \frac{1}{h} \tag{2.19}$$

The thermal resistance of the whole system is the sum of all the resistances:

$$R_{th,tot} = R_{th,cooling} + R_{th,1} + R_{th,2} + \ldots + R_{th,n} + R_{th,skull} \tag{2.20}$$

The total heat flux, q_{tot}, can then be calculated through equation (2.21):

$$q_{tot} = \frac{(T_{process} - T_{cooling})}{R_{th,tot}} \tag{2.21}$$

Since the heat flux is the same in each component of the lining, q_{tot} can be used to calculate the temperature drop in the individual components through equation (2.16). q_{tot} is therefore a critical parameter during the design phase of the freeze lining system.

A freeze lining is a dynamic thermal system driving towards equilibrium heat flux[5]. The thickness of the skull varies with hot phase temperature, so with increased temperature, the skull thickness is reduced until thermal equilibrium again is established. For maximum efficiency and lifetime, the furnace lining should be thin, consist of small pieces of thermally conductive refractory materials, have a tight fit to a robust cooling system and expansion should be properly accommodated. Only when all these factors are taken into consideration, the term true freeze lining can be used[5].

2.4 Refractory lifetime

As established in Chapter 2.3, refractory lifetime is critical for furnace performance. Upon well-founded selection of refractory materials, the challenge then consists of reducing factors negatively affecting the refractory lifetime.

2.4.1 Factors affecting refractory lifetime

One of the most common causes of premature refractory failure is incorrect installation procedures[6]. This can be due to insufficient training, or simply ignorance both by installation personnel and refractory suppliers. For a refractory lining to work as intended by the manufacturer, it is important to assure correct mixing ratios, mixing procedures and installation techniques. If the water ratio is incorrect and the water purity or temperature is not suitable, a castable refractory will behave differently than what was intended and might be impossible to work with. During mixing, suitable equipment should be utilized to ensure the correct level of stirring, and mixing time and temperature are normally critical. Correct choice of equipment during installation in the furnace is also important, in order to ensure a tight refractory lining with no cracks accessible for penetration by process materials. Finally, curing conditions are of critical importance, and errors can in many cases ruin an otherwise correctly installed lining. Installation errors can be swiftly detected through post-mortem examinations, although these are time demanding and are therefore often skipped in an attempt to restart production as fast as possible.

Minor and major changes in process operational variables can have a large effect on refractory lifetime[6]. Production personnel are often unaware of which factors that influence the lifetime of the refractories installed in the different production units, hence small changes in operating temperature or slag composition can be carried out without thorough refractory failure consideration. Depending on the type of furnace and the mode of operation, over 20 different types of failures due to process changes have been identified[6].

In submerged-arc furnaces, three different wear mechanisms leading to refractory failure are dominant[5]:

- Chemical wear
- Thermal stress
- Erosion

As defined in Table 2.2, chemical wear is a result of chemical interaction between the refractories and the process materials, spalling due to thermal stresses is a result of non-uniform thermal expansion in the material, and erosion is material disintegration caused by natural or forced convection.

According to Duncanson & Toth[5], all the three dominant wear mechanism can be related to high temperatures: Chemical interaction is only thermodynamically and kinetically favorable

in certain high temperature intervals, the thermal expansion coefficient is a function of temperature, and erosion can be prevented by formation of a protective layer at lower temperatures. Logic then implies that refractory wear can be minimized at lower temperatures – the fundamental concept of freeze linings described in chapter 2.3.4.

2.4.2 Chemical wear

Chemical wear, also known as corrosion or slagging, is caused by the formation of a liquid due to chemical interaction between refractories and process materials[6]. Liquid formation can be a result of chemical reactions on the refractory surface, or reactions both on the surface and within the refractory. A new compound with a lower melting point can be formed, reaction products can be soluble in the liquid slag, or melting point depression can occur as a result of penetration into the refractory structure. Melting point depression is closely related to refractory porosity and permeability, since these two properties control the surface areas available for attack by slag and gasses, respectively. Dissimilar phases tend to react at high temperatures, so in order to limit chemical wear, slags and refractories should be of a similar nature[8].

According to Lee and Zhang[8], dissolution of refractories into slag can both be direct and indirect: For direct dissolution, atoms in the refractory material dissolve directly into the liquid melt. If a first order chemical reaction is the rate limiting step, the dissolution rate, J, can be expressed through equation (2.22):

$$J = K \cdot C_m \cdot \left(\frac{A_c}{A_o} \right) \tag{2.22}$$

K is the rate constant, C_m is the reactant concentration in the melt, A_c is the actual area of the refractory and A_o is the apparent area of the refractory. Clearly, porosity has a big effect in this model, directly affecting the A_c/A_o- ratio.

If the rate of reaction product removal is slower than the rate of chemical reaction, the dissolution rate is controlled by diffusion through a boundary layer. For a slag saturated in refractory components, the reaction product-rich boundary layer can lead to formation of a solid interlayer, shown in Figure 2.12. Refractory dissolution is now indirect:

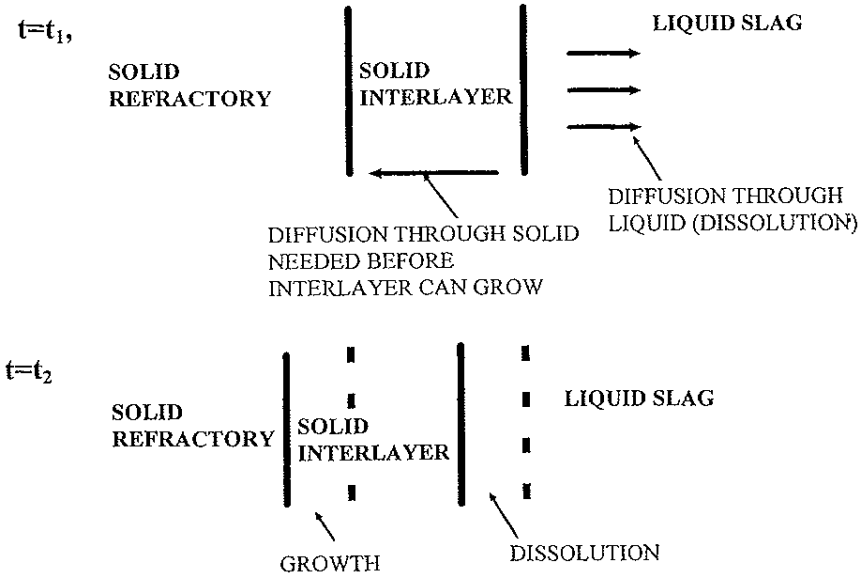

Figure 2.12: Indirect refractory dissolution through solid interlayer. From Lee and Zhang[8]

Fick's first law, shown in equation (2.23), can be used to express the indirect dissolution rate:

$$J = D \cdot \left(\frac{C_s - C_m}{\delta} \right) \tag{2.23}$$

D is the diffusion coefficient, C_s is the saturation concentration of refractory in the melt, C_m is the concentration of reactant in the melt and δ is the effective boundary layer thickness.

In the case of stirring, indirect dissolution is converted to direct dissolution, as the boundary layer thickness is reduced[8]. Under natural convection, the dissolution rate of a thin plate was expressed by Levich[21] as equation (2.24). For a rotating disc geometry representing a system under forced convection, the dissolution rate can be expressed as equation (2.25).

$$J = 0.5D \cdot (C_s - C_m) \cdot \left(\frac{\Delta\rho \cdot g}{D \cdot \eta} \right)^{\frac{1}{4}} \cdot x^{-\frac{1}{4}} \tag{2.24}$$

$$J = D \cdot \frac{(C_s - C_m)}{3.09} \cdot \left(\frac{U}{\nu \cdot x} \right)^{\frac{1}{2}} \cdot \left(\frac{\nu}{D} \right)^{\frac{1}{3}} \tag{2.25}$$

Δρ is the density difference between saturated and bulk melt, η is the dynamic viscosity, g is the gravitational constant, x is the distance from the refractory, U is the bulk velocity of the fluid and ν is the kinematic viscosity. Based on equations (2.24) and (2.25), it can be observed that dissolution can be minimized through controlling the term (C_s - C_m), therefore calling for close control of refractory saturation in the slag.

Hloben[4] lists possible additional routes leading to chemical wear specifically for C-based refractories in a SiMn furnace: Alkali attack, SiO-gas attack and graphitization. Silva et al.[22] have proposed a mechanism for the former: Gaseous potassium formed in the alkali circulation process described in Chapter 2.1.4 can react with carbon dioxide, CO_2(g), to form potassium oxide, K_2O, in correspondence with equation (2.26):

$$K_2(g) + CO_2(g) = K_2O(s,l) + CO(g) \tag{2.26}$$

K_2O can react further with Al_2O_3 and SiO_2 in the C ashes to form liquid potassium aluminum silicates kaliophilite, $K_2O \cdot Al_2O_3 \cdot 2SiO_2$, and leucite, $K_2O \cdot Al_2O_3 \cdot 4SiO_2$ through equations (2.27) and (2.28), respectively:

$$K_2O(s,l) + Al_2O_3(s) + 2SiO_2(s) = K_2O \cdot Al_2O_3 \cdot 2SiO_2(l) \tag{2.27}$$

$$K_2O \cdot Al_2O_3 \cdot 2SiO_2(l) + 2SiO_2(s) = K_2O \cdot Al_2O_3 \cdot 4SiO_2(l) \tag{2.28}$$

These liquids form in the refractory pores disintegrating the material, and result in structural spalling which will be discussed in the next chapter.

Investigations of the silicon process[23] have established that formation of silicon monoxide gas, SiO(g), is necessary in order to reduce SiO_2 to Si. In contact with the furnace lining, SiO(g) can react with C to form SiC in correspondence with equation (2.29), causing refractory wear[4]:

$$SiO(g) + 2C(s) = SiC(s) + CO(g) \tag{2.29}$$

SiO(g) can also penetrate into pores, where the gas will condense according to equation (2.30):

$$2SiO(g) = Si(l,s) + SiO_2(l,s) \tag{2.30}$$

SiO-condensate blocking the pores results in increased thermal conductivity, possibly causing melting of the sub-hearth refractories. The same phenomena results from graphitization of C-refractories catalyzed by alkali vapor. As described in Chapter 2.3.2, graphite has a higher thermal conductivity than C, so upon partial graphitization, the temperature in the sub-hearth can reach temperatures as high as 1750 – 1800°C causing melting.

2.4.3 Spalling

Spalling, or cracking, of a refractory material can be a result of thermal, structural or mechanical stresses leading to loss of fragments from the refractory hot face[6]. *Thermal spalling* is caused by a non-uniform temperature gradient in the refractory, resulting in non-uniform expansion and contraction of the material. Figure 2.13 shows how different temperature gradients cause material expansion and how this leads to cracking:

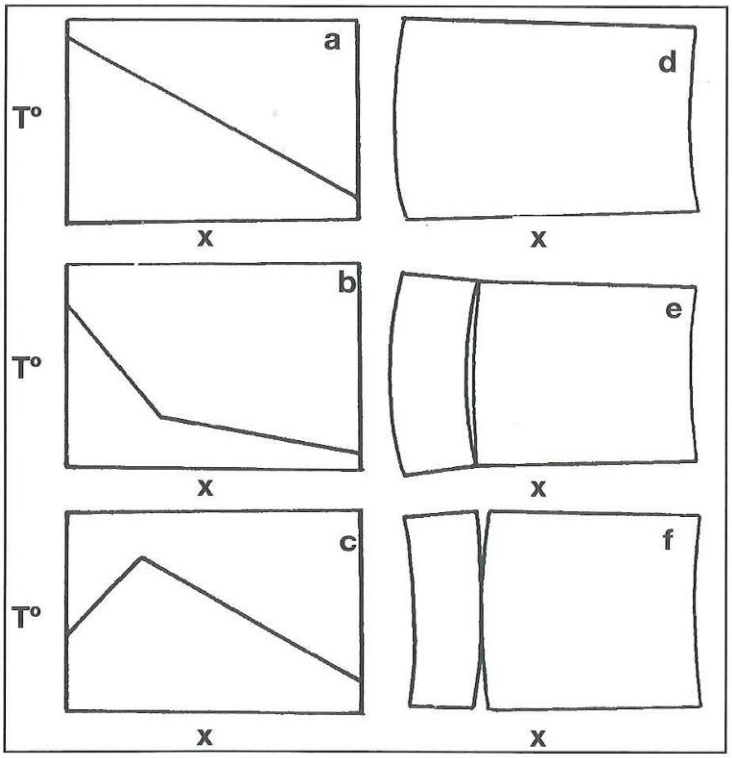

Figure 2.13: Origin of thermal stresses causing cracking parallel to the hot face of refractories. a), b) and c) show temperature gradients, and d), e) and f) show the resulting curvatures. From Hancock[6].

In Figures 2.13 a) and d), a temperature gradient in the material causes the hot face to expand more than the cold face. If the hot face temperature is increased quickly, a non-uniform temperature gradient is established as seen in Figure 2.13 b). This induces internal stresses in the material, and cracking is observed parallel to the hot face, as seen in Figure 2.13 e). In practice[6], the crack appears 30 – 50 mm from hot face, and the break-off angle is ~45°. Cracking can also take place as a result of rapid hot face cooling, for example through an unintended cooling water leakage: Figure 2.13 c) shows the induced non-uniform temperature gradient, and Figure 2.13 f) shows the resulting thermal spalling. Thermal spalling can be restricted using high-porosity materials with low reversible thermal expansion coefficients

and high thermal conductivities. Utilizing refractory pieces with a small cross section will also reduce the risk of thermal spalling[18].

Structural spalling is caused by structure alterations after overheating or chemical attack[6]. Structure alterations can create differences in thermal expansion coefficients between affected and unaffected areas, which through a sudden change in temperature gradient induce cracking at the interface. Oxygen tap hole lancing introduces temperatures above the refractory sintering temperature, and with excessive lancing the refractory structure can be altered. Direct contact with O_2(g) will also oxidize C(s) to form CO(g) and CO_2(g) in C-based refractories. Chemical attack causing structural spalling is related to chemical wear, but in the case of spalling, slag penetration into refractories is the main factor. According to Lee & Zhang[8], slag penetration takes place through capillaries such as open pores and microcracks, and the slag penetration depth, d_{pen}, can be expressed through equation (2.31):

$$d_{pen} = \sqrt{\frac{r \cdot \cos\theta}{2} \cdot \frac{\gamma}{\eta} \cdot t} \tag{2.31}$$

r is the capillary radius, θ is the wetting angle, η is the dynamic viscosity of the slag, γ is the slag surface tension and t is time. It can be observed that increased viscosity will reduce slag penetration, pinpointing the desire for low hot face temperatures. During penetration, θ and γ can vary with time as a result of chemical reactions.

Mechanical spalling, commonly known as mechanical failure, describes cracking, shearing or crushing of a refractory caused by application or restriction of a mechanical force[6]. In the case of inadequate allowance for thermal expansion, the mechanical forces can exceed the critical limit of the material, resulting in refractory cracking. Typical expansion allowances can be found in the literature[6], and should be utilized when designing the refractory lining.

2.4.4 Erosion

Supplementing the definition in Table 2.2, erosion can be described as physical wear of refractories as a result of turbulent gas and liquid flow[24]. The wear mechanism is related to abrasion, defined as physical wear caused by solids[6]. In a submerged-arc furnace, enhanced erosion tends to take place at the metal-slag and slag-atmosphere interfaces, known as slag line erosion, and in and around the tap hole.

Mills[24] describes slag line erosion utilizing the principle of Marangoni flow: A meniscus is formed upon contact between slag and refractory, dissolving some of the refractory material and thereby locally altering the surface tension. Driven by the surface tension gradient, flow is established from low to high surface tension, resulting in the formation of a vortex gradually eroding the refractory material. Marangoni flow is shown for a silica refractory and a SiO_2-PbO slag in Figure 2.14.

Since $\gamma_{SiO_2} > \gamma_{PbO}$, slag is pulled upwards as shown in Figure 2.14, covering and dissolving new slag layers. This mechanism is known as slag creeping, and the upwards motion will continue until the force of gravity exceeds the force related to Marangoni flow.

In order to avoid excessive erosion, slag properties need to be controlled[24]: Increasing the slag viscosity will decrease the fluidity, and a reduction in the slag flow rate will therefore be observed. Flowing metal can also introduce a drag force on the slag, so by reducing the metal flow rate through electromagnetic braking, slag flow can be reduced.

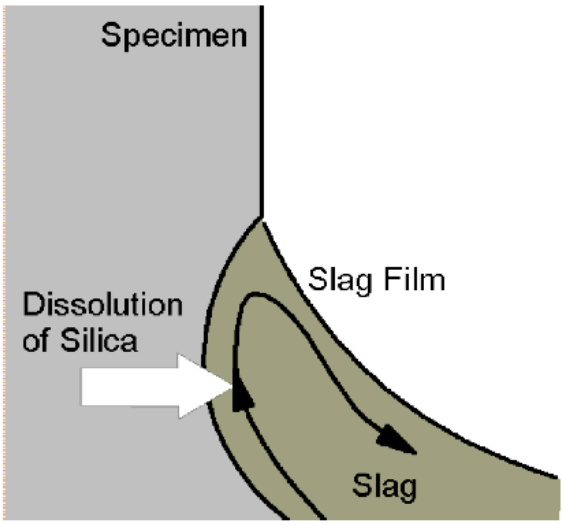

Figure 2.14: Mechanism for silica slag line attack by PbO-SiO_2 slag. From Mills[24]

Another way to reduce slag erosion is to saturate the slag on refractory components, as mentioned in Chapter 2.4.2. The driving force for erosion is $\Delta C = (C_{sat} - C_o)$, C_{sat} and C_o being the saturation and actual concentrations, respectively. Saturating the slag will result in $C_{sat} - C_o = 0$, and erosion can be avoided.

Refractory lives can also be extended ensuring non-wetting properties between slag and refractory, obtainable through application of an electrical potential[24]. The C-based refractories utilized in a SiMn furnace already have this non-wetting property, as described in Chapter 2.3.2. A final way to avoid refractory erosion is to establish a freeze lining, protecting refractories through a frozen layer of process materials, as discussed in Chapter 2.3.4.

Establishing a freeze lining will protect the general refractory lining, but this solution is not possible in the most critical part of the furnace refractory lining: The tap hole. For several hours a day, liquid metal and slag flow through the tap block, causing erosion in and around the tap hole, eventually causing burn-throughs in the tap hole areas. As described in Chapter 2.3.3, a material such as SiC should therefore be utilized due to the excellent abrasion resistance possessed by the material. The tap hole should also be regularly maintained in accordance with procedure in Chapter 2.2.2 in order to achieve as long tap hole lifetime as possible.

2.4.5 Slag properties affecting refractory life time

The previous chapters show that the slag can be held partially responsible for chemical wear, spalling and erosion. Controlling the slag properties is therefore of essence, and especially properties such as liquidus temperature, viscosity and wetting of the refractory materials.

According to Olsen, Tangstad and Lindstad[1], SiMn slags consist mainly of oxides SiO_2, CaO, MgO, Al_2O_3 and MnO. Typical five component SiMn slag compositions are presented in Table 2.4:

Table 2.4: Typical composition ranges for SiMn slags. From Olsen, Tangstad and Lindstad[1]

Slag component	CaO	Al_2O_3	SiO_2	MgO	MnO
[wt%]	20 – 35	10 – 25	38 – 44	5 – 15	6 – 12

The *liquidus temperature* of a slag is controlled by the relative amounts of acidic and basic oxides present, and has been shown to increase with increasing basicity ratio[1], B, expressed as equation (2.32):

$$B = \frac{CaO + MgO}{SiO_2 + Al_2O_3} \tag{2.32}$$

MgO has been shown to have a larger effect on liquidus temperature than CaO, and a decrease in liquidus temperature has been observed as a result of increased MnO content. Figure 2.15 shows calculated liquidus contours of SiO_2-CaO-Al_2O_3-10%MgO-5%MnO slags. Typical industrial slags are indicated as a green oval:

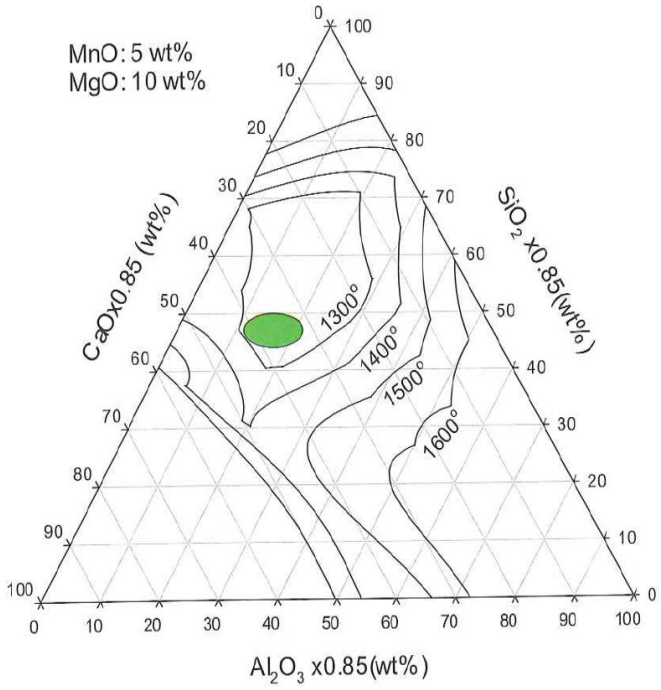

Figure 2.15: Calculated liquidus contours for SiO_2-CaO-Al_2O_3-10%MgO-5%MnO slags. Typical industrial slags are indicated as a green oval. From Olsen, Tangstad and Lindstad[1]

In liquid state, a slag is able to interact chemically with the refractory lining to a larger extent than in solid state. The liquidus temperature of the slag can therefore give indications regarding when chemical interaction between slag and refractory materials is a threat. A molten slag will also be able to penetrate into the refractory lining, causing densification and possibly structural spalling.

Viscosity, η, influences the flowing properties of a slag, making it an important parameter with regards to chemical wear, erosion and spalling. Factors affecting the viscosity are slag composition, temperature and presence of solids in the molten slag[1]. An acidic oxide such as SiO_2 is a network former and will contribute to an increased viscosity, while basic oxides such as MgO, CaO and MnO will break up the silica network and thus decrease the viscosity. Al_2O_3 is an amphoteric oxide and can therefore act as both a network former and network breaker. Equation (2.33) describes how the viscosity decreases with increasing temperature[25]:

$$\eta = \eta_0 \cdot \exp\left[\frac{G^*}{RT}\right] \tag{2.33}$$

η_0 is the pre-exponential factor , G^* is the viscous activation energy, R is the gas constant and T is the thermodynamic temperature. The effective viscosity[26], η_e, of a melt containing solid particles can be expressed as equation (2.34):

$$\eta_e = \eta_l \left(1 - 1.35\Phi_s\right)^{-2.5} \tag{2.34}$$

η_l is the viscosity of the liquid, and Φ_s is the volume fraction solid particles; assumed to be spherical and uniform in size.

Table 2.5 shows calculated viscosities for four industrial SiMn slag samples utilizing three different viscosity models. Tang and Tangstad[25] specially developed their model to predict viscosities for industrial FeMn multicomponent slags . The authors claim that their model can be used to predict the viscosities of liquid ternary, quaternary and higher order silicate melts within the experimental uncertainties present when physically measuring the viscosities. Urbain & Mills[24,27] and Riboud[28] models are known to quantify viscosities for a variation of slags with a 25 % and 30 % deviation[24] between measured and calculated viscosities, respectively.

Table 2.5: Calculated viscosity data for industrial SiMn slag samples

Industrial slag sample	**Component [wt%]**					**Calculated viscosities [poise]**					
						Tang & Tangstad model[25]		**Urbain & Mills model[24,27]**		**Riboud model[28]**	
	SiO_2	**Al_2O_3**	**CaO**	**MgO**	**MnO**	**1500°C**	**1600°C**	**1500°C**	**1600°C**	**1500°C**	**1600°C**
A	39.1	22.0	26.1	6.0	6.9	6.2	3.5	15.1	7.8	18.8	8.1
B	42.2	21.5	20.0	7.6	8.8	7.7	4.2	20.2	10.1	25.8	11.0
C	42.1	20.9	22.4	6.9	7.7	7.1	3.9	18.2	9.2	23.4	10.0
D	41.8	20.0	29.0	6.2	3.1	5.9	3.2	14.4	7.4	18.6	8.2

From Table 2.5 it can be observed that all models predict increased viscosities with increasing silica content, and decreasing viscosities with increasing calcia content. A fluid slag will be of larger threat than a viscous slag in terms of chemical wear, and will also be able to penetrate into a refractory lining more easily. The amount of solids in the molten slag will influence the erosive and abrasive properties of the slag.

Chemical wear is also affected by the degree of *wetting* between slag and refractory lining. Wetting is dependent on relative surface tension; a property of thermodynamic nature affecting reaction kinetics, nucleation and suspension formation in molten slags[26]. A high degree of wetting will result in a large contact area increasing the probability of chemical interaction. Figure 2.16 visualizes the wetting angle, θ, at wetting and non-wetting conditions:

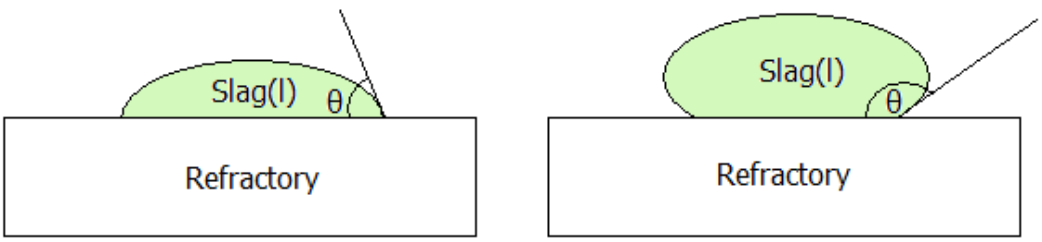

Figure 2.16: Wetting(left) and non-wetting(right) conditions for a slag droplet on a piece of refractory. After Mills[24]

Mills[24] describes the phenomena of reactive wetting at high temperatures, and claims that wetting will occur when there are reactions taking place between the slag/metal and the refractory surface. An example of this is a slag wetting and reacting with oxide refractories at high temperatures.

As discussed in chapter 2.3.2, C-based refractories generally have low wetting angles towards slags. Chapter 2.3.4 states that since SiMn alloys have a C content close to saturation, minimal interaction with C-based refractories is expected.

2.5 Refractory wear tests

Refractory wear tests, in some cases referred to as corrosion tests[7] or slagging tests[6], have been developed in an attempt to simulate the environment refractories are exposed to during service. Static wear tests simulate corrosion due to chemical interactions influenced by free interfacial convection and free density convection, while dynamic wear tests also strive to incorporate the forced convection of the corrosive fluids relative to the refractory. A major drawback during static tests is rapid saturation of the corrosive medium with reaction products[8]. The corrosive medium can be replaced continuously or periodically during dynamic tests, enabling better composition control throughout the experiment.

According to Hancock[6], all laboratory slagging tests have to be conducted at a higher temperature than the desired service temperature in order to finish the test in a reasonable time. By doing so, the obtained results have to be treated with caution, since an increased temperature can change the nature of the chemical attack. Ideally, a post-mortem study examining refractory materials after exposure to actual service conditions should be done in order to identify the failure mechanisms. This can be done through XRD and SEM investigations.

2.5.1 Wear evaluation and test visualizations

Refractory wear is commonly evaluated through quantifications of geometrical changes in diameter or immersed volume, or though flux line depth, d, as described by Dunkl[7]. This value is calculated according to equation (2.35) based on thickness measurements of sectioned finger or plate samples at the liquid-gas interface before and after refractory wear:

$$d = \frac{t_i - t_c}{2} \tag{2.35}$$

t_i is the initial sample thickness, and t_c is thickness at the liquid-gas interface after refractory wear. Using values for sectioned samples, potentially adhered glass layers can be omitted easily.

ASTM standard C621-09[29] presents a similar calculation for attack evaluation at the liquid-gas interface after isothermal corrosion testing. Glass line corrosion, G_c, takes the diameter of both sample halves into consideration, as shown in equation (2.36):

$$G_c = \frac{G - \frac{1}{2}(g_1 + g_2)}{2} \tag{2.36}$$

G is the initial sample diameter, and g_1 and g_2 are the diameters of the sample halves after the test. ASTM C621-09 also calls for the calculation of the half-down corrosion, H_c, describing

the attack half-way between the liquid-gas interface and the bottom of the sample. H_c can be calculated according to equation (2.37):

$$H_c = \frac{H - \frac{1}{2}(h_1 + h_2)}{2} \tag{2.37}$$

H is the initial sample diameter at the half-way point, and h_1 and h_2 are the diameters of the sample halves after corrosion testing.

Figures 2.17 through 2.26 visualize the different refractory wear tests which will be discussed during the rest of this chapter:

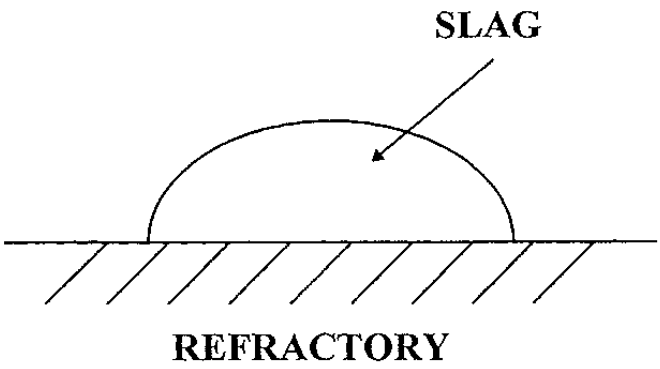

Figure 2.17: Sessile drop test. From Lee and Zhang[8]

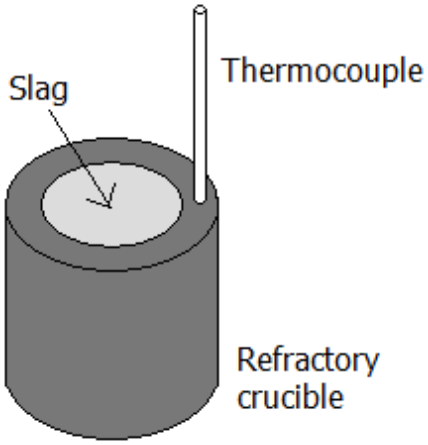

*Figure 2.18:*Crucible test

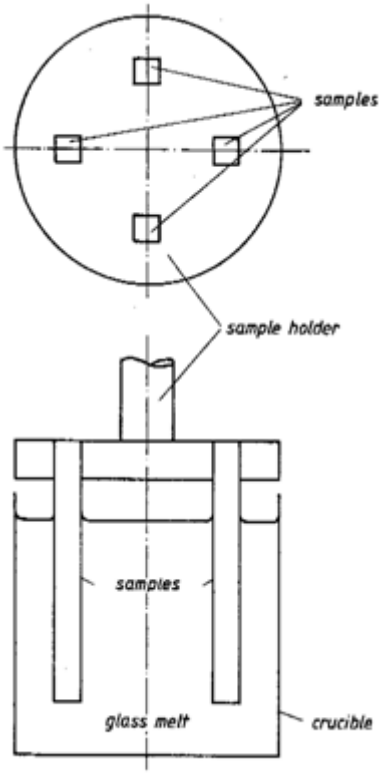

Figure 2.19: Static finger test. From Dunkl[7]

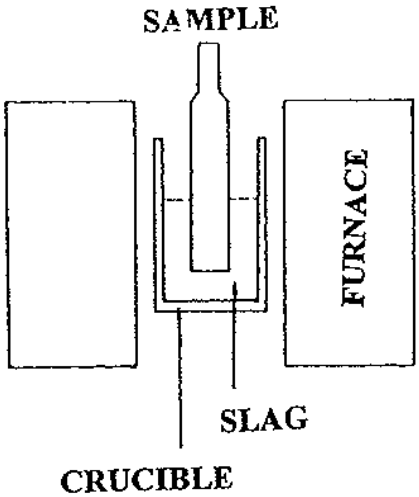

Figure 2.20: Static finger test. From Lee and Zhang[8]

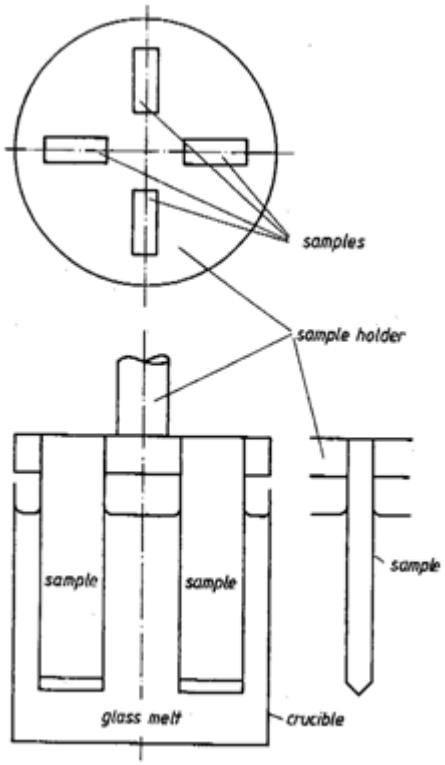

Figure 2.21: Static plate test. From Dunkl[7]

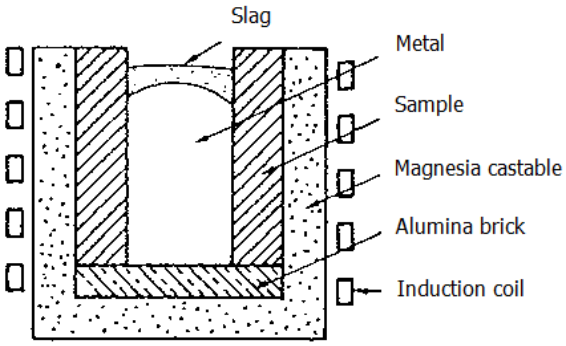

Figure 2.22: Induction furnace test. After Lee and Zhang[8]

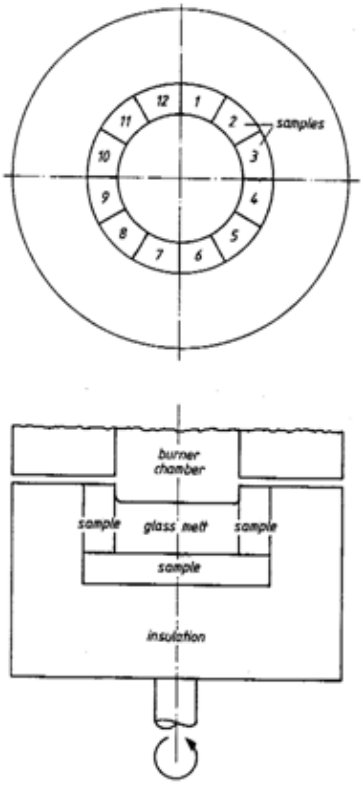

Figure 2.23: Rotating furnace test. From Dunkl[7]

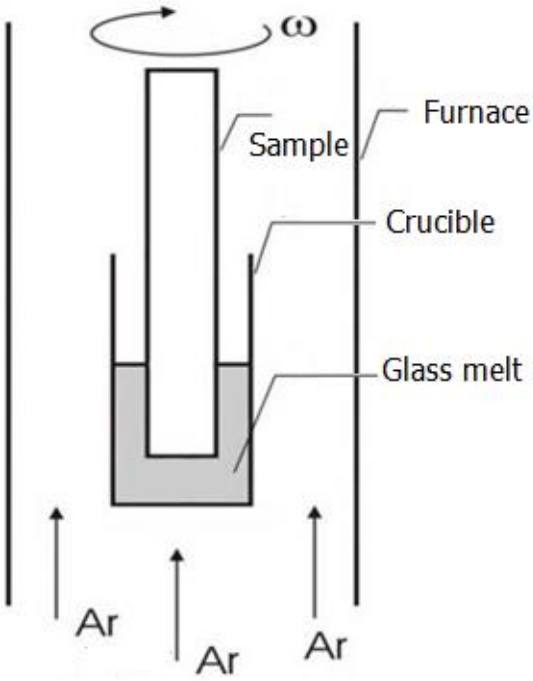

Figure 2.24: Rotating finger test. From Tomala and Basista[20]

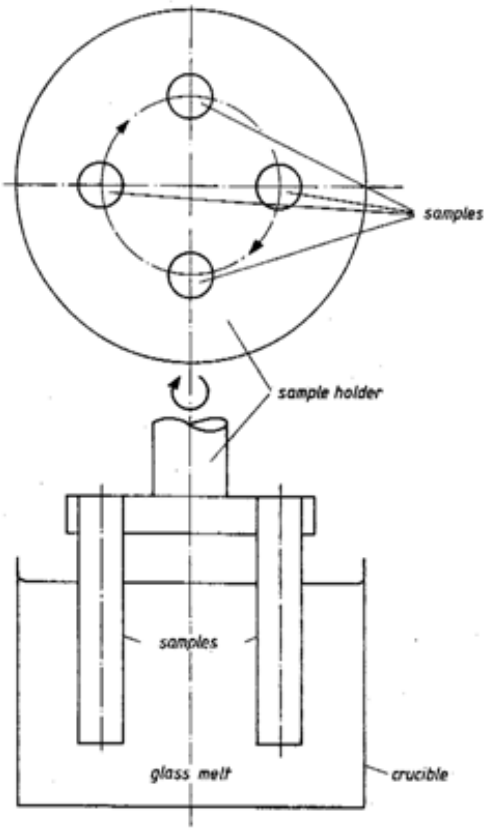

Figure 2.25: Dynamic finger test. From Dunkl[7]

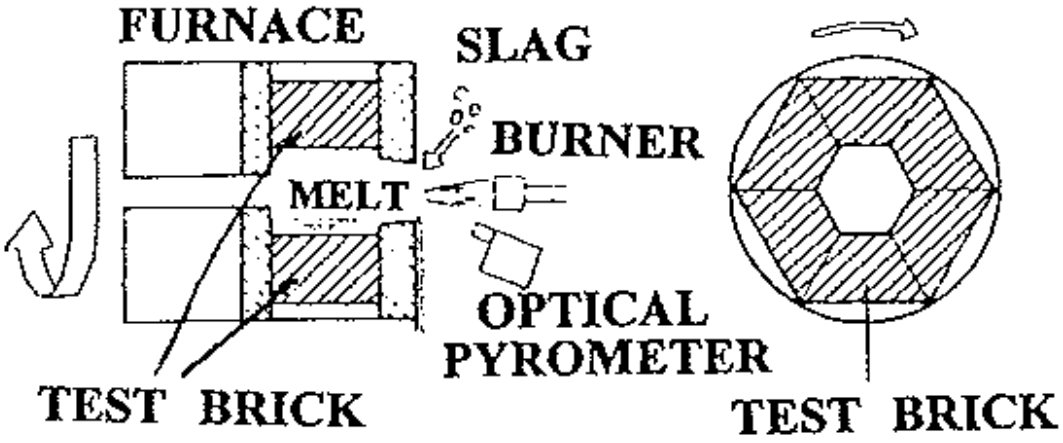

Figure 2.26: Rotary slag test. From Lee and Zhang[8]

2.5.2 Sessile drop test

Figure 2.17 shows the sessile drop test, also known as the button test[8]. Slag is placed on a refractory substrate, heated to a desired temperature and held for a fixed amount of time, allowing the slag to wet and react with the refractory. Generally, this technique is used to measure interface and surface energies in systems where the liquid is fluid and does not react with the solid. In the case of refractory wear testing, the energy calculations become more complicated as the hot, viscous slag will react with the refractory substrate.

2.5.3 Crucible test

The crucible test, also known as the cup, cavity or brick test[8], is shown in Figure 2.18. A crucible is made out of the refractory material which is to be tested, and the cavity is filled with slag. Typical cavity measurements[7] are diameter 40 – 50 mm and height 80 – 100 mm. Crucible wall thickness should be 10 mm or larger. Thermocouples can be inserted into the crucible wall or in the cavity for temperature control. The crucible is heated to the desired test temperature and held at this temperature for a fixed period of time. Upon desired high temperature exposure, the crucible is cooled and cut, and refractory wear is inspected and quantified. Attack by the molten slag is usually evaluated measuring the change in cavity diameter and through SEM and XRD investigations.

Due to the isothermal nature of the crucible test, it does not fully resemble the situation in an industrial furnace. Chemical wear as well as structural spalling due to slag penetration and structure densification can be evaluated, but since the refractory crucible is heated from all sides during the test, the establishment of a temperature gradient is prevented. The crucible test is therefore not suitable for thermal spalling investigations, since it has been established that a temperature gradient is responsible for this wear mechanism[6]. Other drawbacks utilizing this method are rapid saturation of slag composition with reaction products and lack of slag flow, restricting wear due to erosion and abrasion. Nevertheless, the crucible test is preferred in many cases due to its simplicity and ease of repeatability.

2.5.4 Static finger test

During the static finger test, also known as the dipping or immersion test[8], isothermal chemical wear of refractories is simulated through immersion of one or more cylindrical or square "fingers" in a molten slag bath. Upon being exposed to the corrosive bath for the desired period of time, the "fingers" are pulled out, and the melt is allowed to drip off at test temperature before sample cooling and inspection. Figure 2.19 shows the setup used by Dunkl[7], where four square rods having a cross section 10 x 10 $(mm)^2$ and length 100 mm were immersed 60 mm into the glass melt. Figure 2.20 shows the single rod setup described by Lee and Zhang[8]. ASTM standard C621-09[29] provides detailed test instructions.

Utilizing the static finger test, composition variation of the slag during the test can be minimized through a large slag volume compared to sample surface area. At the same time, the relatively small corrosion surface led to an upgrade of the static finger test to the static plate test described in the following chapter.

2.5.5 Static plate test

Dunkl[7] describes the static plate test visualized in Figure 2.21: Four platelets measuring 25 x 10 x 100 $(mm)^3$ are immersed 60 mm into a glass melt and held for a period of time. Upon cooling and cutting, refractory wear can be evaluated through microscopy or photography.

According to Dunkl, the static plate test can be used to identify wear due to interfacial convection and free density convection. Possible wear profiles are shown in Figure 2.27. In Figure 2.27a), refractory wear has taken place mostly at the slag-gas interface due to density differences between glass melt, refractory and glass melt saturated with refractory components; glass melt being the lightest. The driving force is known as interfacial convection. Figure 2.27b) shows a situation where the driving force for wear is free density convection. Flow is initiated downwards in the melt as a result of density differences. In this

case, the glass melt is heavier than the refractory and the glass melt saturated in refractory components.

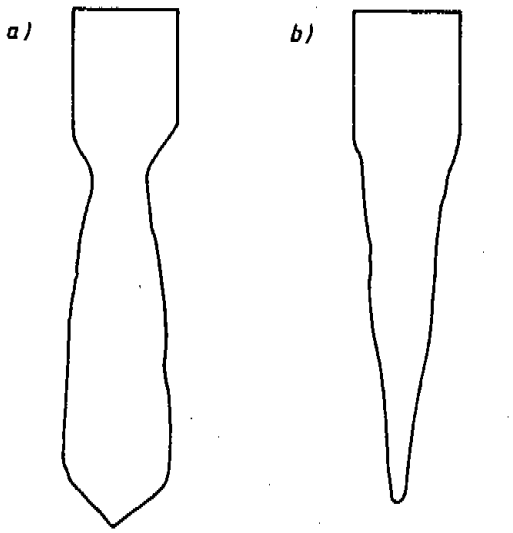

Figure 2.27: Platelets after static plate test. a) Wear due to interfacial convection. b) Wear due to free density convection. From Dunkl[7]

2.5.6 Induction furnace test

In the induction furnace test, shown in Figure 2.22, slag and metal are melted through induction heating in a polygonal crucible[8]. A temperature gradient can be established, and the atmosphere can be controlled easily. Slag-metal interface wear can be effectively simulated using this technique. Some fluid motion is obtained due to the nature of the induction furnace, although the flow cannot be controlled. This represents the main drawback of this method, otherwise simulating the situation in an industrial furnace effectively.

2.5.7 Small rotating furnace test

During the small rotating furnace test shown in Figure 2.23, 12 crown brick shaped refractory samples are tested simultaneously in a rotating experimental tank for 15 – 20 days[7]. The rotation ensures better temperature distribution, although the samples are still in static state relative to the glass melt. For composition control, the glass melt is replaced every sixth day. Upon cooling and cutting, samples are inspected and flux line depth, d, is quantified.

The rotating furnace test is a very expensive test due to its duration, and uncertainties related to accurate glass melt level upon slag replacement have been identified. Burner placements are also believed to negatively affect the results through increased corrosion at slag-gas interface.

2.5.8 Rotating finger test

Tomala and Basista[20] describe the rotating finger test visualized in Figure 2.24. A cylindrical "finger" with diameter 30 mm and length 230 mm is immersed in a molten bath and rotated at 100 rpm. After 1 hour the "finger" is rapidly pulled out of the liquid and cooled in inert gas. Upon cooling, the finger is cut and visually inspected. The strength of this method is the defined convection flow around the immersed part of the "finger", simulating relative motion of liquid slag and solid refractory not obtainable in a static test. Through removal of the boundary layer, refractory wear is increased.

Dunkl[7] describes a similar test known as the rotating cylinder face method, where a cylinder is rotated in a molten glass bath, and a Pt/Rh-probe measures the change in cylinder length as a function of time and at different rotation rates. Dunkl determined the change in cylinder length to be linear with time when stationary state had been reached, and found that the refractory wear rate increased with the square root of the rotation rate, $\sqrt{n}$. The rotating cylinder face method is especially useful for newly developed refractories, recognizing long term effects of glass melt immersion. A major drawback is high costs.

2.5.9 Dynamic finger test

Figure 2.25 shows the setup for the dynamic finger test, where cylindrical rods are immersed 60 mm into a glass melt and moved through it in a circular motion[7]. Typical rod measurements are diameter 18 – 22 mm and length 100 mm. After a desired refractory wear time, the melt is allowed to drip off at test temperature before sample cooling, cutting and inspection. Wear can be evaluated as change in diameter, immersed volume or through flux line depth measurements.

Due to different flow velocities, refractory wear will be highest on the outside of the rods. The corroded and eroded rods will therefore have an oval horizontal shape after the experiment, making evaluation of the geometrical profile difficult. Another major drawback utilizing the dynamic finger test is the short distance between the samples, resulting in mutual influence of the flow fields and contact between samples and dissolved material from other samples.

2.5.10 Rotary slag test

The rotary slag test is claimed to be one of the most popular wear tests for refractory materials[8]. For this test, a horizontally rotating cylindrical drum lined with refractory sections is utilized, as visualized in Figure 2.26. The drum is typically 450 mm long, has an internal shell diameter of 250 mm and is lined with six refractory samples[6]. Crushed slag is melted with an oxypropane flame and interacts with the refractory sections. The slag is refreshed periodically in order to control the composition and fluidity of the melt. Another advantage utilizing this test is time efficiency, as several different refractory materials are usually tested simultaneously. A temperature gradient can be established through firing the drum from one end, although it can be difficult to control accurately.

ASTM standard C874-99[30] provides more detailed instructions for the rotary slag test.

2.5.11 Reproducibility

In order to obtain representative results from refractory wear testing, good reproducibility is required. Dunkl[7] defines reproducibility as *maximum deviation of measured values within several test series relative to the average values*, in correspondence with equation (2.38):

$$\text{Reproducibility} = \pm \max\left[\textit{refractory wear}(i) - \frac{1}{n}\sum_{i=1}^{n} \textit{refractory wear}(i) \right] \qquad (2.38)$$

Through different refractory wear tests exposing a high-alkali-silicate glass melt to a fused-cast AZS 41 material consisting of corundum, Al_2O_3, and baddeleyite, ZrO_2, Dunkl calculated the reproducibility of each test. Table 2.6 presents the calculated reproducibilities, average fluxline depths, $\overline{d}$, and average decrease in length, $\overline{\Delta l}$.

Refractory wear tests conducted in electrical furnaces generally give better reproducibility than tests conducted in gas furnaces[7]. According to Table 2.6, the crucible test conducted in

an electric furnace with optical evaluation of slag attack was shown to have the best reproducibility, that is, the lowest maximum deviation from the average wear value. High costs and time requirements suppress the good reproducibility of the rotating cylinder face method and the small rotating furnace test, while difficult geometric profile evaluation represents a major drawback for the dynamic finger test.

Table 2.6: Reproducibilities for different refractory wear tests. From Dunkl[7]

Test	Atmosphere/Evaluation	Reproducibility	Refractory wear
Dynamic finger test	Gas furnace, mechanical evaluation	±10 %	$\overline{d}$ = 2 mm
Rotating cylinder face method	Electric furnace, probe evaluation	±8 %	$\overline{\Delta l}$ = 0.5 – 1.0 mm
Small rotating furnace test	Gas furnace, mechanical evaluation	±10 %	$\overline{d}$ = 9 mm
Crucible test	Gas furnace, mechanical evaluation	±38 %	$\overline{d}$ = 1 mm
	Gas furnace, optical evaluation	±20 %	$\overline{d}$ = 1 mm
	Electrical furnace, mechanical evaluation	±17 %	$\overline{d}$ = 0.6 mm
	Electrical furnace, optical evaluation	±6 %	$\overline{d}$ = 0.6 mm
Static finger test	Gas furnace, mechanical evaluation	±30 %	$\overline{d}$ = 1.3 mm
	Electrical furnace, mechanical evaluation	±15 %	$\overline{d}$ = 1 mm
Static plate test	Electrical furnace, optical evaluation	±10 %	$\overline{d}$ = 1 mm

In order to determine how sample geometry affects static wear test reproducibility, Dunkl conducted experiments exposing “fingers”, plates and crucibles of fused-cast AZS 41 material to sodium-silicate glass at 1450°C in an electric furnace for 72 hours. Table 2.7 presents the results:

Table 2.7: Sample geometry influence during static refractory wear testing. From Dunkl[7]

Sample geometry	$\overline{d}$ [mm]	Reproducibility [%]
Plates	1.6	±2
“Fingers”	1.0	±14
Crucibles	1.0	±8

Based on the results in Table 2.7, Dunkl claims that the static plate test shows high and real refractory wear at isothermal conditions due to a relatively large flow surface allowing an optimal development of convection flow. In spite of its good reproducibility, the crucible test does not reflect the real corrosion rate to the same extent due to a small glass melt volume to refractory surface area. Also, the glass melt becomes depleted of alkalis very quickly in the crucible test due to alkali diffusion, resulting in a too low attack. “Fingers” show lower refractory wear than the plates due to non-optimum development of convection flow as a result of a small refractory surface. Dunkl therefore recommends the use of the static plate test as the standard refractory wear test for selection of refractories for glass tanks based on good reproducibility, several advantages and no observed disadvantages.

2.6 Earlier work

2.6.1 Effect of microporosity

A microporous refractory is characterized by 90 % of the pores having a diameter less than 1 μm, as described in Chapter 2.3.2. Tomala & Basista[20] investigated the effect of microporosity in C-based refractories, and claim that microporous carbon generally provides better resistance to attack by liquid metal and alkalis than standard carbon: During rotating finger experiments conducted in argon, Ar, atmosphere, the researchers observed no refractory wear when cylindrical microporous carbon was rotated at 100 rpm in a 1470°C FeMnSi bath for 1 hour. In a FeMnC bath, some refractory wear was observed on both regular carbon and microporous carbon. Microporous carbon was also shown to have better resistance to water oxidation than standard carbon. Finally, Tomala & Basista claim that microporous carbon materials are resistant against alkali attack, while alkali attack takes place on standard carbon in the temperature range 800 - 1100°C.

2.6.2 Alkali attack, carbon monoxide deterioration and thermal shock

Silva et al.[22] investigated wear mechanisms for C hearth refractory lining utilized in blast furnaces. Two different C-refractories were investigated, characterized in Table 2.8:

Table 2.8: Carbon refractories investigated by Silva et al.[22]

Sample	Component 1	Component 2	Matrix
Anthracitic	80% anthracite, low crystallization degree	20% graphite	Amorphous carbon, high ash high permeability
Super-micropore	50% anthracite, low crystallization degree	50% graphite, high crystallization degree	Amorphous carbon, low ash low permeability

Alkali attack was investigated through comparative tests where the refractory samples were subject to attack by an alkaline steam or in direct contact with molten K_2CO_3. Figure 2.28 shows the K_2O concentration in the samples after alkaline steam attack at different temperatures, and Figure 2.29 compares K_2O absorption after alkaline steam attack and alkaline attack by liquid phase for anthracitic and supermicropore C-refractories:

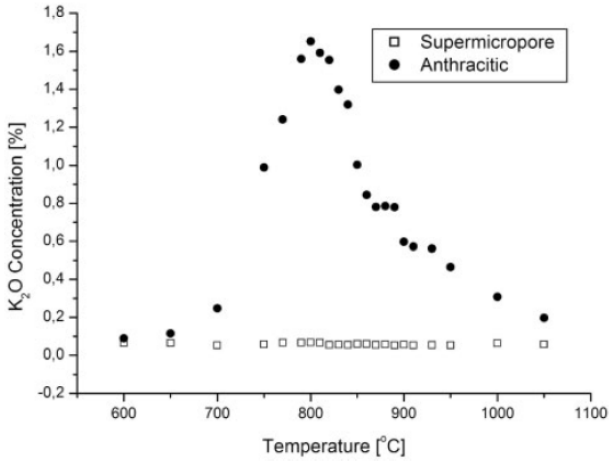

Figure 2.28: K_2O concentration in refractory samples after alkaline steam attack

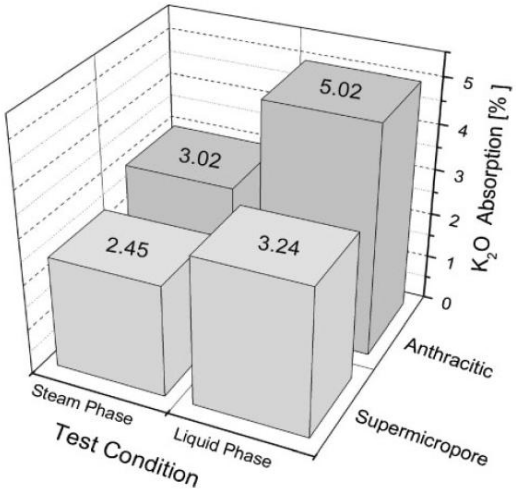

Figure 2.29: K_2O absorption in refractory samples from steam and liquid

From Silva et al.[22]

Silva et al. claim that alkali incorporation takes place mainly via free silica in the ash. The low ash content and low permeability of supermicropore C thus explains the low K_2O absorption in the material. Figure 2.28 supports claims[20,5] that alkali attack is most prominent in the temperature range 800 – 1100°C for anthracitic C. Figure 2.29 shows that potassium absorption is higher for alkaline attack via liquid phase for both supermicropore and anthracitic C-refractories, and that supermicropore C generally absorbs less alkalis than anthracitic C.

Carbon monoxide deterioration was investigated through CO(g) exposure followed by bending resistance tests in accordance with ASTM standard C-288/78[31] and ABNT standard NBR-6113/90. Based on the test results, Silva et al. claim that anthracitic C-refractories are more susceptible to CO(g) deterioration than supermicropore C-refractories.

Thermal shock tests showed that both anthracitic and supermicropore C-refractories exhibit excellent thermal stress resistance, as suggested in Chapter 2.3.2.

3. Experimental

3.1 Equipment and raw materials

Compatibility experiments described in Chapter 2.5 were conducted in a Carbolite PVT 18/80 vertical tube furnace with an Al_2O_3 tube resistance heated by six lanthanum chromite, $LaCrO_3$, heating elements. Prior to experimental start-up, the furnace was repaired and tube fittings redesigned in order to make the furnace operable and suitable for refractory testing. Furnace setup is shown in Figure 3.1, and a principle drawing of the Carbolite tube furnace is presented as Figure A.3 in Appendix A.2. Work drawings for tube fittings are shown as Figures A.4 through A.7 in Appendix A.2.

Figure 3.1: Furnace setup including (from left) mass flow controller, furnace controller and Carbolite tube furnace. On the floor: Zirconium gas purifier.

5 different refractory materials utilized in a SiMn production furnace were tested against process materials conducting crucible and static plate tests, described in Chapters 2.5.3 and 2.5.5, respectively. Table 3.1 classifies and describes the industrial usage of the different raw materials investigated:

Table 3.1: Raw materials

Raw material	Industrial usage	Classification
SiC tap block	Tap block	Refractory
Carbon tap clock	Tap block	Refractory
Electrode paste	Tap hole maintenance	Refractory
Ramming paste	Tap block repair	Refractory
Tap hole clay	Tap hole plugging	Refractory
SiMn slag I	Metal refining	Process material
SiMn slag II	Metal refining	Process material

Raw material analyses are presented in Table A.1 through Table A.8 in Appendix A.3.

Slags were analyzed utilizing X-ray Diffraction(XRD) and X-ray fluorescence(XRF) at Department of Geology, University of Pretoria. XRD-samples were crushed, milled and analyzed using a PANalytical X'Pert Pro powder diffractometer with X'Celerator detector and variable divergence- and receiving slits with Fe filtered Co-Kα radiation. Phases were identified using X'Pert Highscore plus software. Quantification of amorphous material was done through addition of 20 % Aldrich 99 % pure Si. A study utilizing a JSM-6300 Scanning Electron Microscope (SEM) at Industrial Metals and Minerals Research Institute (IMMRI) supported and confirmed the XRD-results. XRF-samples were crushed, milled, prepared as powder briquettes and analyzed utilizing an ARL 9400XP+ XRF spectrometer and the Uniquant software. Tables A.1 and A.2 in Appendix A.3 present results from XRD and XRF analyses of slag samples, respectively.

Based on XRD and XRF analyses and typical SiMn slag compositions[1] presented in Table 2.4 in Chapter 2.4.5, SiMn slag samples I and II were selected for use during experiments. 5-component slag compositions, basicities calculated in accordance with equation (2.32) in Chapter 2.4.5, viscosities estimated utilizing the Tang & Tangstad model[25] and liquidus temperatures estimated utilizing FactSage^{TM} 6.2[32] are presented in Table 3.2:

Table 3.2: Compositions, basicities, estimated viscosities and liquidus temperatures for slags utilized

Slags	**Component [wt%]**					**Basicity,B**	**Estimated viscosity[25] [poise]**		**Estimated liquidus temperature[32] [°C]**
	SiO_2	**Al_2O_3**	**CaO**	**MgO**	**MnO**		**1500°C**	**1600°C**	
SiMn slag I	42.1	20.9	22.4	6.9	7.7	0.465	7.1	3.9	1310.54
SiMn slag II	41.8	20.0	29.0	6.2	3.1	0.570	5.9	3.2	1295.84

Only minor differences in slag behavior in contact with refractories were expected, based on data from Table 3.2. In order to enhance complete melting during experiments, SiMn slags I and II were crushed and milled to d_{80} = 400 μm and d_{80} = 320 μm, respectively.

SiC tap block and green tap hole clay ashes were analyzed utilizing XRD. Results are presented in Table A.3 and A.4 in Appendix A.3, respectively.

Carbon tap block, electrode paste, ramming paste and tap hole clay A were analyzed utilizing short analysis techniques and LECO combustion analysis at Advanced Coal Technology, Pretoria. Short analysis quantifies moisture content, ash content and volatile matter content. %Carbon was quantified utilizing a LECO CS230SH. The remaining ash was analyzed utilizing XRD and XRF at Department of Geology. Results from short analyses and ash analyses are presented in Table A.5, A.6 and Table A.7 in Appendix A.3, respectively.

SiMn metal samples were analysed for reference purposes at an external laboratory, utilizing potentiometric, gravimetric and LECO methods. Results are presented in Table A.8 in Appendix A.3, and correspond reasonably well with typical alloy specifications[1] presented in Table 2.1 in Chapter. 2.1.2.

3.2 Crucible and plate manufacture

Crucibles with outer diameter 65 mm and height 70 mm were manufactured from the refractory materials. Side wall thickness was 20 mm and bottom thickness was 25 mm, leaving a cavity of approximately 22 cm^3 to be filled with process materials during tests. Depending on the material properties, different techniques were utilized in order to

manufacture the crucibles and will be described in this chapter. Forming a crucible from electrode paste proved challenging, so based on discussions in Chapter 2.5, static plate tests replaced crucibles tests for this refractory material. Detailed work drawings can be found as Figures A.8 through A.10 in Appendix A.4.

SiC and carbon tap block crucibles, shown in Figures 3.2 and 3.3, were core drilled and machined from SiC and carbon tap block bricks measuring 25 x 12 x 7 cm, respectively.

Figure 3.2: SiC tap block crucible

Figure 3.3: Carbon tap block crucible

Ramming paste and tap hole clay crucibles required an outer graphite shell to support the refractory crucible during baking, as visualized in Figures 3.4 and 3.5. Tap hole clay crucibles were manufactured through shaping of tap hole clay by hand into the prefabricated graphite shell. A dowel was utilized to manufacture ramming paste crucibles through ramming of the refractory material into the graphite shell.

Figure 3.4: Tap hole clay crucible

Figure 3.5: Ramming paste crucible

Upon manufacture, the green refractory crucibles were baked in inert atmosphere in the muffle furnace shown in Figure 3.6. Inert atmosphere was obtained through covering the crucibles with C pellets in a steel can with lid visualized in Figure 3.7. Detailed baking procedures are presented in Table 3.3; based on refractory manufacturer recommendations and industrial temperature profiles.

Figure 3.6: Muffle furnace

Figure 3.7: Baking setup

Table 3.3: Baking procedures for C-based refractories

Refractory material	**Baking temperature [°C]**	**Heating rate [°C/min]**	**Holding time [hours]**
Tap hole clay	800	40	4
Ramming paste	950	40	0.5
Electrode paste	500	20	24

Thin plates with height 60 mm, width 20 mm and thickness 5 mm were cut from electrode paste using a diamond saw. Upon cutting, the plates were baked in accordance with Table 3.2, cooled and finally polished using sand paper. An electrode paste plate is visualized in Figure 3.8:

Figure 3.8: Electrode paste plate

3.3 Temperature profiles

Initially, temperature profiles in an empty furnace tube were obtained at set points 1500°C and 1520°C in N_2(g) atmosphere by moving a platinum – platinum 13 % rhodium, Pt/Pt13Rh, R-type thermocouple vertically in the center of the tube. Based on recorded temperature profiles, the ideal sample position during experiments could be determined. Temperature profiles at set points 1500°C and 1520°C are shown in Figures 3.9 and 3.10, respectively. Ideal sample positions are indicated in red.

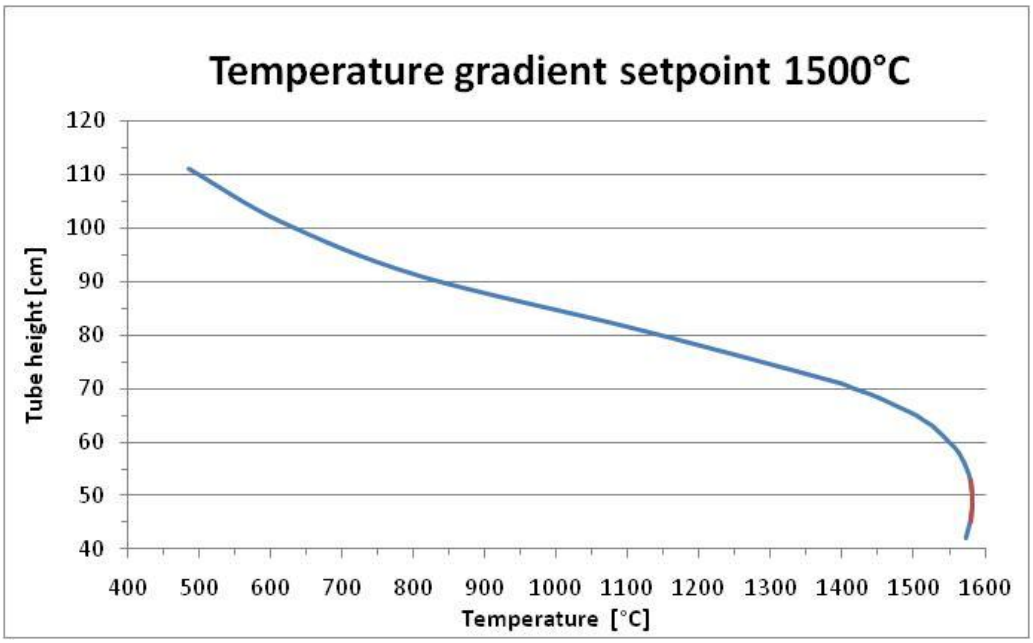

Figure 3.9: Temperature profile at set point 1500°C. Ideal sample placement is shown in red.

From Figure 3.9 it can be observed that the stabile temperature area at set point 1500°C was found 45 – 53 cm from the tube bottom. In this area, the temperature varied in the range 1580 – 1583°C. A temperature offset of 83°C between controller thermocouple and external R-thermocouple was measured. This was most likely due to controller thermocouple placement. Set point 1520°C was chosen based on this knowledge.

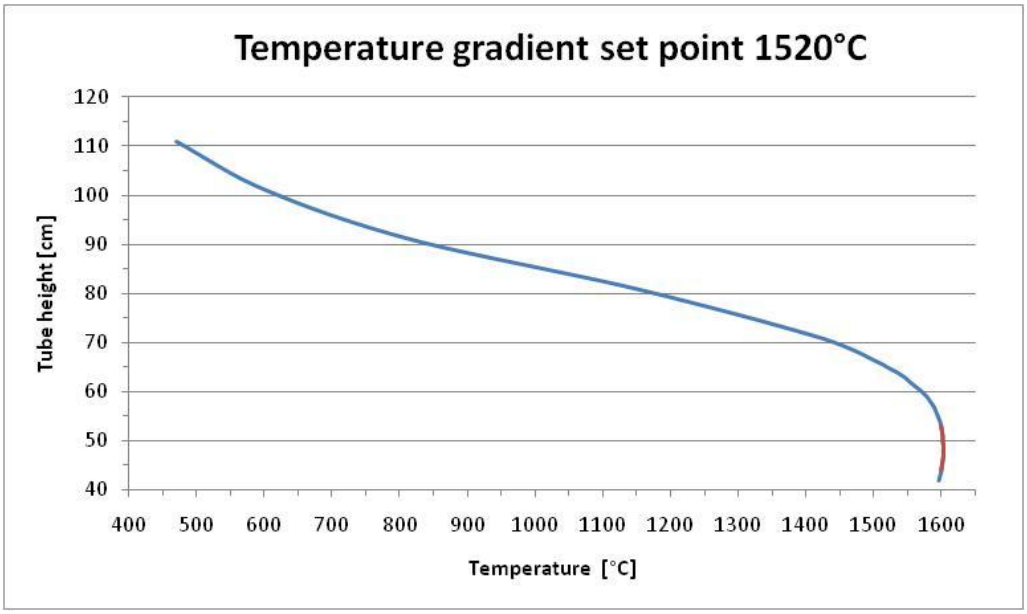

Figure 3.10: Temperature profile at set point 1520°C. Ideal sample placement is shown in red.

At set point 1520°C, the stabile temperature area was found 44 – 53 cm from the tube bottom, visualized in Figure 3.10. In this area, the temperature varied in the range 1600 – 1603°C.

3.4 Temperature validations

During the experimental work, a communication error within the temperature logging system was discovered, calling for a recalibration of the temperature logger followed by temperature validations. The wire-bridge method[33] was utilized to quantify the error in the temperature logging system at the melting points of gold, Au, and palladium, Pd. Crovini et al.[34] conducted an interlaboratory study comparing the wire-bridge Au and Pd calibrations with optical pyrometer calibrations. Agreement within 0.7 K for Au and 1.5 K for Pd was achieved amongst three laboratories, showing that the wire-bridge method can be considered adequately accurate for this investigation.

Utilizing the wire-bridge method, an R-type thermocouple hot junction was constructed by mechanically clamping a piece of pure metal wire to the ends of Pt/Pt13Rh thermocouple wires, shown for Au in Figure 3.11 - left. Heating this reference thermocouple through the melting point of the pure metal wire resulted in thermocouple short circuiting, thus providing a simple, rapid and relatively inexpensive way of quantifying the offset in temperature readings from an R-thermocouple heated alongside the wire-bridge thermocouple[33].

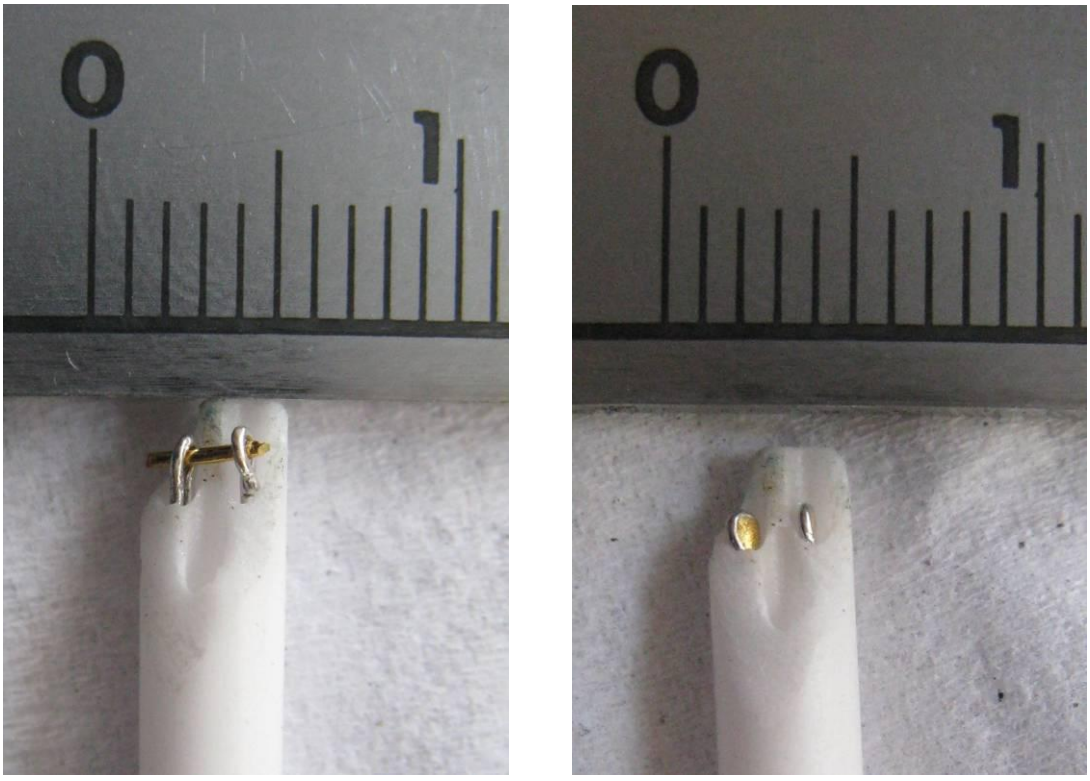

Figure 3.11: Au-wire bridge. Left: Before experiment. Right: After experiment

Figure 3.12 shows the temperature history during an experiment, heating the wire-bridge thermocouple and an R-thermocouple through the melting point of Au[35], 1064°C. The wire-bridge thermocouple, readings shown in red, was observed to short circuit after a short melting plateau at 1064°C, due to melting of the Au wire visualized in Figure 3.11 – right.

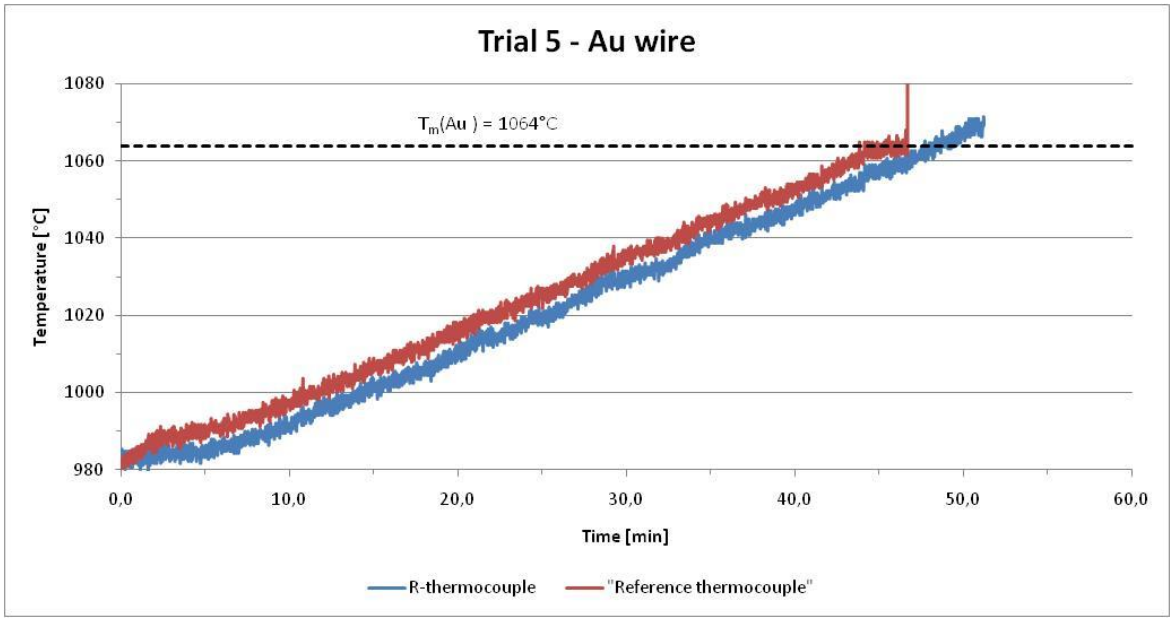

Figure 3.12: Temperature history during Au wire-bridge experiment

At 1064°C, an average temperature offset of -2.1°C ± 2.3°C was measured, and at the melting point of Pd[35], 1555°C, an average temperature offset of 0.2°C ± 0.4°C was measured. These results suggest increased temperature accuracy at higher temperatures.

3.5 Test procedures

3.5.1 Crucible tests

12 crucible tests were conducted as described in Chapter 2.5.3, investigating the compatibility between different combinations of refractory and process materials. Refractory crucibles, visualized in Chapter 3.2, filled with process materials were suspended in the furnace tube by a Φ = 3 mm molybdenum, Mo, wire connected to an Al_2O_3 support rod. Figure 3.13 shows the two different crucible setups utilized, and Figure 3.14 shows the furnace tube setup:

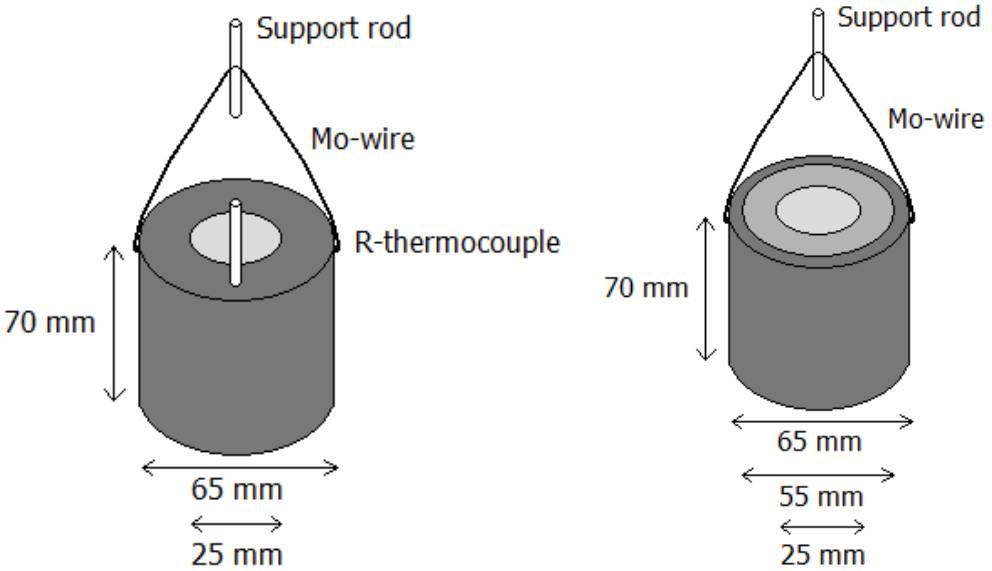

Figure 3.13: Crucible test setup.
Left: SiC and carbon tap block crucible.
Right: Ramming paste and tap hole clay crucible with graphite shell.

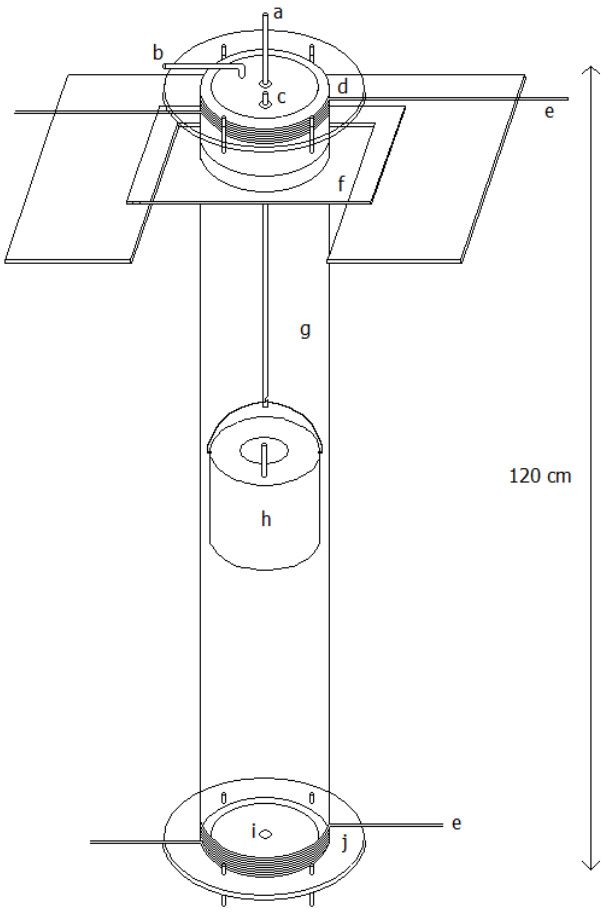

a – Al_2O_3 sample support rod, Φ = 10 mm
b – Gas outlet, Φ = 8 mm
c – R-type thermocouple (Pt/Pt13Rh), Φ = 8 mm
d – Brass top tube fittings
e – Copper coolers
f – Steel support plate resting on steel stand
g – Al_2O_3 furnace tube, Φ_{outer} = 91 mm, Φ_{inner} = 77 mm
h – Sample
i – Gas inlet, Φ = 6 mm
j – Brass bottom tube fittings

Figure 3.14: Furnace tube setup (not to scale)

The refractory crucibles were heated to high temperatures at 4°C/min in Ar(g), atmosphere and were held for a certain time before being cooled, filled with epoxy, cut and inspected. Due to the use of graphite support crucibles, and since the industrial slags contained metal prills, the p_{O2} in the system was fixed, rendering the need to accurately control or manipulate the p_{O2} in the furnace tube unnecessary. In order to avoid extensive oxidation of graphite support crucibles during experiments, low p_{O2} was ensured through purification of Ar(g); oxidizing zirconium, Zr, turnings at 300°C in correspondence with equation (3.1). Figure A.11 in Appendix A.5 presents p_{O2} data from an experiment holding a ramming paste crucible at 1367°C for 4 hours.

$$Zr(s) + O_2(g) = ZrO_2(s) \tag{3.1}$$

Before the start of each experiment, the system was purged with purified Ar(g) at 2388 mL/min for 15 minutes. Upon starting the heating programme, the Ar(g) flow rate was reduced to less than 390 mL/min, and was maintained below this rate throughout the length of the experiment.

Table 3.4 shows the different combinations of refractory and process materials investigated, as well as the respective holding temperatures and times. Holding temperatures were initially chosen to simulate industrial furnace tapping conditions where slags hold a temperature of 1500 – 1600°C[1]. Due to the communication error in the temperature logging system, temperatures were verified to be ~133 – 136°C lower than initially measured. Based on

liquidus temperature estimates presented in Table 3.2 in Chapter 3.1, both slags were still expected to reach liquid state during all experiments.

Table 3.4: Crucible tests

Experiment	Crucible material	Filler material	Holding temperature [°C]	Holding time [hours]
C.1a)	Ramming paste	SiMn slag I	1367	2
C.1b)	Ramming paste	SiMn slag I	1367	4
C.1c)	Ramming paste	SiMn slag I	1464	4
C.1d)	Ramming paste	SiMn slag I	1600	4
C.2a)	Ramming paste	SiMn slag II	1367	2
C.2b)	Ramming paste	SiMn slag II	1464	4
C.3	SiC tap block	SiMn slag I	1464	4
C.4	SiC tap block	SiMn slag II	1464	4
C.5	C tap block	SiMn slag I	1464	4
C.6	C tap block	SiMn slag II	1464	4
C.7	Tap hole clay	SiMn slag I	1464	4
C.8	Tap hole clay	SiMn slag II	1464	4

The temperature histories during experiments C.1b), C.1c) and C.1d) are shown in Figure 3.15. Temperatures were recorded with a Pt/Pt13Rh R-type thermocouple ~1 cm above the top of the samples. Temperature histories are representative for all the experiments conducted at the three holding temperatures with holding time 4 hours.

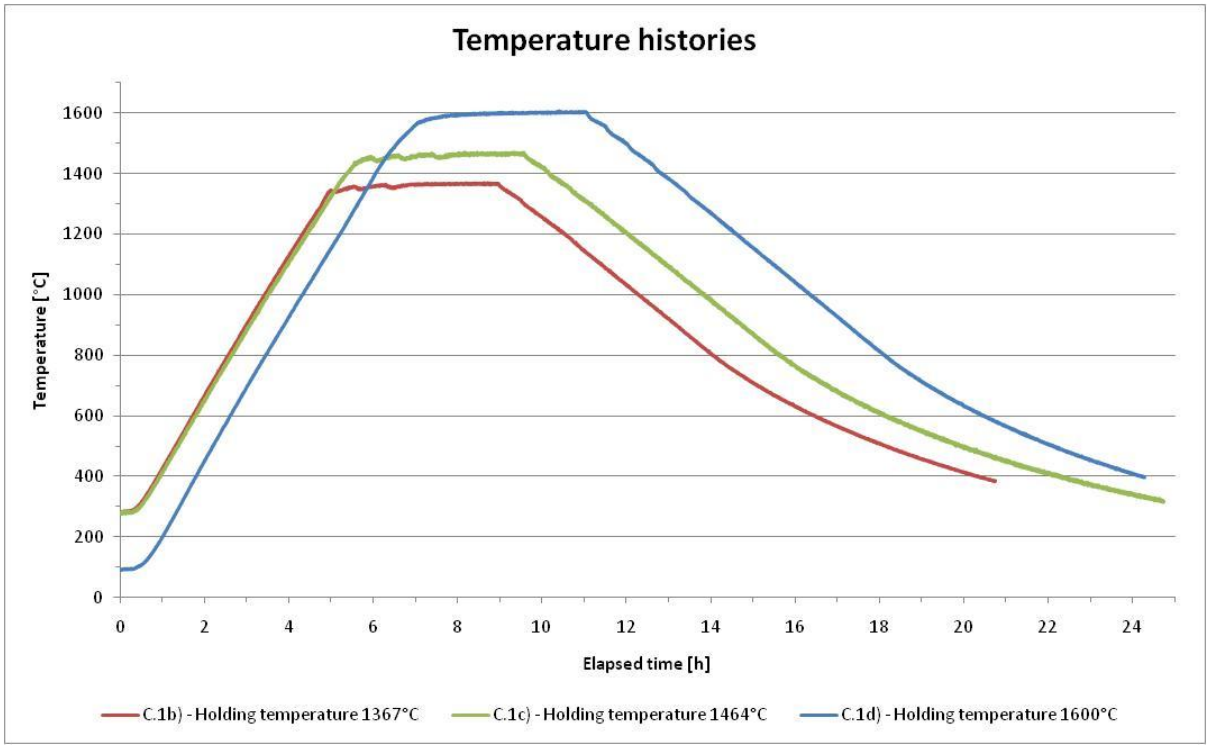

Figure 3.15: Temperature histories during experiments

After the experiments, the change in cavity diameter was quantified visually utilizing a vernier caliper. Selected areas were investigated further utilizing a Nikon Eclipse E200 optical microscope and a JSM-6200 Scanning Electron Microscope at 15kV. Energy dispersive spectrometry (EDS) mode in the SEM was used to qualitatively identify different phases in

the samples and to give a rough quantitative element analysis. Results are presented in Chapter 4.1, and EDS analyses of slag, metal and SiC compositions are presented in Tables A.9 through A.15 in Appendix A.6.

3.5.2 Static plate tests

Due to challenging material properties described in Chapter 3.2, two static plate tests were conducted investigating the compatibility between thin electrode paste plates and process materials. Utilizing the same tube furnace as during the crucible tests, static plate tests were conducted in accordance with test description in Chapter 2.5.5. Material combinations and holding temperatures and times are presented in Table 3.5:

Table 3.5: Static plate tests

Experiment	Plate	Filler	Holding temperature [°C]	Holding time [hours]
P.1a)	Electrode paste	SiMn slag I	1464	2
P.2	Electrode paste	SiMn slag II	1464	4

Figure 3.16 shows the setup for the static plate tests. An electrode paste plate was submerged in a solid slag bath confined in a thick-walled graphite crucible. The crucible was heated to 1464°C and held for the desired time before cooling, cutting and inspection. The change in plate thickness was quantified utilizing a vernier caliper, and selected areas were investigated further utilizing a Nikon Eclipse E200 optical microscope and a JSM-6200 Scanning Electron Microscope at 15kV. Different phases were identified using EDS mode in the SEM, and a rough quantitative element analysis was acquired. Results are presented in Chapter 4.2, and EDS analyses of slag, metal and SiC compositions are presented in Tables A.9 through A.15 in Appendix A.6.

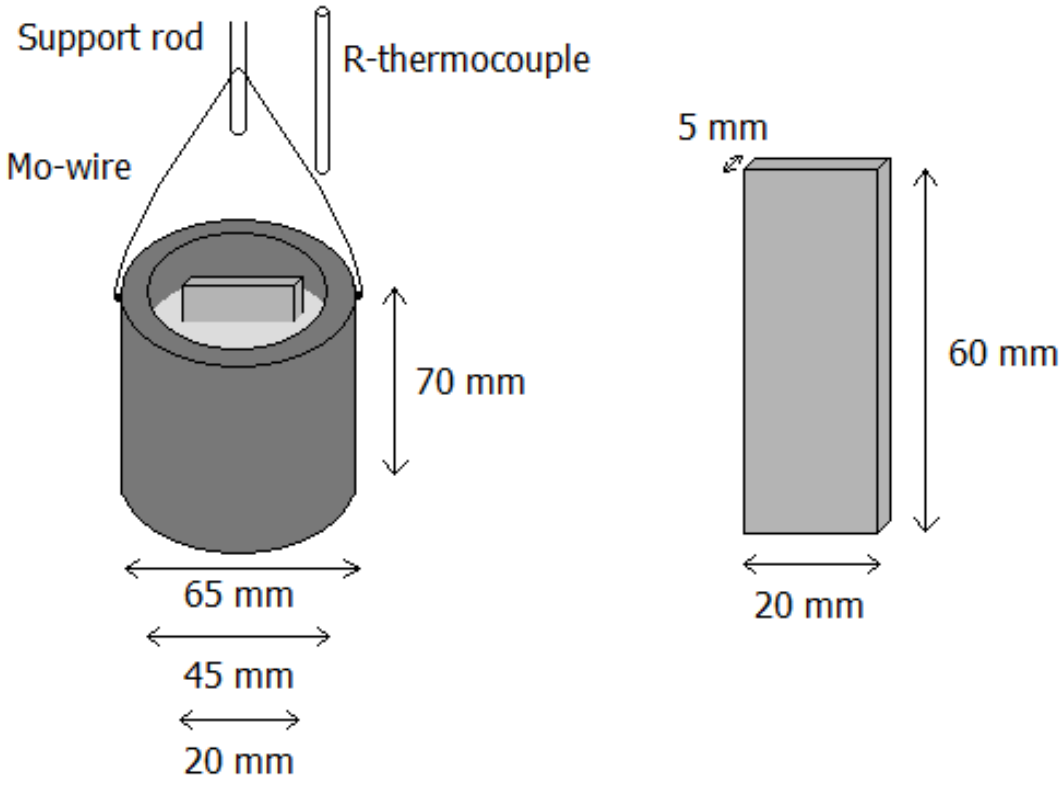

Figure 3.16: Static plate test setup. Left: Setup with graphite crucible. Right: Electrode paste plate

4. Results

4.1 Crucible tests

12 crucible tests were conducted investigating the interaction between process and refractory materials - of these eight unique combinations. In this chapter, the results from the different combinations will be presented. Tables A.9 through A.15 in Appendix A.6 present rough quantitative EDS analyses of slag, metal and SiC compositions.

4.1.1 Ramming paste VS SiMn slag I

Figure 4.1 shows the intersected crucibles after experiments C.1a) and C.1b):

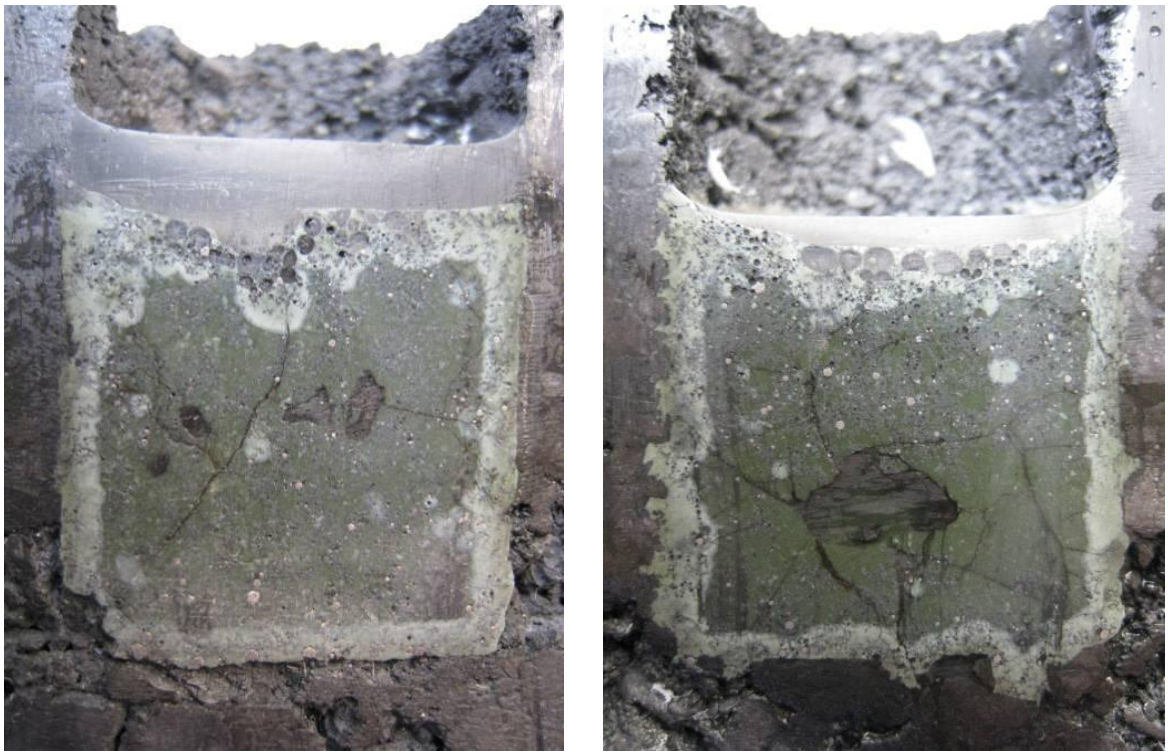

Figure 4.1: Intersected crucibles after experiments C.1a) (left) and C.1b) (right)

After two and four hours holding time at 1367°C, respectively, only a small degree of interaction between slag and refractory was observed. Difference in slag crystallinity between slag-refractory interface and center areas was observed macroscopically as different shades of green. Metal prills were embedded in the slag bulk, but were also found specifically at the slag-refractory interface. After experiment C.1a), metal prills were distributed evenly in the slag, while after experiment C.1b), a higher degree of concentration to top and bottom areas was observed. Gas pores were found close to the slag-gas interface after both experiments.

Upon increasing the holding temperature to 1464°C in experiment C.1c), slag penetration into the refractory wall was observed, visualized in Figure 4.2.

Slag penetration after experiment C.1c) was studied at higher magnification in an optical microscope, shown in Figure 4.3. Large pieces of refractory(1a) can be observed embedded in slag as a result of refractory disintegration upon slag penetration. In Figure 4.3, slag is light grey matrix phase(1b) in the top half of the image, while epoxy is dark grey(1c) in the bottom half of the image. Black areas(1d) are gas pores.

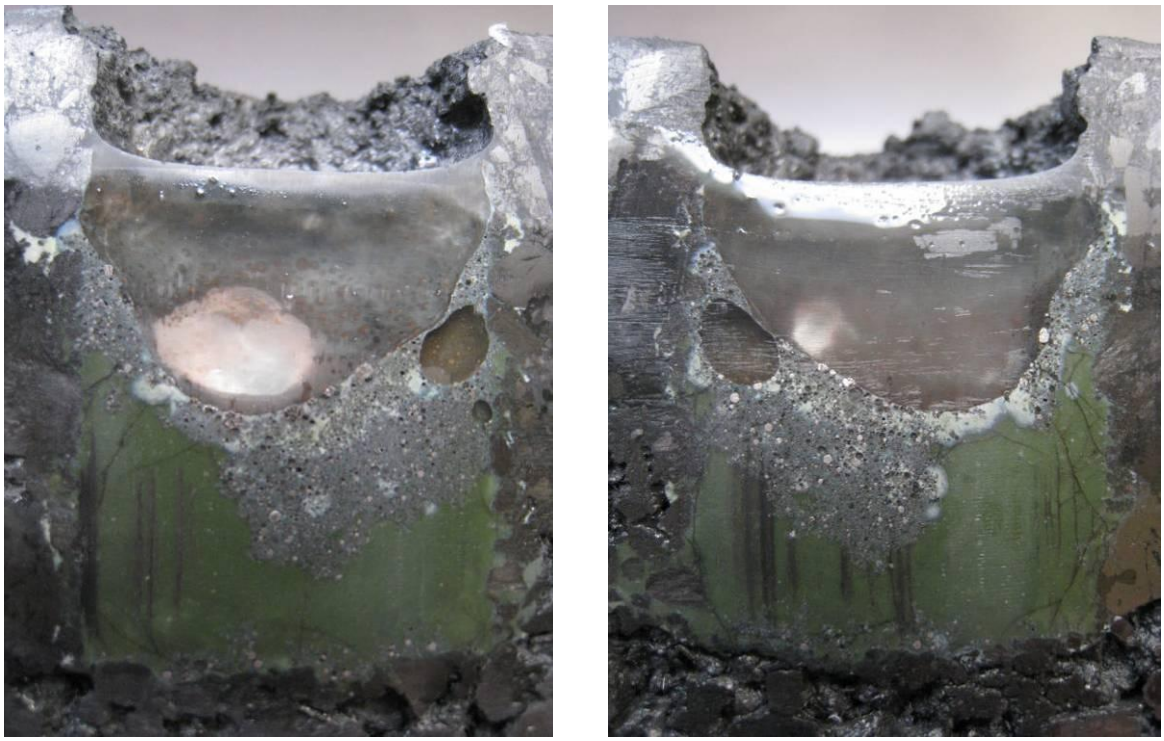

Figure 4.2: Intersected crucible after experiment C.1c)

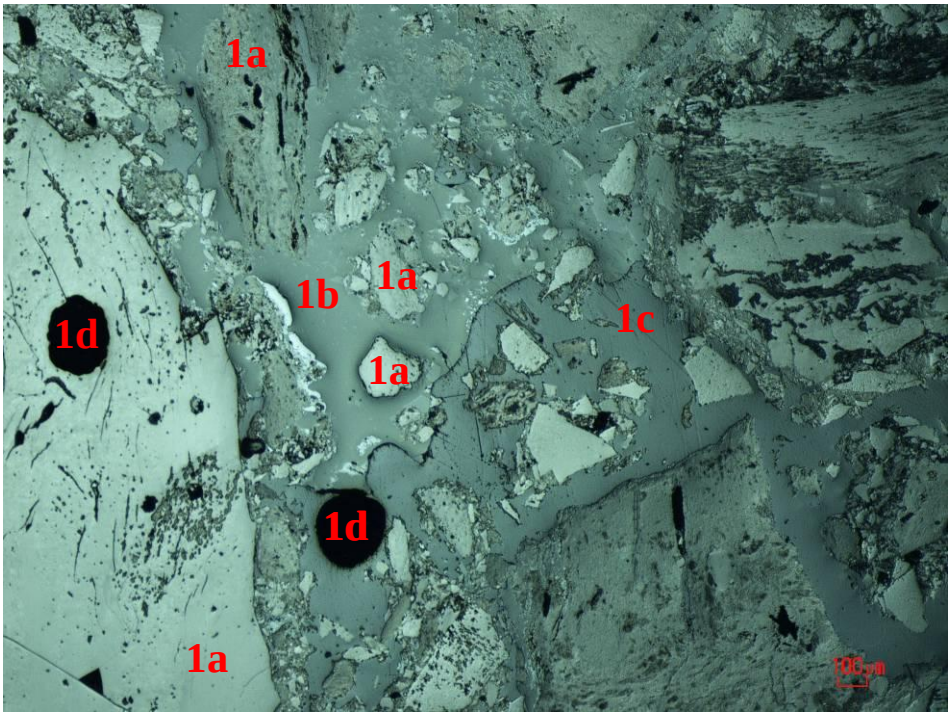

Figure 4.3: Slag-refractory matrix transition after experiment C.1c). Scale bar reads 100 µm.

Metal prills(2a) containing on average 51.5 wt% Fe, 36.0 wt% Mn and 12.1 wt% Si were found close to refractory particles(2b), surrounded by SiC(2c), visualized in the SEM backscatter image in Figure 4.4. According to Table A.10 in Appendix A.6, the MnO content in the slag close to the slag-refractory interface(2d) was reduced from 7.7 wt% to 1.5 wt% during the course of the experiment.

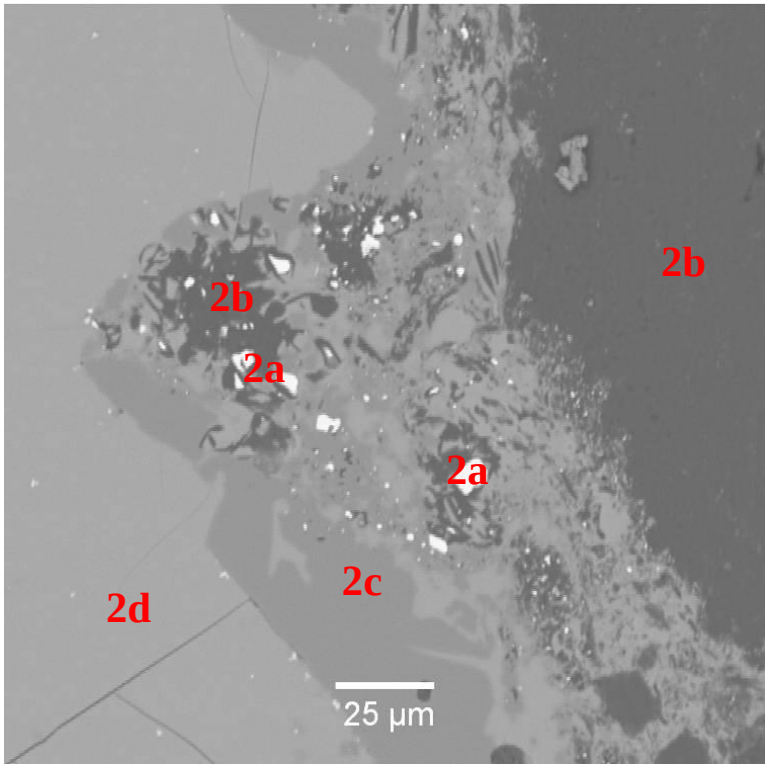

Figure 4.4: Slag-refractory particle transition after experiment C.1c)

The transition between green and grey areas close to slag-gas interface in Figure 4.2 is visualized at increased magnification in Figure 4.5:

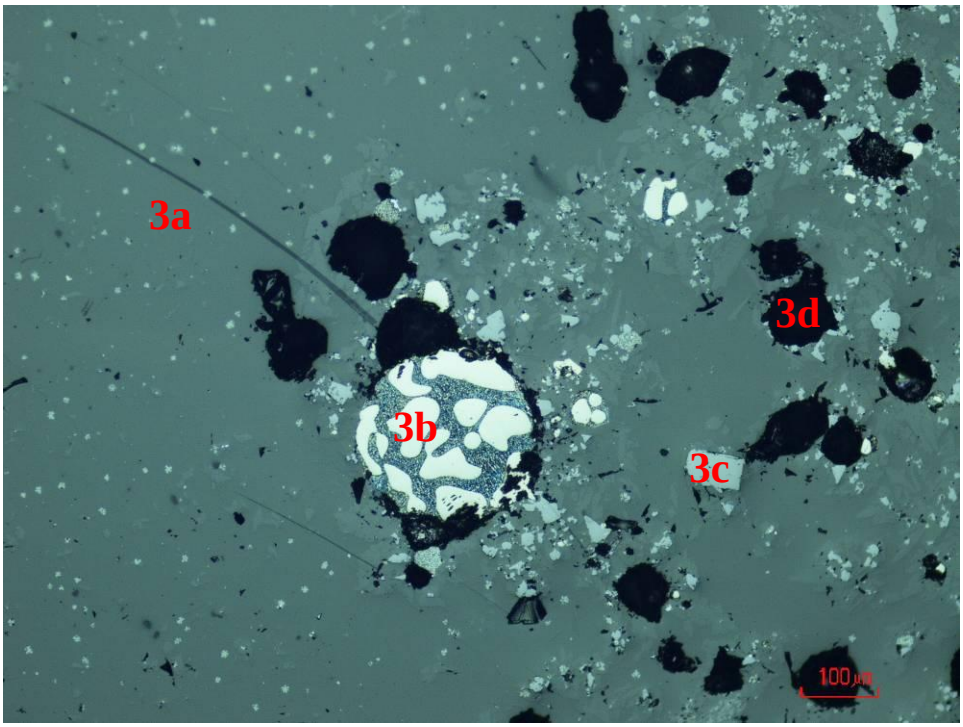

Figure 4.5: Green slag – grey area transition after experiment C.1c). Scale bar reads 100 µm.

To the left in Figure 4.5 is the bulk slag(3a) incorporating manganese sulphide, MnS, clusters and SiMn prills originally present in the slag. According to Table A.9 in Appendix A.6, an average bulk slag composition with a slightly reduced MnO content compared to fresh SiMn slag I was measured. To the right, metal prills(3b) with up to 86.8 wt% Mn incorporating

manganese carbides[36], Mn_xC_y, light grey SiC particles(3c) and many large and small gas pores(3d) were observed making up the rough, grey slag area in Figure 4.2.

Large metal prills found on the cavity bottom slag-refractory boundary are visualized in Figure 4.6:

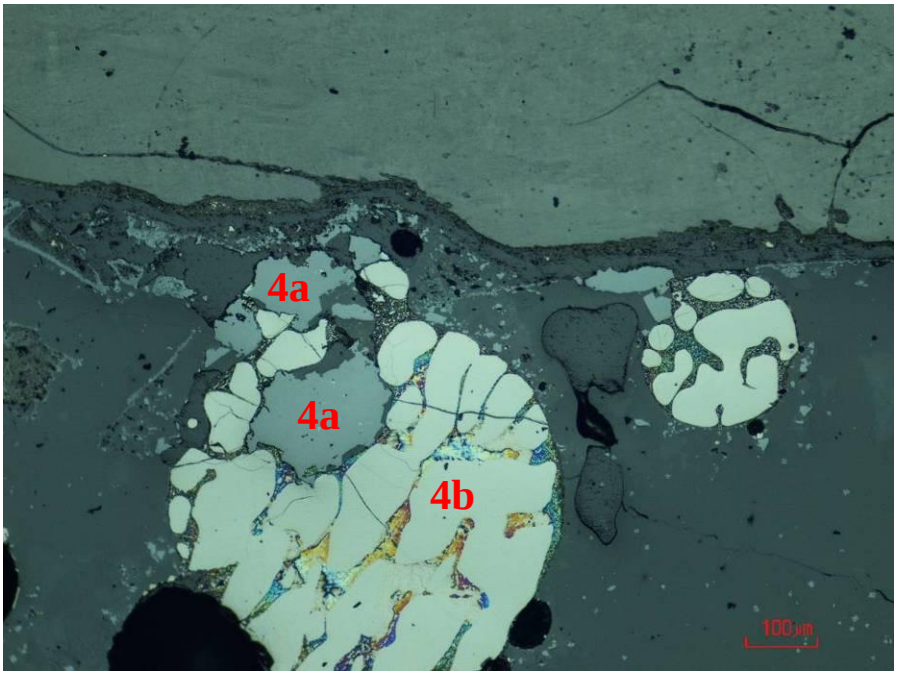

Figure 4.6: Metal prills on slag-refractory boundary after experiment C.1c). Scale bar reads 100 µm.

In Figure 4.6, grey SiC areas(4a) were observed in direct contact with white metal prills containing Mn_xC_y areas(4b). A metal composition of 76.8 wt% Mn, 17.6 wt% Si and 5.5 wt% Fe corresponds well with the composition of SiMn metal I presented in Table A.8 in Appendix A.3. An MnO concentration gradient from 3.1 wt% to 1.4 wt% was measured approaching the slag-refractory interface.

Figure 4.7 visualizes the change in cavity diameter as a function of height in the crucible during experiment C.1c). Red and blue dots represent inner crucible walls before and after the experiment, respectively. Percentages quantify change in cavity diameter at respective heights in the crucible. It can be observed that refractory wear was higher in the slag-gas interface area indicated by green lines. This trend was also confirmed microscopically.

Figure 4.8 shows the intersected crucible after experiment C.1d), holding the combination of ramming paste and SiMn slag I at 1600°C for 4 hours. After the experiment, metal prills were observed on the bottom of the crucible cavity, as well as hanging on the inside walls of an otherwise empty crucible. Upon cutting, a white phase was observed macroscopically inside crucible walls, having penetrated through the ramming paste all the way to the supporting graphite shell. The white phase is expected to contain both metal and slag phases.

Figure 4.9 visualizes the change in cavity diameter during experiment C.1d). Red and blue dots represent inner crucible walls before and after the experiment, respectively, while green triangles visualize the affected area after the experiment. The affected area includes the white areas inside the refractory wall observed in Figure 4.8. Percentages quantify the change in

affected diameter at respective heights in the crucible, comparing the size of the affected area after the experiment with the original crucible cavity measurements.

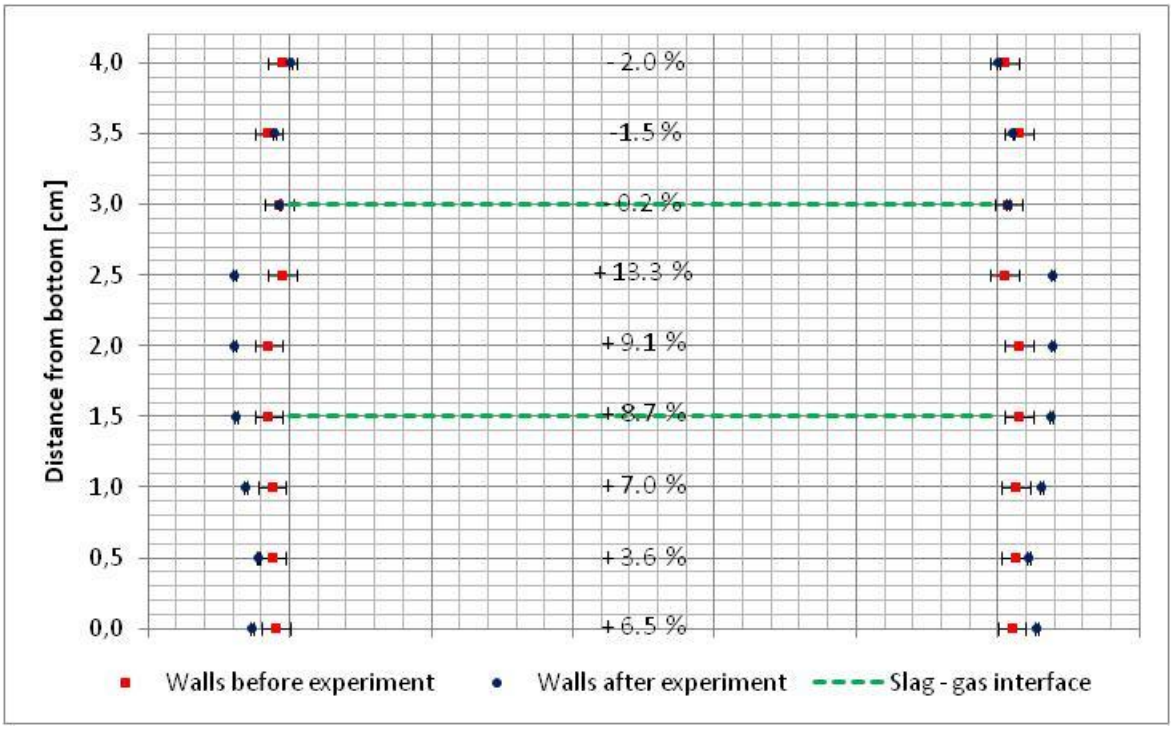

Figure 4.7: Wear profile experiment C.1c)

Figure 4.8: Crucible after experiment C.1d).
Left: Intersected crucible. Right: Close-up of left half.

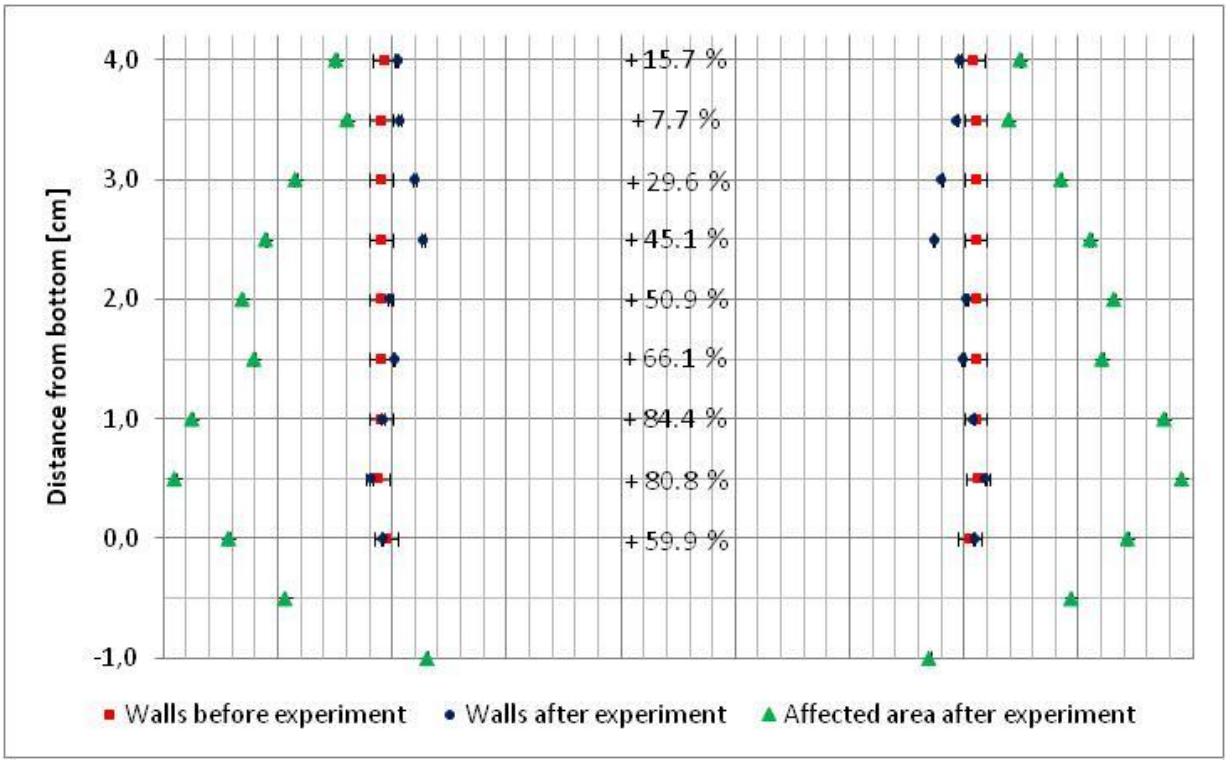

Figure 4.9: Wear profile experiment C.1d)

Figure 4.9 shows that the crucible cavity volume decreased due to metal formation on the cavity walls, and the affected diameter increased with almost 90 % due to slag and metal penetration. Sample C.1d) was not investigated further due to time limitations.

4.1.2 Ramming paste VS SiMn slag II

Figure 4.10 shows the intersected crucibles after experiments C.2a) and C.2b):

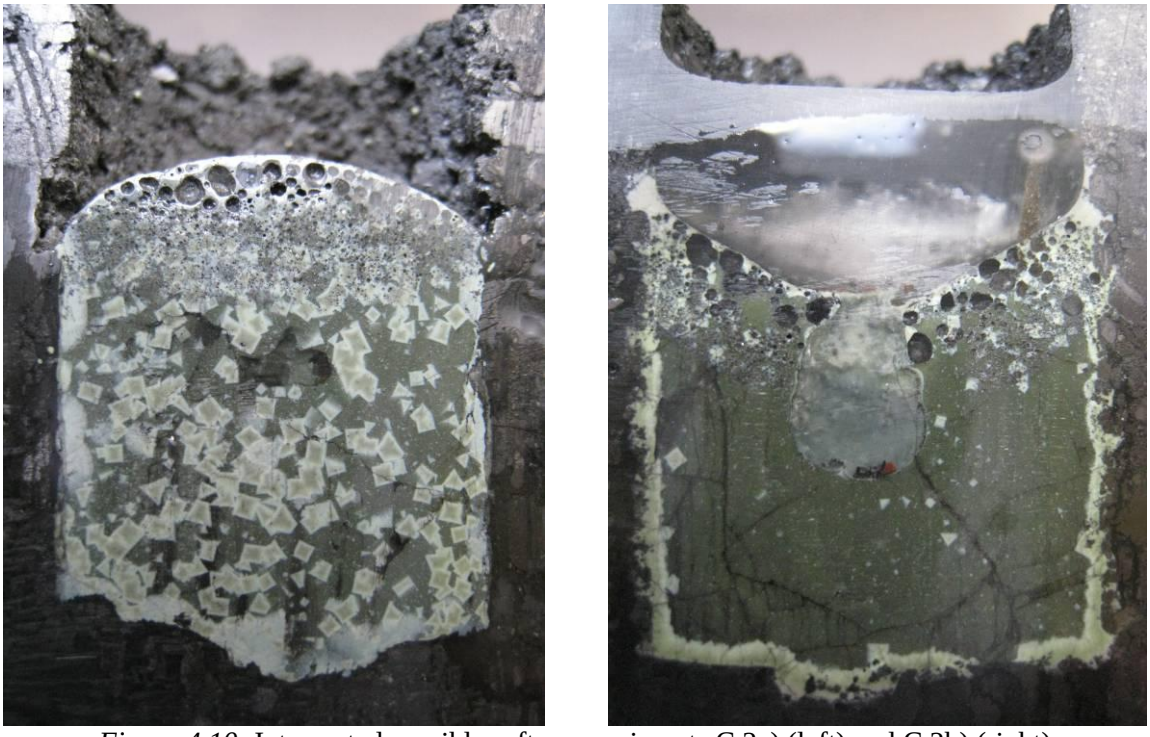

Figure 4.10: Intersected crucibles after experiments C.2a) (left) and C.2b) (right)

After two hours at 1367°C, Figure 4.10 - left, only a small degree of interaction between slag and refractory can be observed. The slag appears to have non-wetting properties with respect to the ramming paste, and crystalline areas were formed within the slag during cooling. Slag was observed to have penetrated into crevices in the refractory after four hours at 1464°C, Figure 4.10 - right, disintegrating the refractory and leaving pieces of refractory embedded in slag. At 1464°C, the slag wetted the ramming paste, and a crystalline slag layer was formed close to the crucible walls. Refractory disintegration was observed microscopically over the entire slag-refractory contact area, and seemingly, sample C.2b) contains less metal prills than sample C.1c).

Figure 4.11 visualizes the crystalline – non-crystalline transition close to the cavity bottom in Figure 4.10 - right at increased magnification. The transition is indicated in red, and dendrites can be observed in bottom right areas of the image. Crystalline areas were shown to have an MnO content of 0.6 wt%, while in non-crystalline areas the MnO content was 1.6 wt%. A CaO/SiO_2 ratio of 1.2 was measured in the crystalline slag; a high value compared to a ratio of 0.9 in the non-crystalline areas and 0.7 in fresh SiMn slag II according to Table A.2 in Appendix A.3. In bottom left parts of the Figure 4.11, slag can be observed disintegrating the refractory wall.

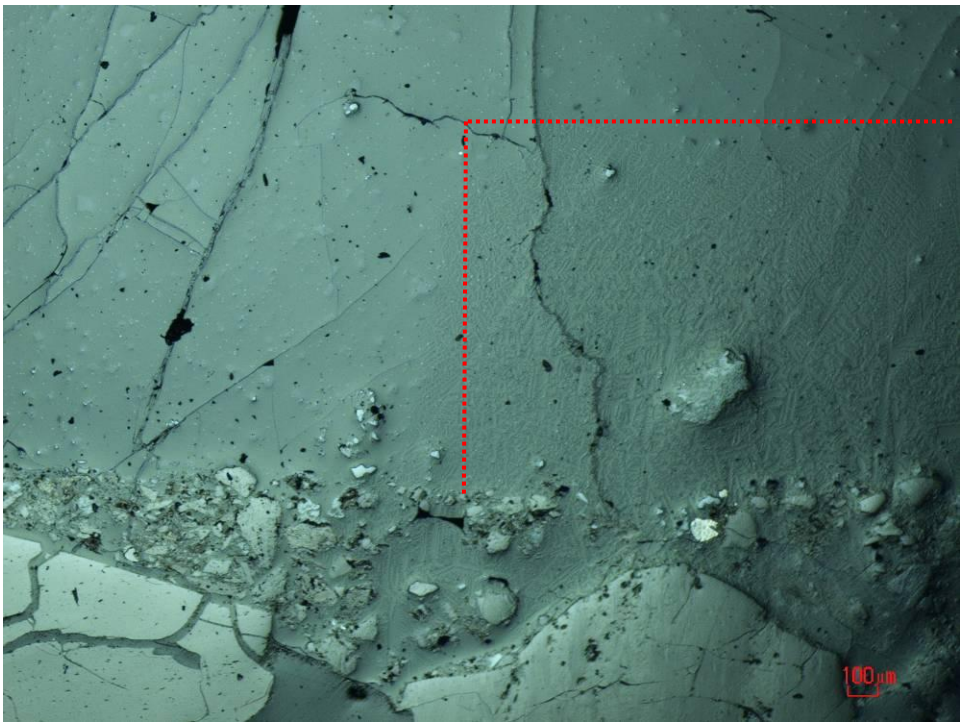

Figure 4.11: Crystalline – non-crystalline transition in sample C.2b) (indicated in red). Scale bar reads 100 µm.

Figure 4.12 shows an area of interaction between slag and refractory close to the lower right corner in Figure 4.10 - right. In left parts of Figure 4.12, a low MnO content corresponding to crystalline areas in Figure 4.11 was measured. In right parts of the image, increased average MnO and MgO contents of 2.9 wt% and 8.9 wt% were measured. Many small, white metal prills(5a) can be observed close to refractory particles(5b), while larger metal prills(5c) can be observed embedded in slag. Both large and small prills have high Fe contents: An average of 28.6 wt% Fe was measured in large prills, and up to 42 wt% Fe was measured in small prills. Light grey SiC areas(5d) can also be observed.

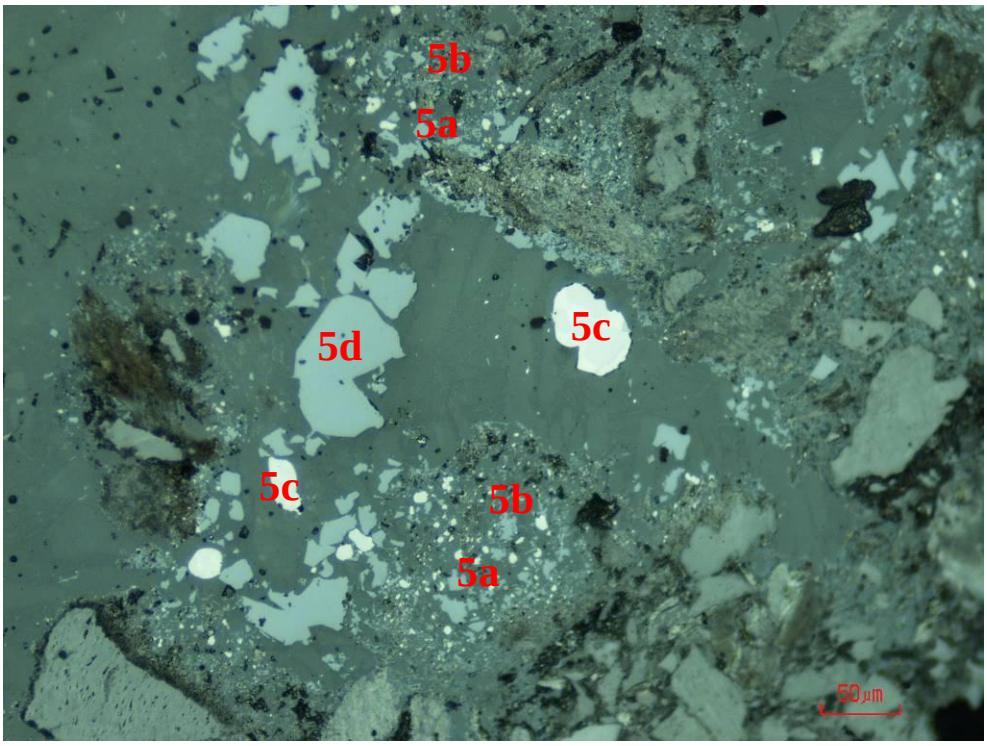

Figure 4.12: Slag-refractory interaction during experiment C.2b). Scale bar reads 50 µm.

Figure 4.13 visualizes the change in cavity diameter during experiment C.2b):

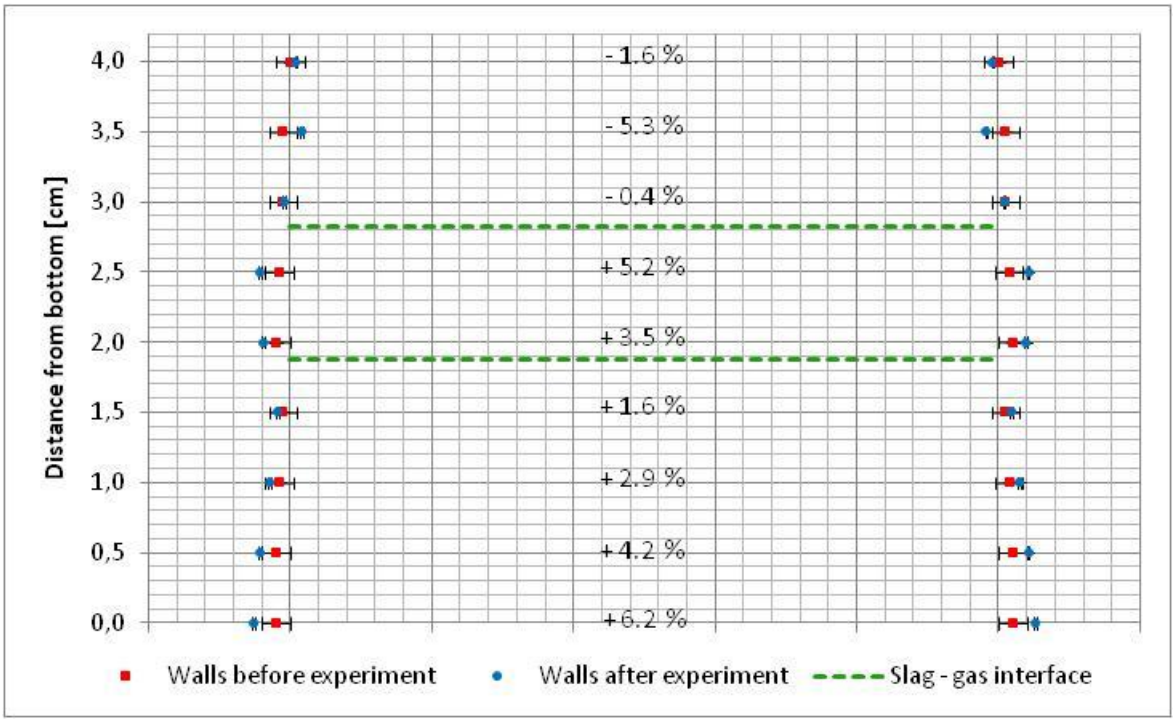

Figure 4.13: Wear profile experiment C.2b)

Comparing Figures 4.7 and 4.13; SiMn slag II appears to have caused a lower degree of macroscopic ramming paste wear than SiMn slag I, and increased wear at the slag-gas interface can only be concluded for wear caused by SiMn slag I.

4.1.3 Silicon carbide tap block VS SiMn slag I

Figure 4.14 shows the intersected crucible after experiment C.3:

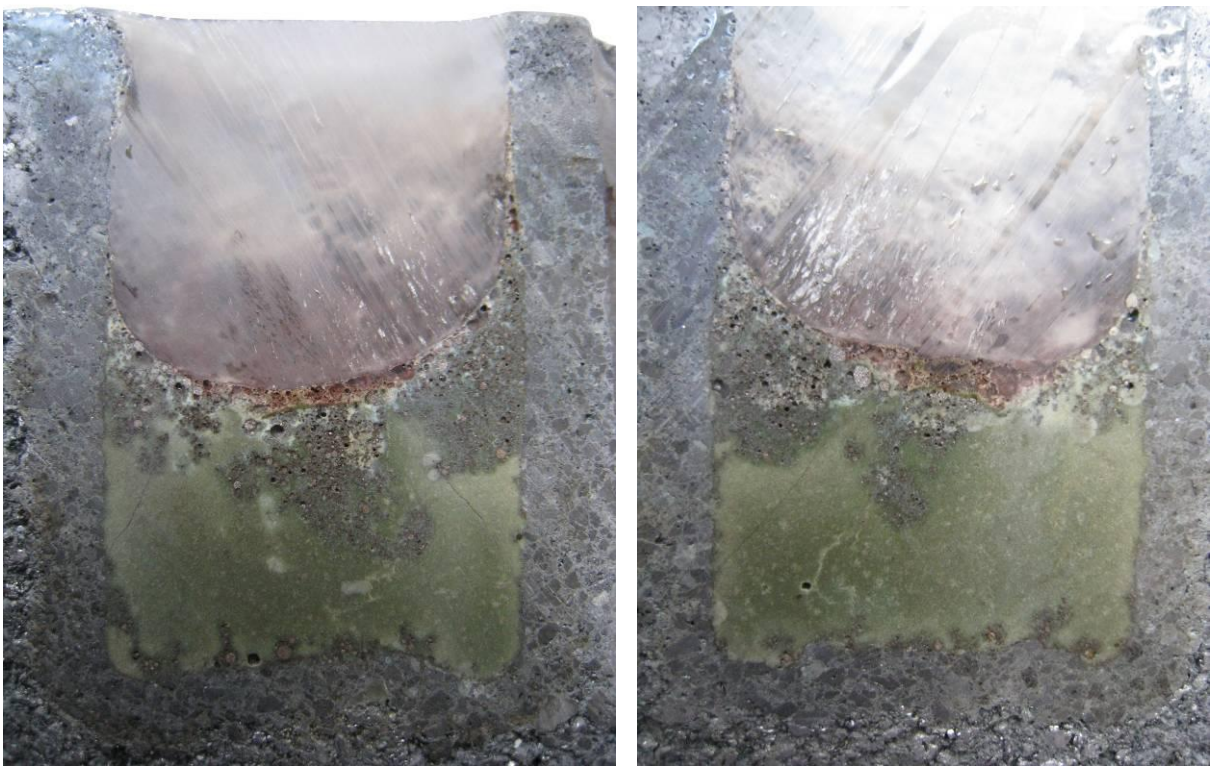

Figure 4.14: Intersected crucible after experiment C.3

No penetration was observed macroscopically, so large scale refractory wear was considered negligible, confirmed by the wear profile in Figure 4.15. A large degree of wetting was observed as slag crept relatively high up the cavity walls. Large concentrations of gas bubbles were formed at the slag-gas interface. Metal prills originally present in the slag were observed on the bottom of the cavity and at the slag-gas interface, while a higher Fe content was measured in metal prills found as a part of the slag wetting the cavity walls.

Figure 4.15 visualizes the change in cavity diameter during experiment C.3. It can be observed that the change in cavity diameter was within the uncertainty of the diameter measurements before the experiment, so large scale refractory wear cannot be proven.

Microscopically, the slag was observed to interact with the refractory, visualized in the optical microscope image in Figure 4.16. Slag(6a) penetrated into the porous SiC crucible walls, dissolving the refractory matrix and interacting with and disintegrating larger particles(6b). Many small, white metal prills(6c) with an average Fe content of 65.5 wt% were observed within the refractory. In correspondence with Table A.11 in Appendix A.6, an MnO content of 1.0 wt% was measured in slag found inside refractory wall compared to the bulk content of 4.4 wt%. Figure 4.17 visualizes measured MnO gradients in slag from bulk to within SiC wall after experiments C.3 and C.4. Decreasing MnO contents indicate MnO reduction.

Figure 4.18 shows slag with decreased Al_2O_3 and CaO contents compared to bulk slag wetting the refractory close to the slag-gas interface. In accordance with Table A.13 in Appendix A.6, large metal prills(7a) with on average 25.2 wt% Fe was observed in the slag, as well as gas pores(7b) both in slag and refractory, possibly indicating gas formation as a

result of slag penetration. In this area, small metal prills(7c) with a 31.0 wt% average Fe-content were observed within the refractory. Close to the slag-refractory interface, slag contained increased concentrations of SiO_2.

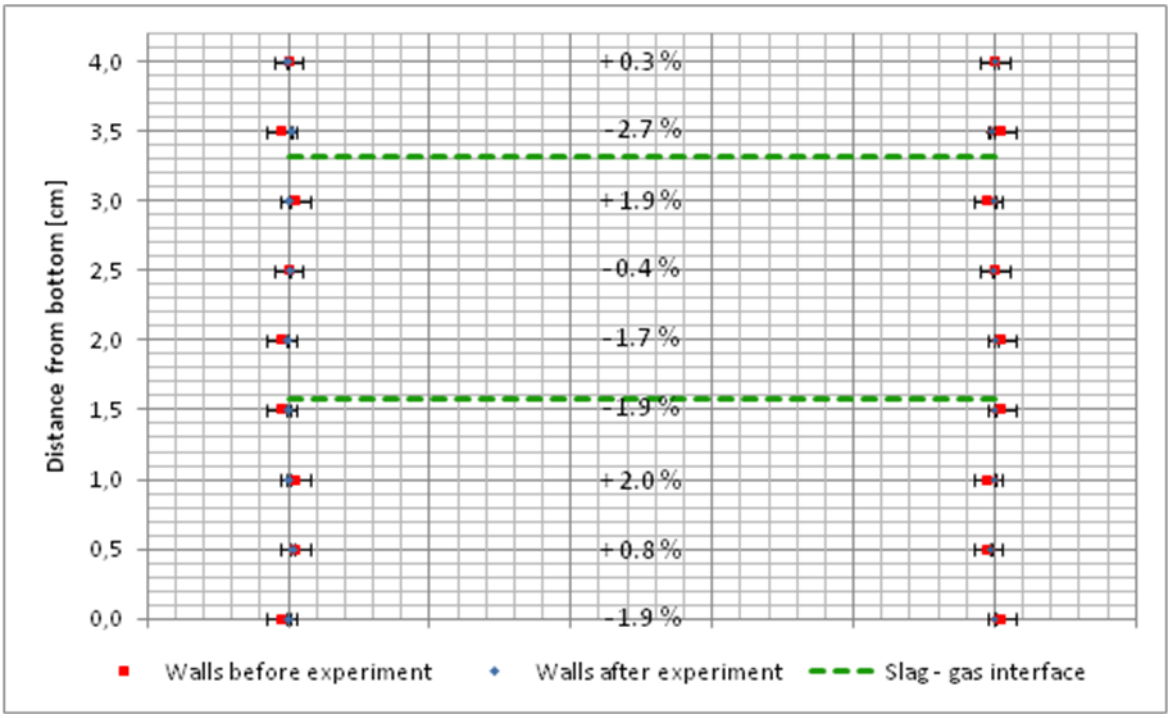

Figure 4.15: Wear profile experiment C.3

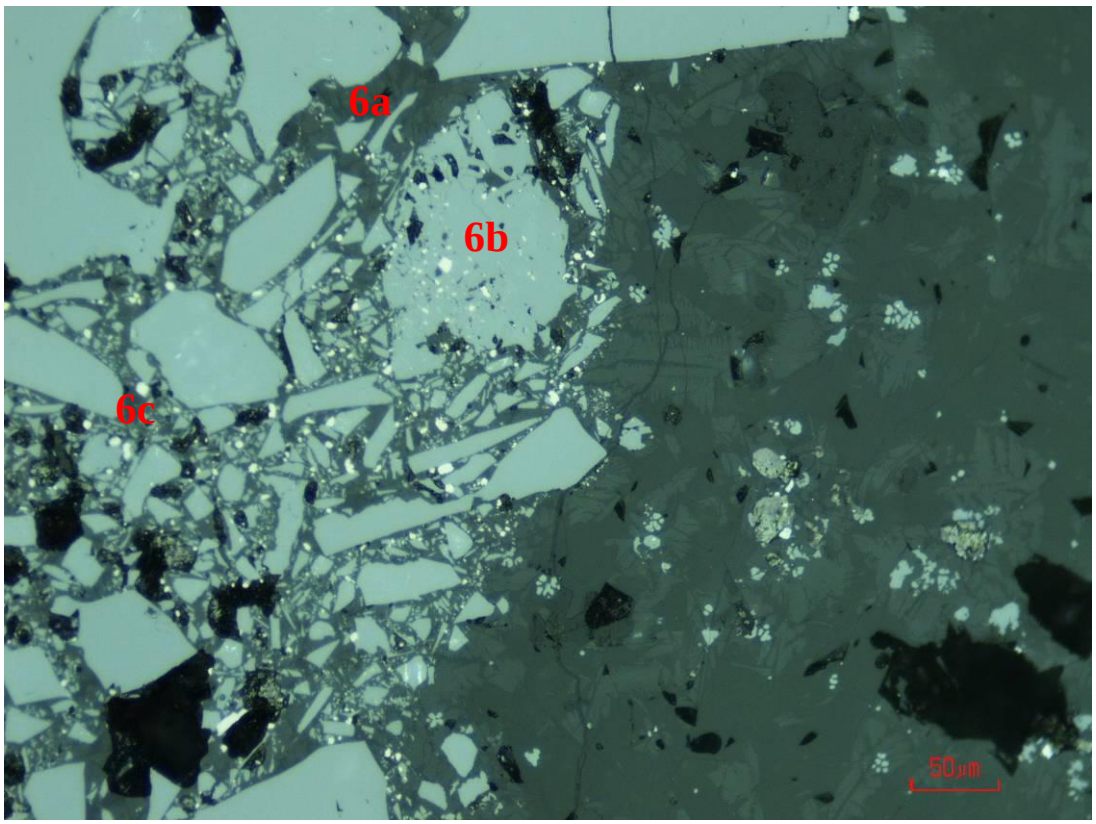

Figure 4.16: Slag-refractory interface after experiment C.3. Scale bar reads 50 µm.

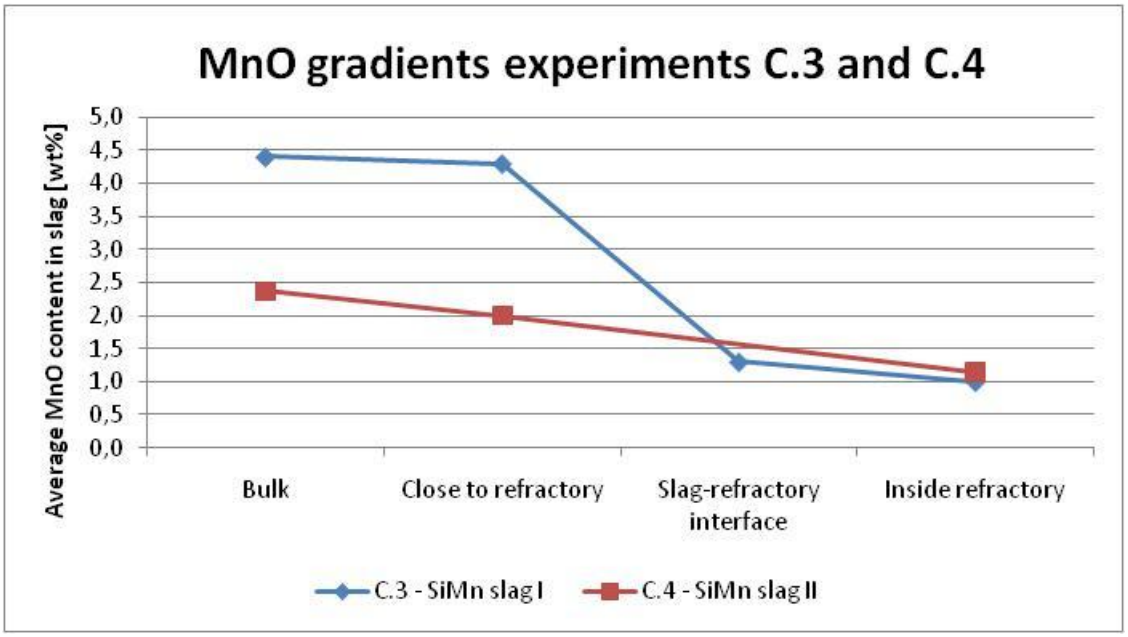

Figure 4.17: MnO gradient from slag bulk to inside SiC wall after experiments C.3 and C.4. Based on data from Table A.11 in Appendix A.6.

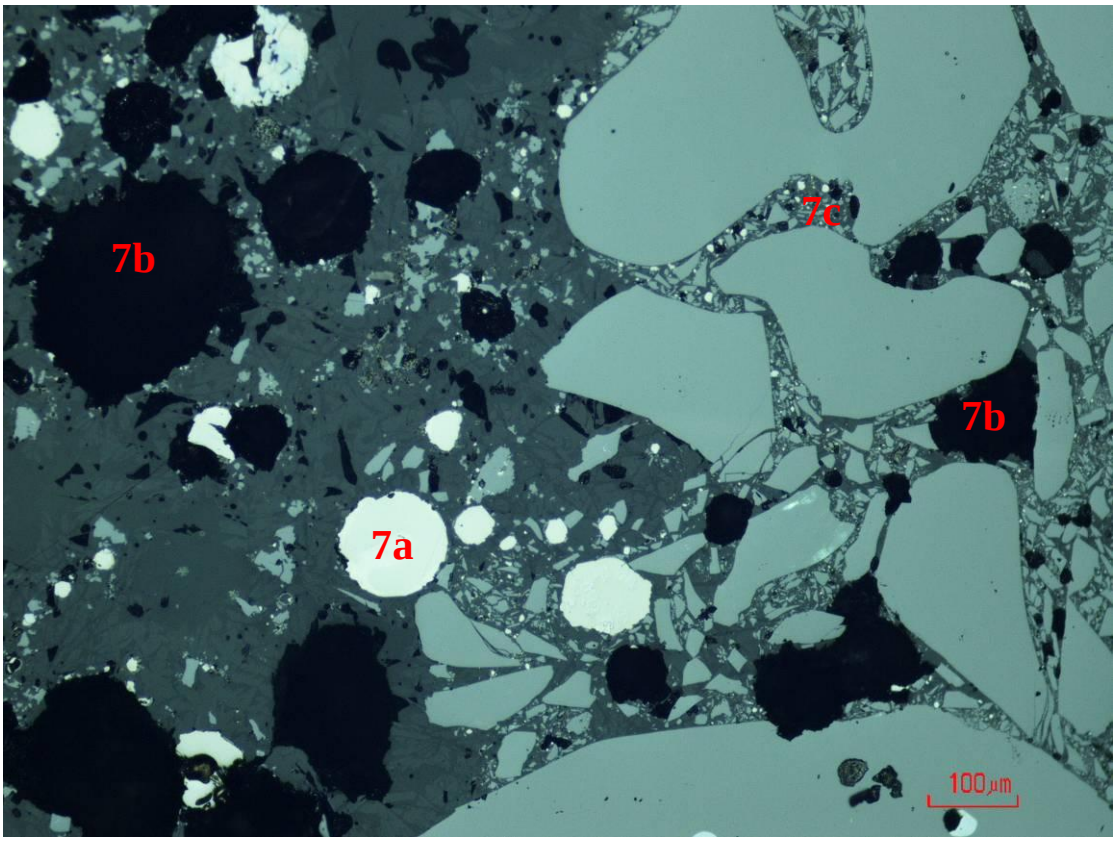

Figure 4.18: Slag wetting and interacting with SiC crucible wall after experiment C.3 Scale bar reads 100 µm.

4.1.4 Silicon carbide tap block VS SiMn slag II

Figure 4.19 shows the intersected crucible after experiment C.4. No penetration was observed macroscopically, and the wear profile in Figure 4.20 confirms that no large scale refractory wear can be proven. The molten slag cooled uniformly, as no difference in crystallinity can be

observed. A large degree of wetting was observed, and gas bubbles and metal prills were found high up on the cavity wall.

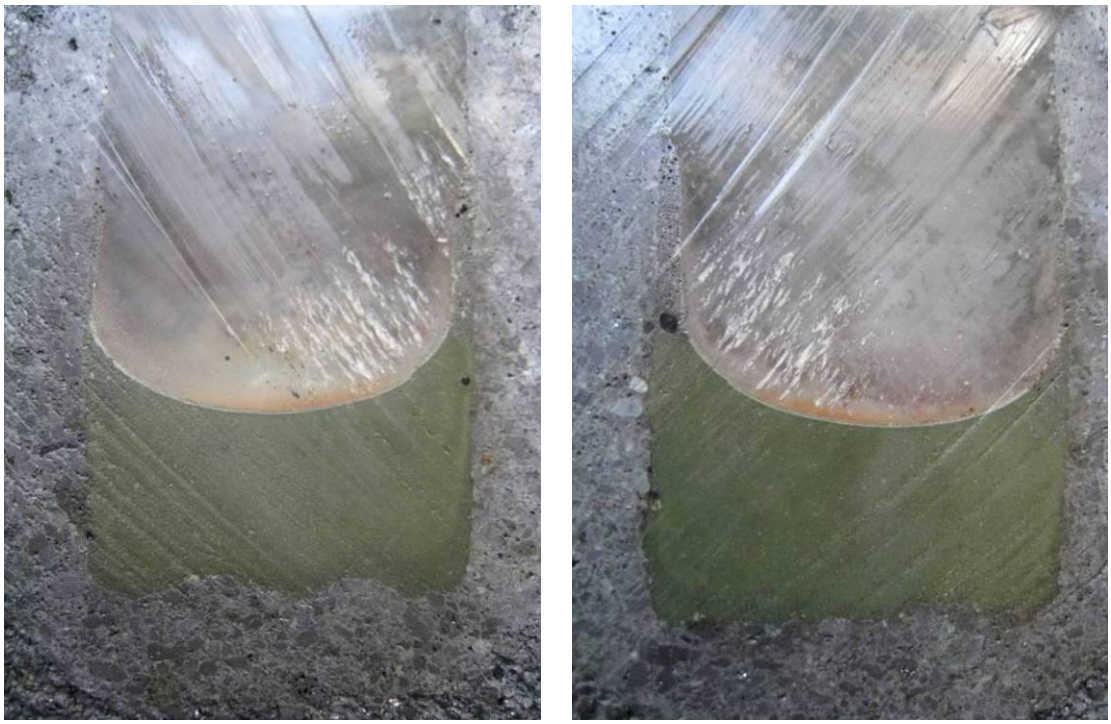

Figure 4.19: Intersected crucible after experiment C.4

Figure 4.20 visualizes the change in cavity diameter during experiment C.4. It can be observed that the change in cavity diameter was generally within the uncertainty of the diameter measurements.

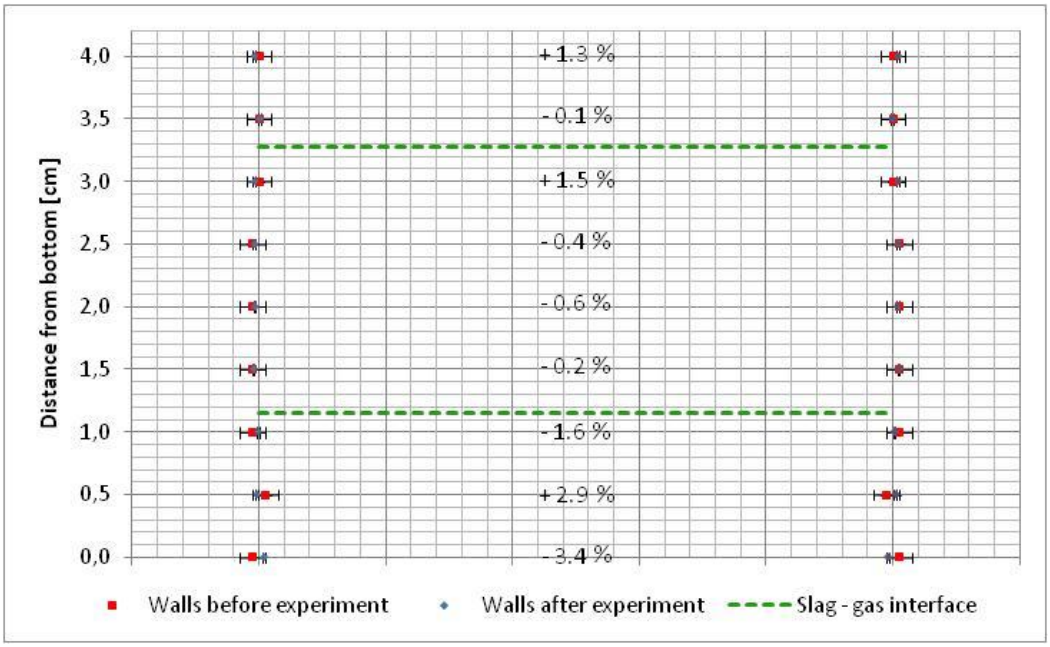

Figure 4.20: Wear profile experiment C.4

Microscopically, interaction between slag and refractory was observed, especially close to the slag-atmosphere interface where the slag wetted the cavity wall. Figure 4.21 shows interaction in lower areas of the cavity, and relatively large metal prills(8a) with average composition

18.4 wt% Si, 40.1 wt% Mn and 41.4 wt% Fe can be observed inside the SiC wall. An even higher Fe content was measured in smaller prills, presented in Table A.14 in Appendix A.6. Average MnO content in bulk slag was quantified to 2.4 wt%, and MnO contents as low as 0.7 wt% were measured in slag found inside refractory wall. MnO gradient in slag after experiment C.4 is visualized in Figure 4.17 in Chapter 4.1.3.

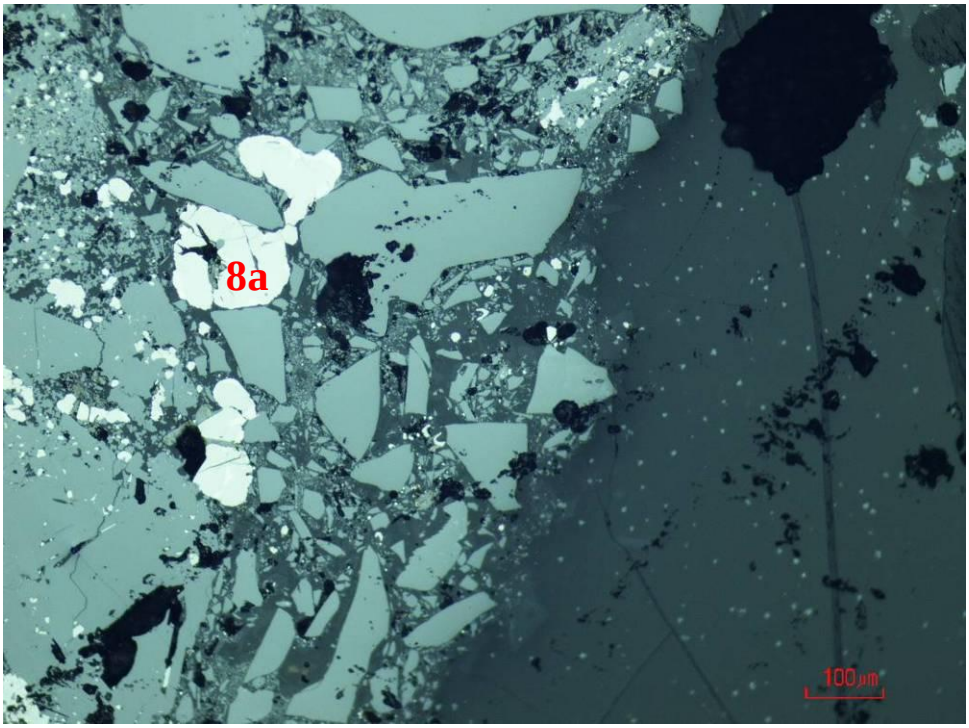

Figure 4.21: Slag - refractory interaction after experiment C.4. Scale bar reads 100 µm.

Figure 4.22 shows a large refractory particle(9a) disintegrated during experiment C.4. Gas pores were observed both in refractory and slag.

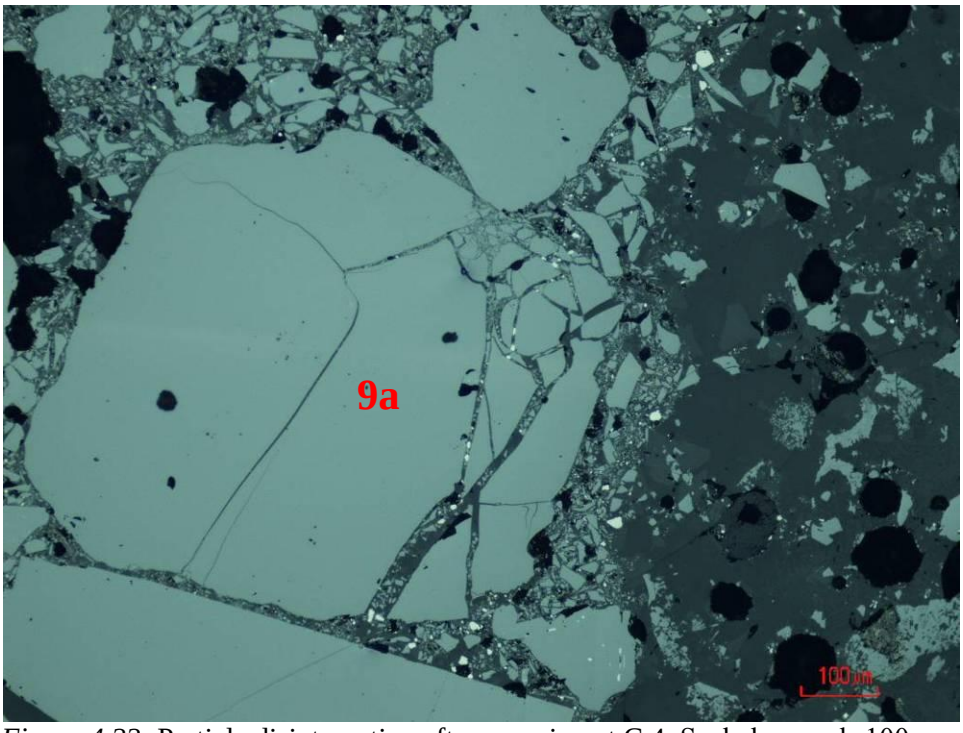

Figure 4.22: Particle disintegration after experiment C.4. Scale bar reads 100 µm.

Figure 4.23 shows slag(10a) and metal(10b & 10c) phases found inside a SiC particle(10d). An SiO_2 content of 52.6 wt% was measured in the slag phase containing negligible amounts of MnO. The bulk metal phase(10b) was relatively pure Si, while smaller metal prills(10c) contained Si and Mn in a 40 – 60 weight ratio.

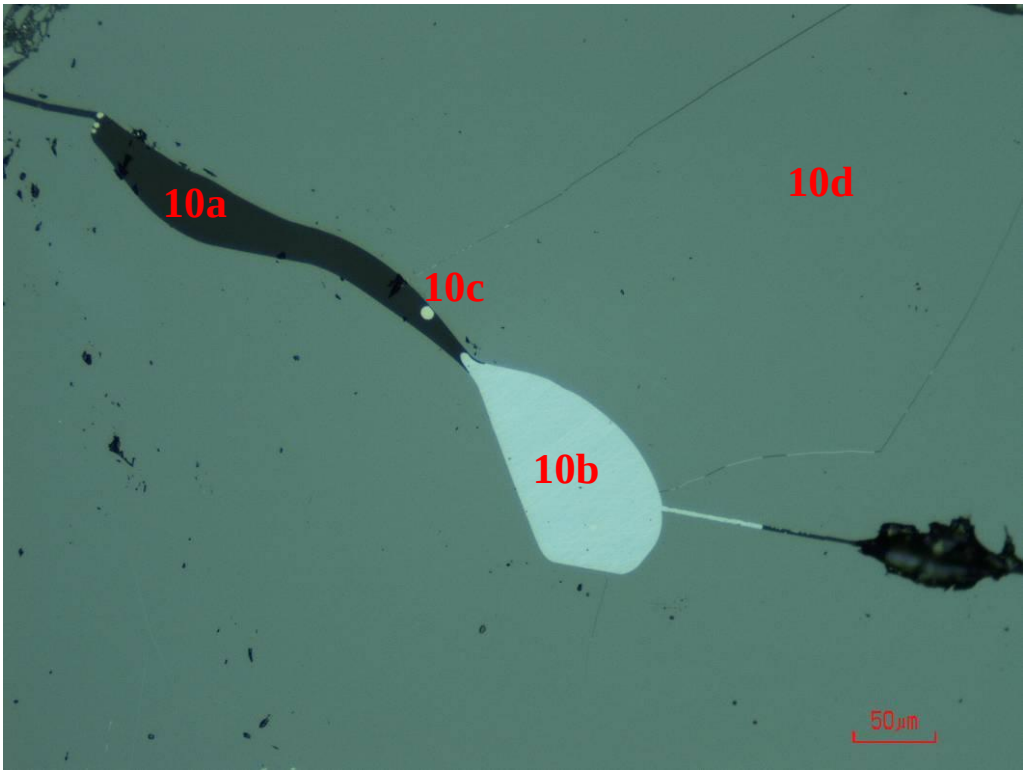

Figure 4.23: Slag and metal inside SiC particle after experiment C.4. Scale bar reads 50 µm.

4.1.5 Carbon tap block VS SiMn slag I

Figure 4.24 shows the intersected crucible after experiment C.5:

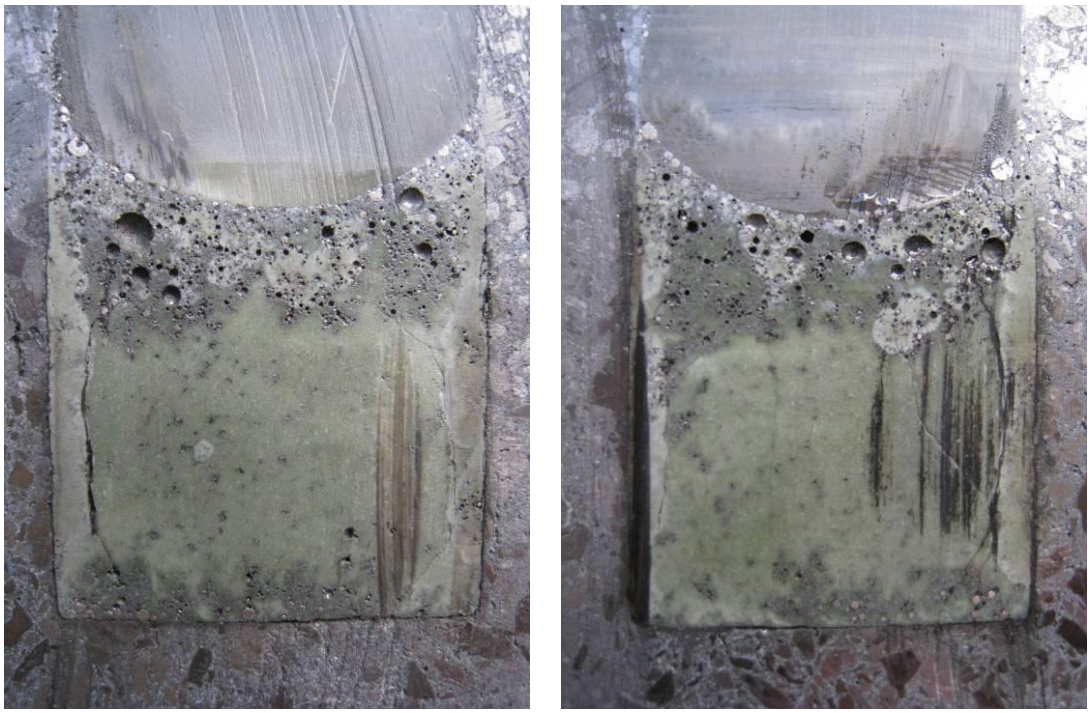

Figure 4.24: Intersected crucible after experiment C.5

No macroscopic wear was observed after experiment C.5, as confirmed by the wear profile in Figure 4.25. Metal prills were observed close to the slag-gas interface, close to the cavity bottom, and as a part of the slag wetting the cavity walls. Gas bubbles were observed at the slag-gas interface and close to the cavity bottom.

Figure 4.25 visualizes the change in cavity diameter during experiment C.5. It can be observed that the change in cavity diameter was within the uncertainty of the diameter measurements.

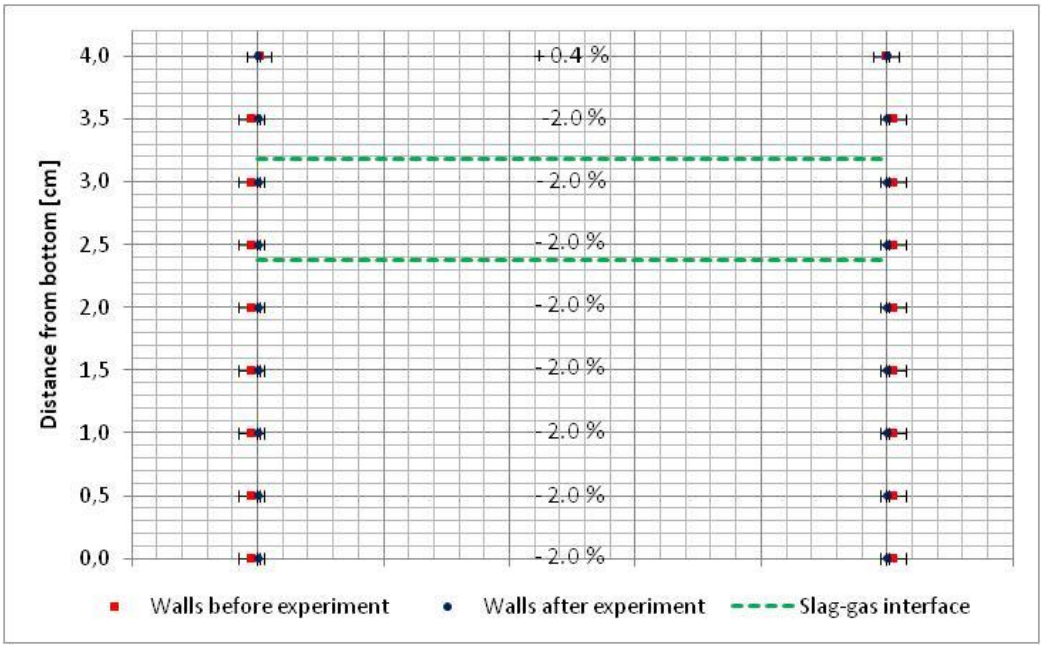

Figure 4.25: Wear profile experiment C.5

Figure 4.26 shows the refractory-slag interface at increased magnification:

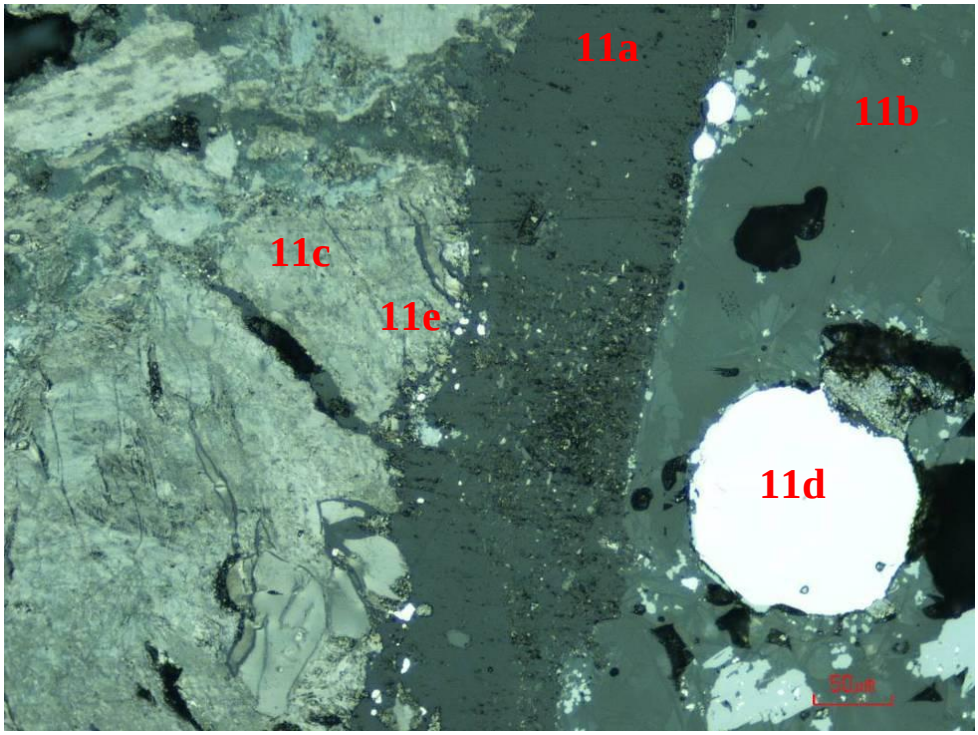

Figure 4.26: Slag-refractory interface after experiment C.5. Scale bar reads 50 µm.

A ~250 μm layer of epoxy(11a) separates the slag(11b) from the refractory(11c) in most of the interface area, as slag contracted during cooling. In accordance with Table A.13 in Appendix A.6, a large, white metal prill(11d) with composition similar to SiMn metal I can be observed embedded in the slag, while smaller metal prills(11e) with increased Mn content can be observed on the refractory side. Metal prills on, and to a small extent in, the refractory material were the only evidence of possible slag-refractory interaction in this system. Pores were observed inside refractory material after cutting, but these were believed to exist naturally in material.

Figure 4.27 visualizes white metal prills inside the refractory material:

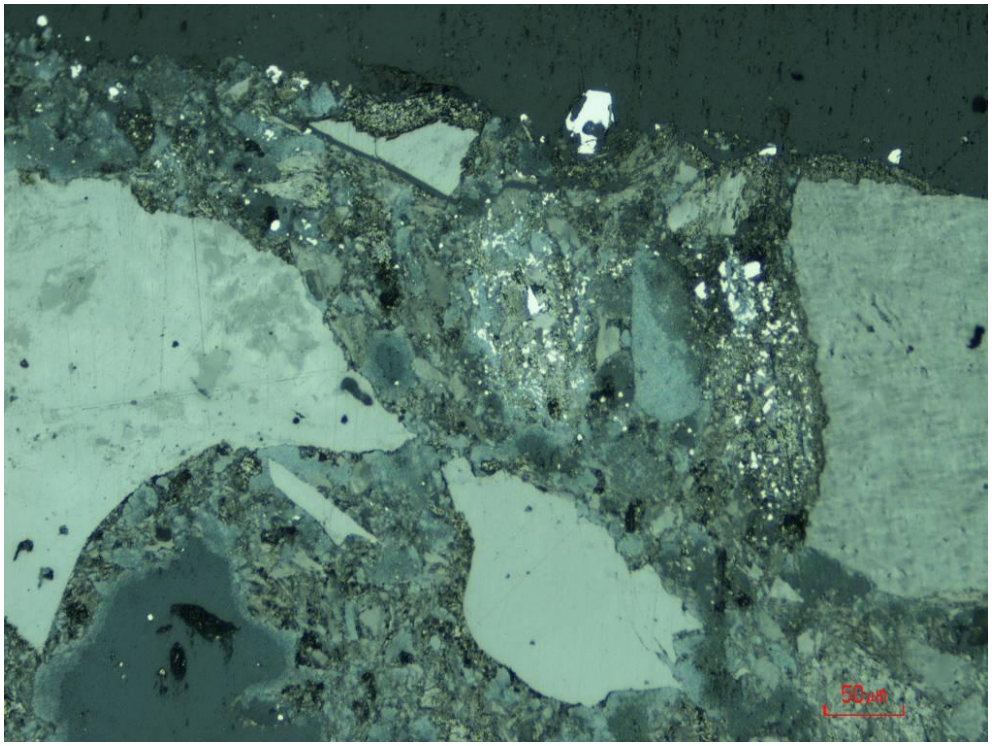

Figure 4.27: White metal prills inside refractory after experiment C.5. Scale bar reads 50 μm.

4.1.6 Carbon tap block VS SiMn slag II

Figure 4.28 shows the intersected crucible after experiment C.6. No macroscopic wear was observed, as confirmed by the wear profile in Figure 4.29. Gas bubbles and scattered metal prills were observed close to the slag-gas interface, and slag wetted the cavity walls. Crystalline areas were observed in the slag bulk.

Figure 4.29 visualizes the change in cavity diameter during experiment C.6. It can be observed that the change in cavity diameter generally was within the uncertainty of the diameter measurements.

Optical microscopy showed that the slag contracted upon cooling. No contact between C-refractory and slag was observed at the bottom of the crucible cavity, visualized in Figure 4.30. A few C particles(12a) followed the contracting slag, but minimal interaction was observed.

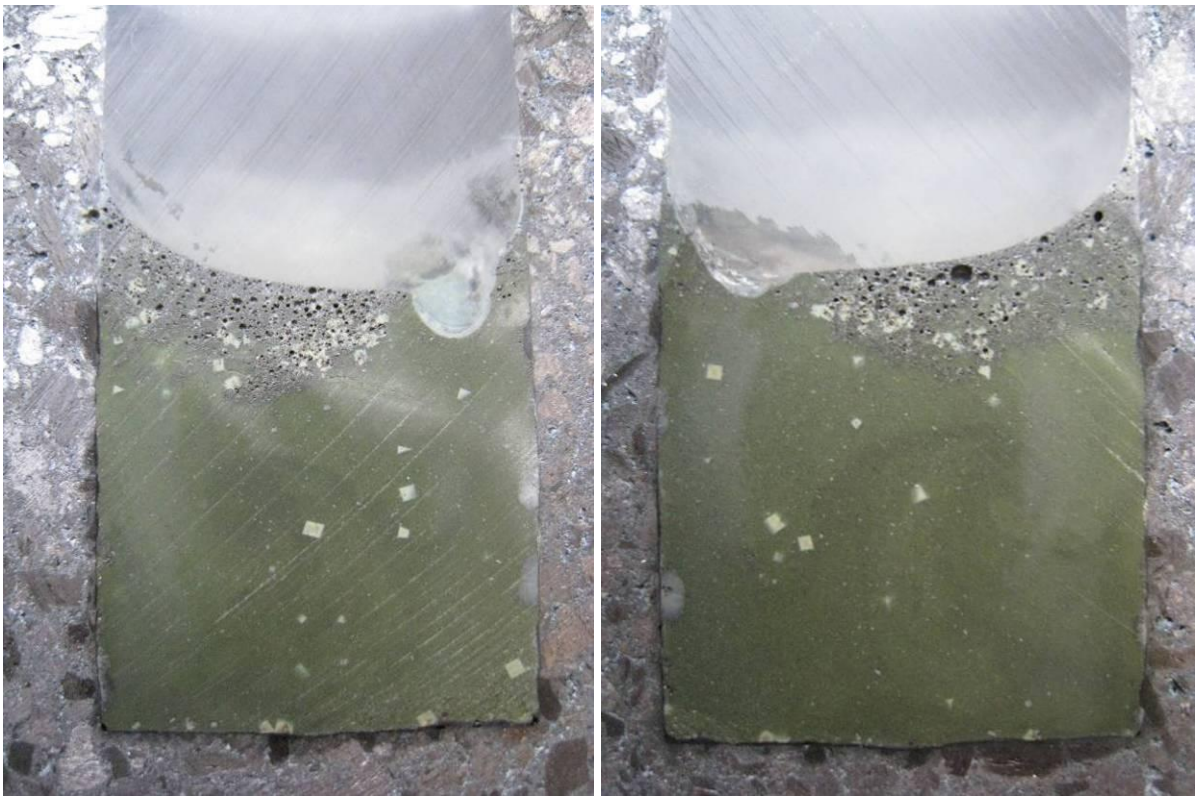

Figure 4.28: Intersected crucible after experiment C.6

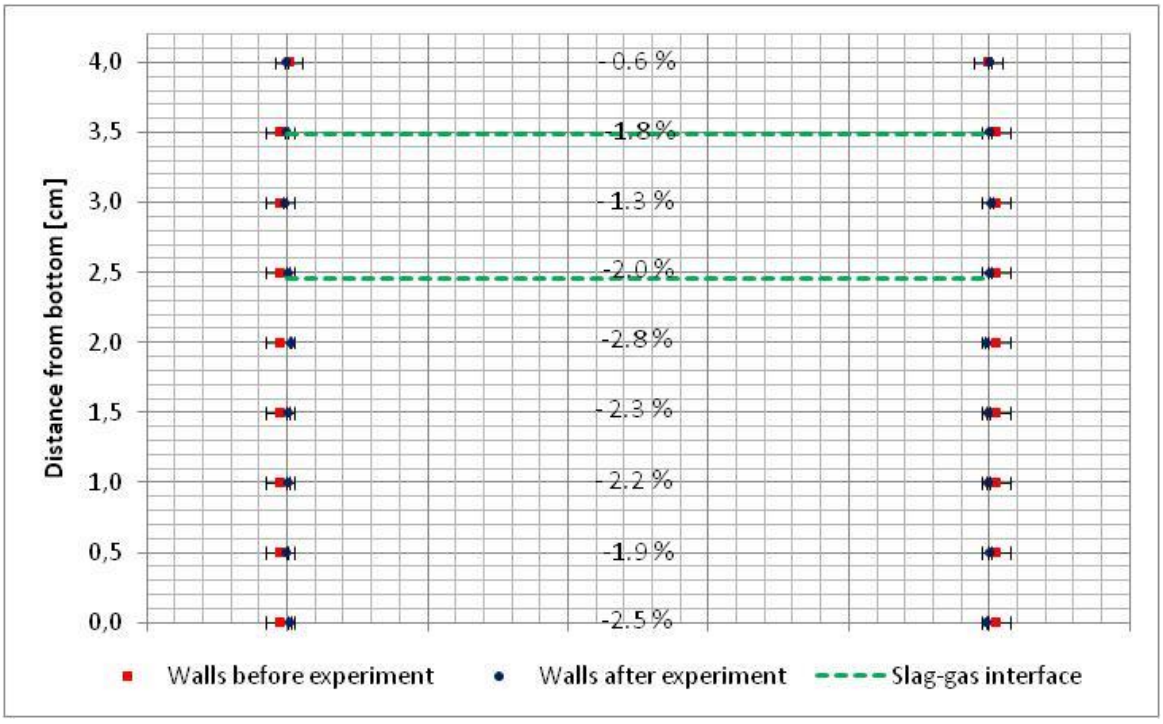

Figure 4.29: Wear profile experiment C.6

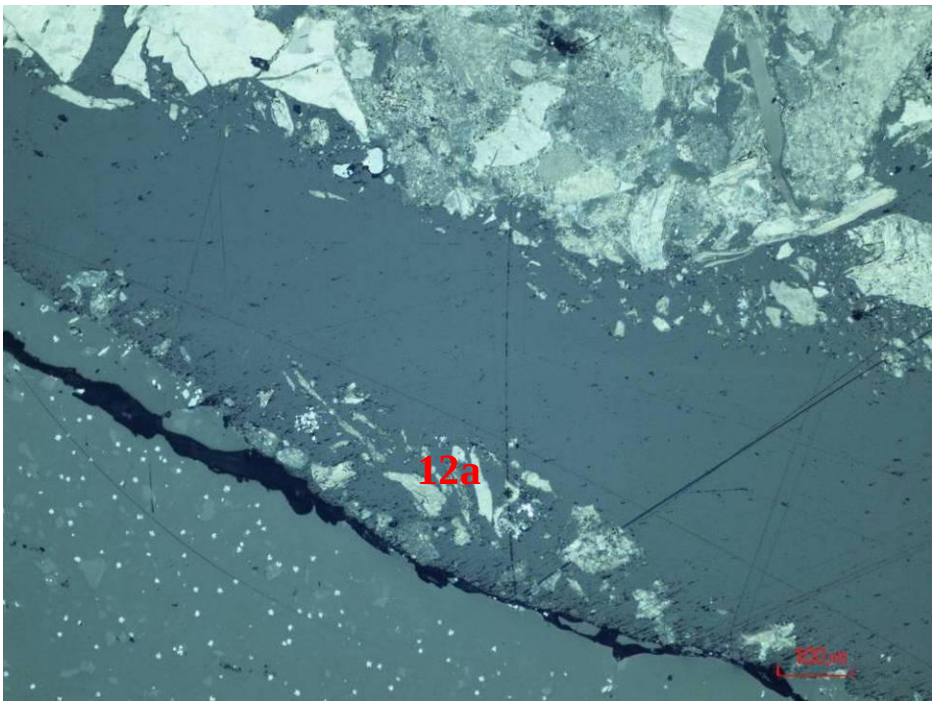

Figure 4.30: Noncontact slag-refractory interface after experiment C.6. Scale bar reads 100 μm.

Figure 4.31 shows the slag-refractory interface close to the slag-gas interface. In correspondence with Table A.14 in Appendix A.6, some metal prills(13a) with slightly increased Fe content compared to SiMn metal I were found on the refractory side of the interface, but very little interaction was generally observed – possibly less than after experiment C.5. Table A.9 in Appendix A.6 shows that no major change in bulk slag MnO content can be concluded.

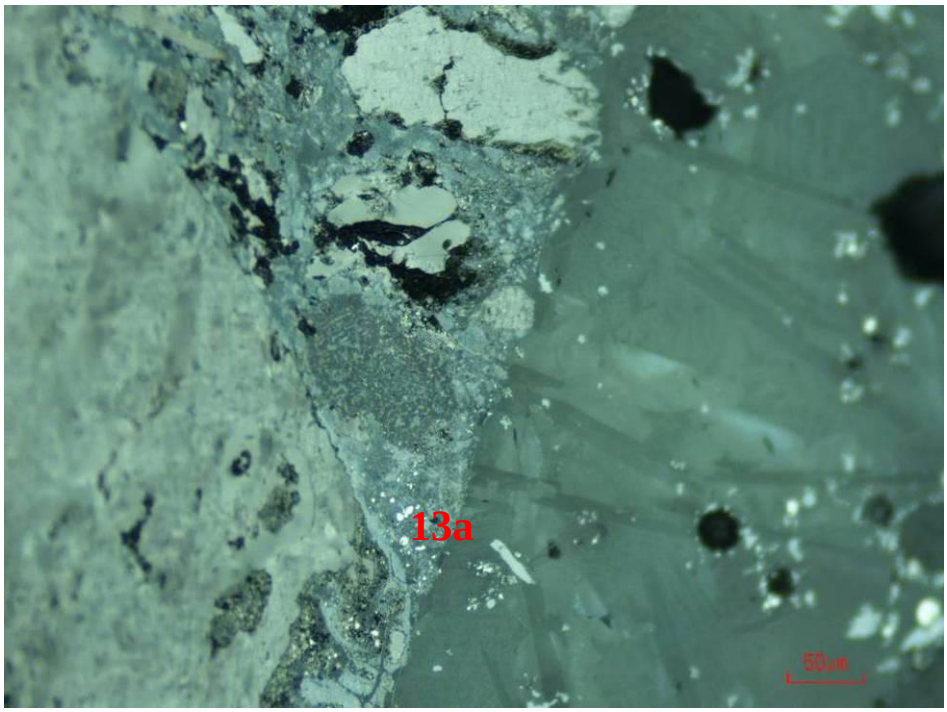

Figure 4.31: Slag – refractory interface after experiment C.6. Scale bar reads 50 μm.

Figure 4.32 shows metal(14a) and SiC(14b) phases embedded in C-refractory(14c). The metal phases contain on average 17.6 wt% Si, 55.1 wt% Mn and 27.1 wt% Fe.

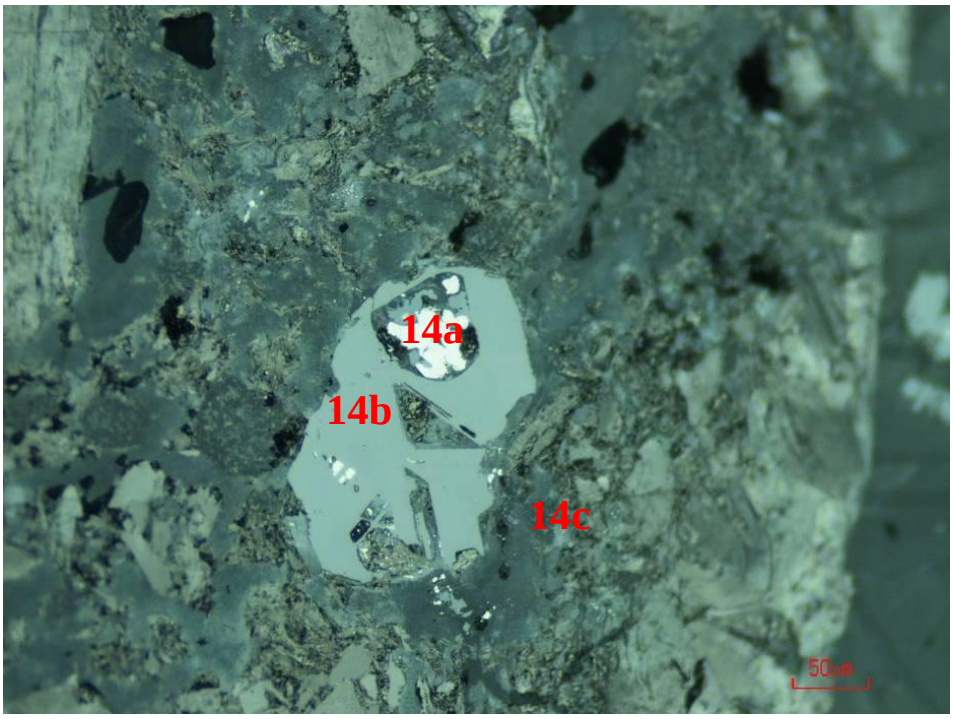

Figure 4.32: Metal and SiC embedded in refractory material after experiment C.6. Scale bar reads 50 µm.

4.1.7 Tap hole clay VS SiMn slag I

Figure 4.33 shows the intersected crucible after experiment C.7. No macroscopic slag-refractory interaction was observed, and the wear profile in Figure 4.34 shows cavity shrinkage – especially in areas in contact with slag. Metal pearls with increased Fe content compared to SiMn metal I and gas bubbles were observed in the upper areas of the slag bulk; gas bubbles increasing in size approaching the slag-gas interface. Slag-refractory contact area was minimized through non-wetting properties at the slag-gas interface.

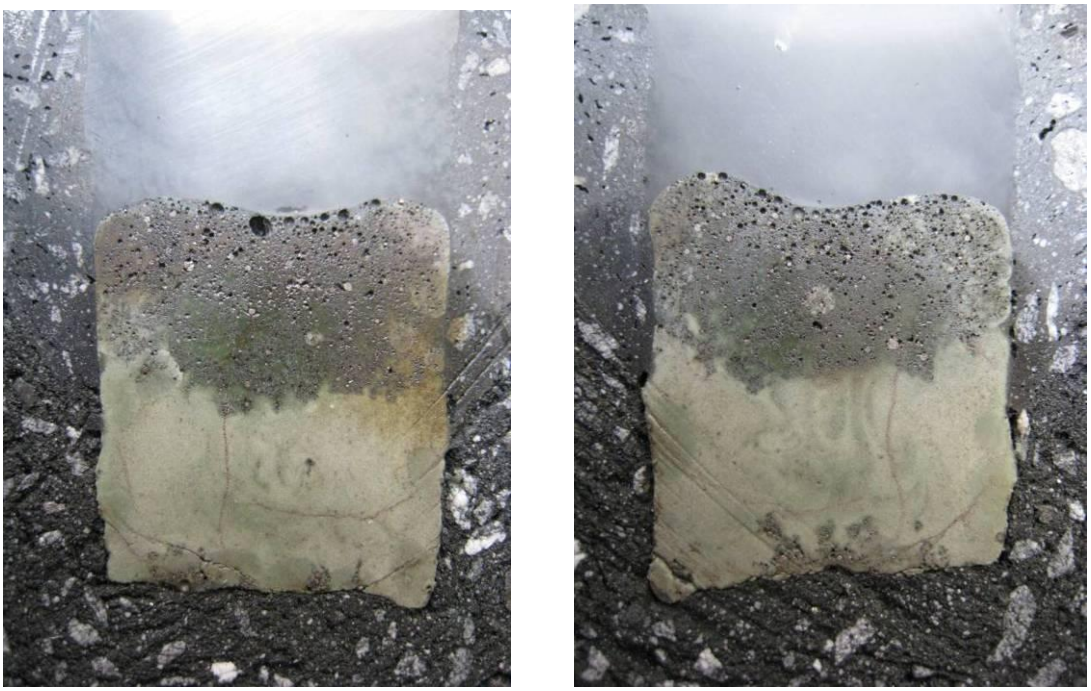
Figure 4.33: Intersected crucible after experiment C.7

Figure 4.34 visualizes the change in cavity diameter during experiment C.7. Significant shrinkage was observed for refractory areas in contact with slag. Above the slag-gas interface, the change in cavity diameter was within the uncertainty of the diameter measurements.

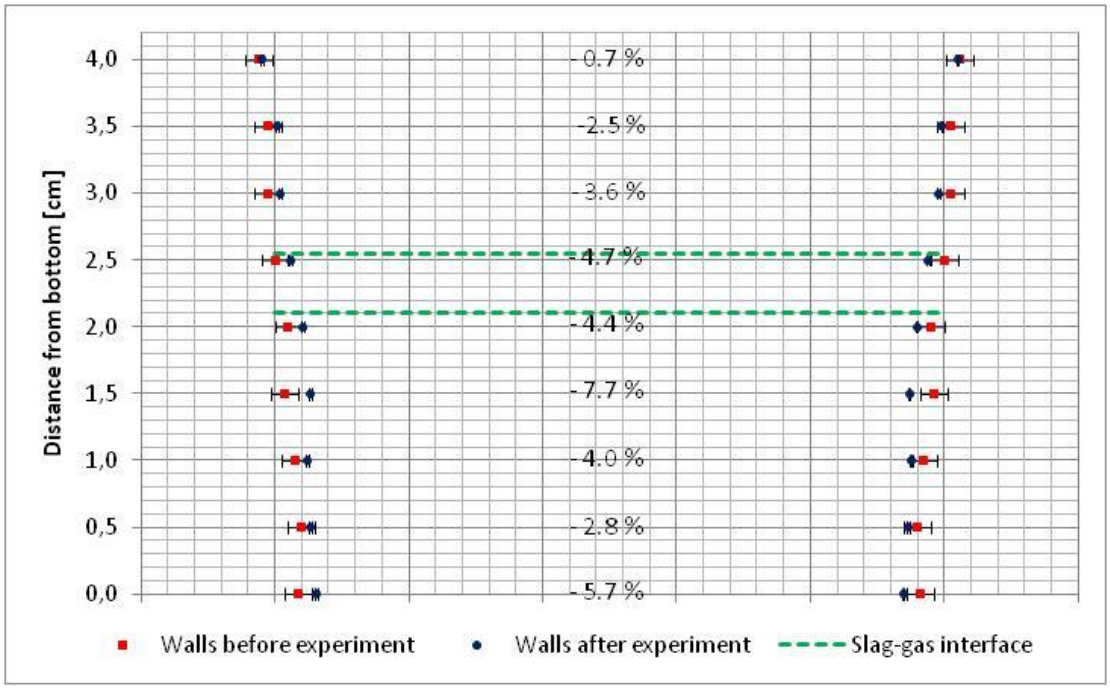

Figure 4.34: Wear profile experiment C.7

The noncontact slag-refractory transition is visualized in Figure 4.35:

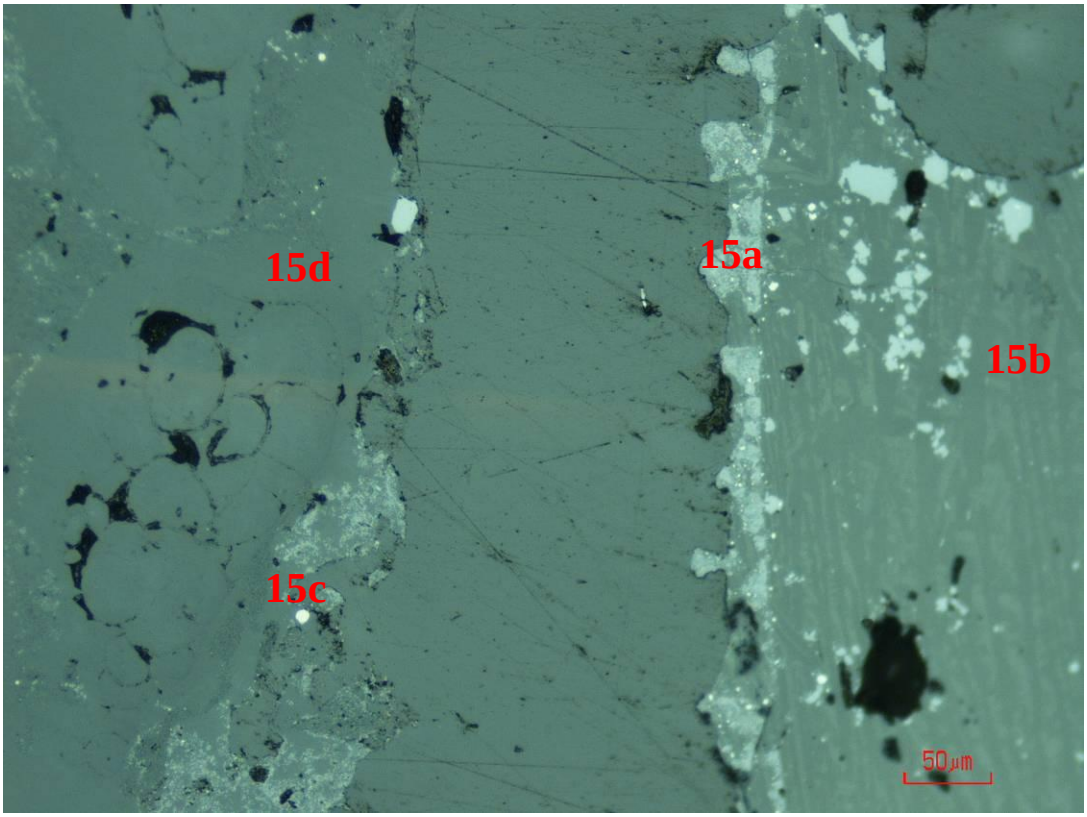

Figure 4.35: Slag-tap hole clay interface after experiment C.7. Scale bar reads 100 µm.

A light grey SiC phase(15a) was observed on the slag side(15b) of the epoxy, and a few white metal prills(15c) with up to 82 wt% Fe was observed inside refractory(15d). According to Tables A.9 and A.10 in Appendix A.6, average slag MnO contents of 0.4 wt% and 5.3 wt% were measured close to the slag-refractory interface and in the bulk slag, respectively, indicating an MnO concentration gradient.

Figure 4.36 visualizes the transition between the light green(16a) and dark green(16b) slag areas in Figure 4.33. In the dark green slag, large gas pores, metal prills, MnS clusters and SiC areas were found embedded in the slag, while in the light green slag, many small gas pores and grain contours indicate that the slag did not melt completely during the experiment.

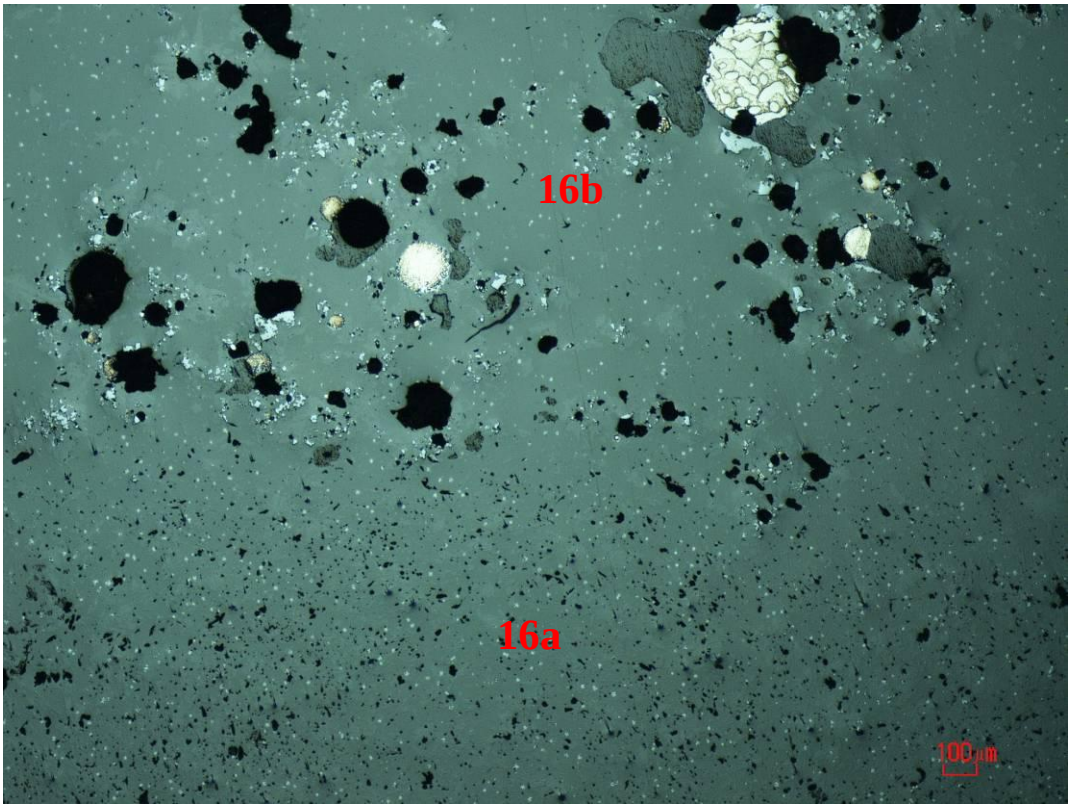

Figure 4.36: Dark green-light green slag transition after experiment C.7. Scale bar reads 100 µm.

4.1.8 Tap hole clay VS SiMn slag II

Figure 4.37 shows the intersected crucible after experiment C.8. Large gas bubbles and metal prills with more than 50 wt% Fe were observed at the slag-gas interface, and one larger gas bubble was observed in the center of the slag bulk. Slag wetted the cavity wall at the slag-gas interface, but slag-refractory contact was minimized below this level. A difference in slag appearance due to gas pore size distribution was observed in bottom parts of the cavity. Grain contours were observed in the light green areas close to the cavity bottom in Figure 4.37, indicating incomplete slag melting during the experiment.

Figure 4.38 visualizes the change in cavity diameter during experiment C.8. Below the slag-gas interface, the diameter change was relatively insignificant, while above the slag level, significant cavity shrinkage was observed.

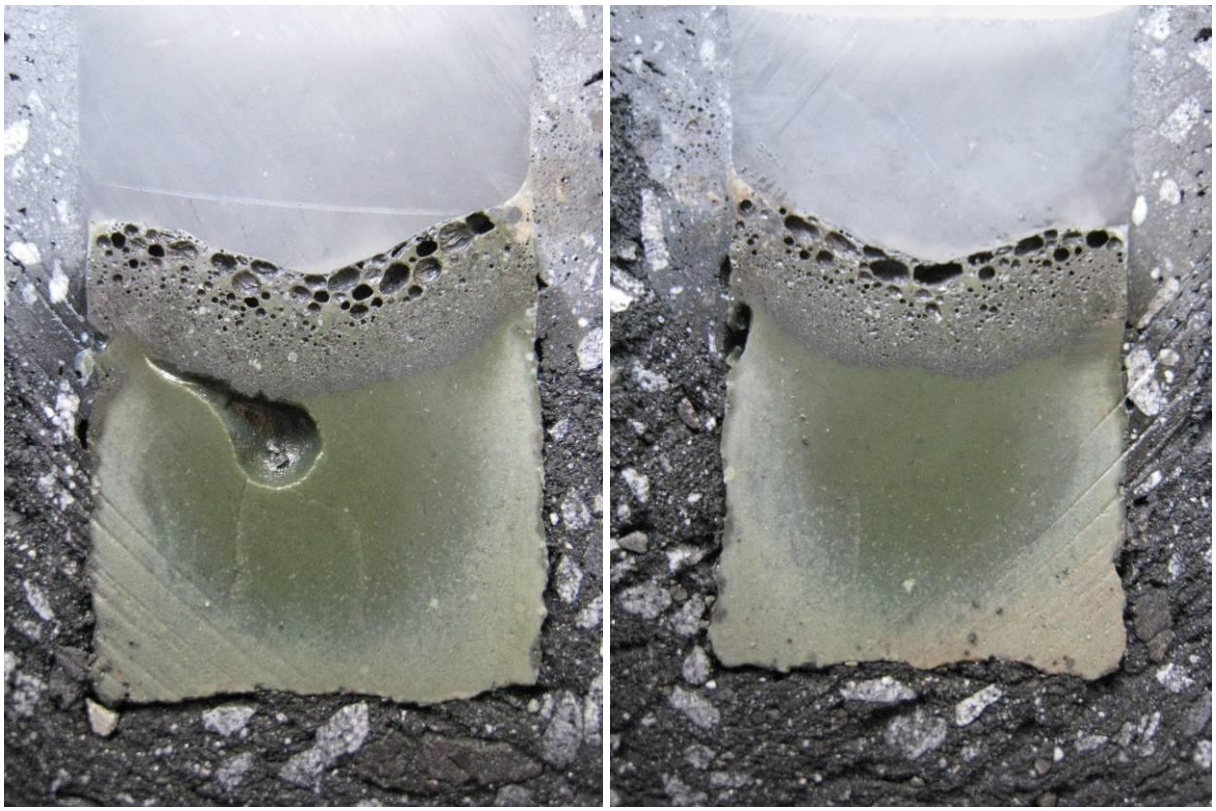

Figure 4.37: Intersected crucible after experiment C.8

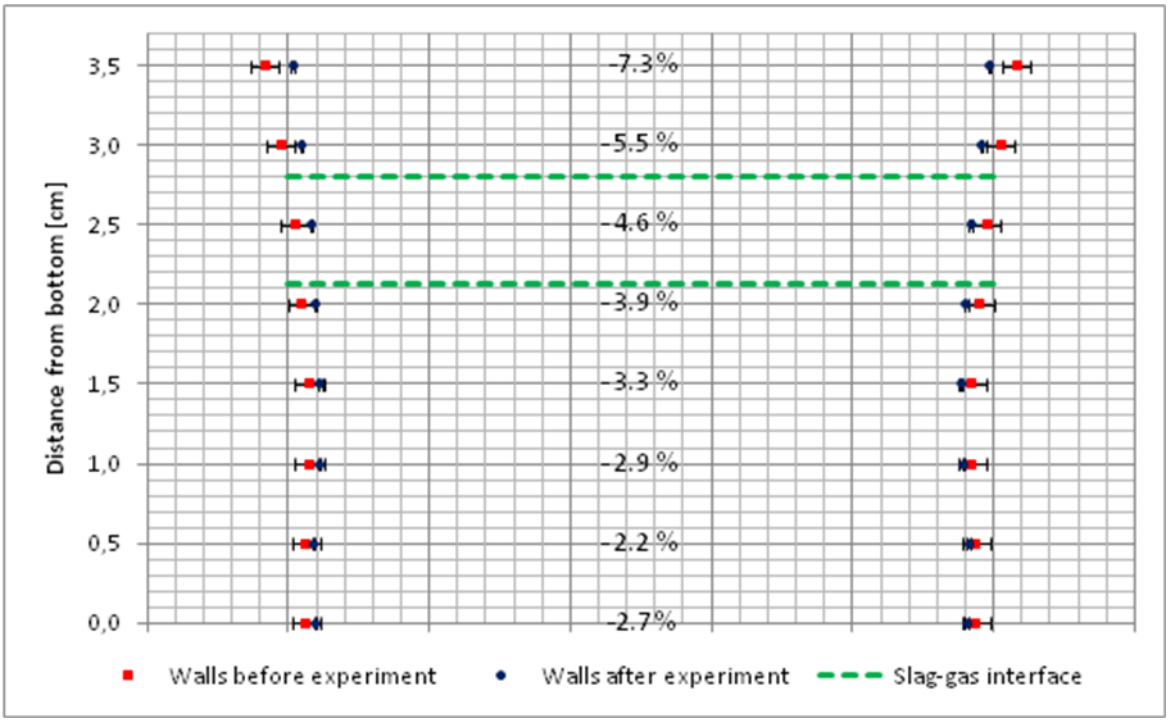

Figure 4.38: Wear profile experiment C.8

Microscopically, a grey SiC layer was observed close to the slag-refractory interface both where the slag(17a) wetted the refractory(17b), visualized in Figure 4.39, and in the non-wetting scheme. A small concentration of metal prills with up to 88 wt% Fe and low Mn content were observed within the refractory. Generally, very little interaction was observed both macroscopically and microscopically after experiment C.8.

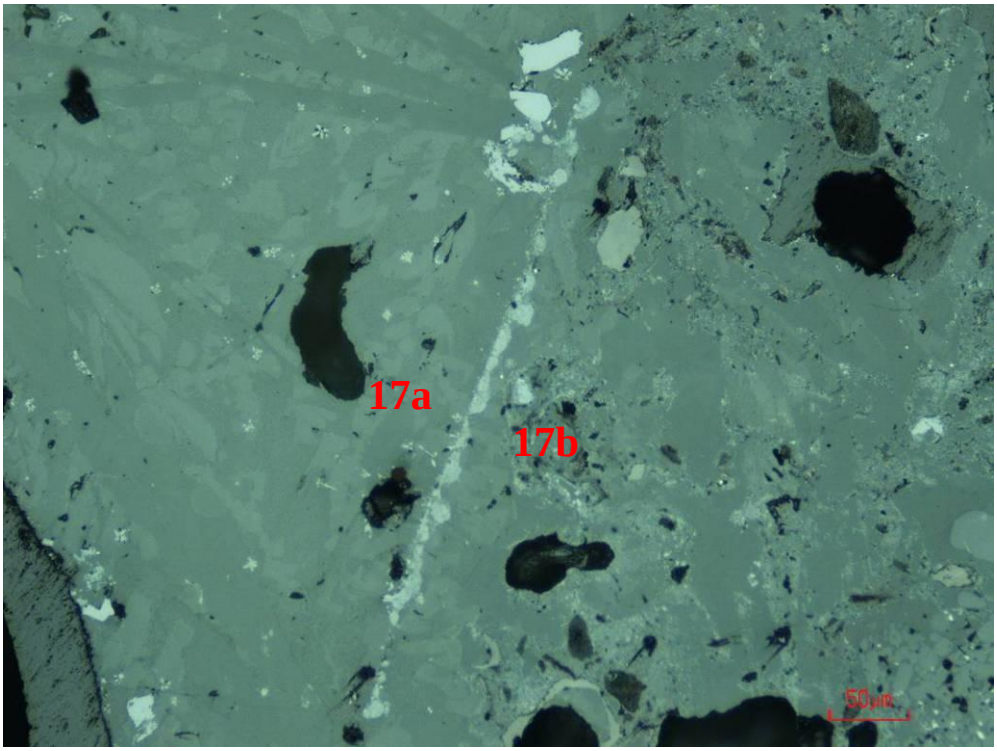

Figure 4.39: SiC layer on the slag-refractory interface after experiment C.8. Scale bar reads 50 μm.

4.2 Static plate tests

Two static plate tests were conducted investigating the interaction between electrode paste and process materials. In this chapter, the results from the different combinations will be presented. Quantitative EDS analyses of slag, metal and SiC compositions are presented in Tables A.9 through A.15 in Appendix A.6.

4.2.1 Electrode paste VS SiMn slag I

Figure 4.40 shows the intersected crucible after experiment P.1a). During the course of the experiment, the electrode plate tilted; finally resting on the graphite crucible wall. Penetration was observed at the slag-gas interface, and the wear profile shown in Figure 4.41 confirms that refractory wear was most extensive in this area. Metal prills and gas bubbles were observed along the length of the submerged part of the electrode plate. The metal prills observed close to the slag-gas interface contained on average 17.3 wt% Si, 76.7 wt% Mn and 5.7 wt % Fe. Closer to the slag-refractory interface, a metal Fe content up to 25.0 wt% was measured in some prills, sacrificing Mn. Inside the refractory, prills with average Mn content of 82.8 wt% were found, justifying the slag MnO gradient observed comparing Tables A.9 and A.10 in Appendix A.6. Major wetting of the electrode plate was observed.

Figure 4.41 visualizes the change in electrode plate thickness during experiment P.1a). Red and blue dots indicate plate cross section before and after the experiment, respectively. Green, dotted lines indicate slag-gas interface. Percentages quantify change in plate thickness during the experiment.

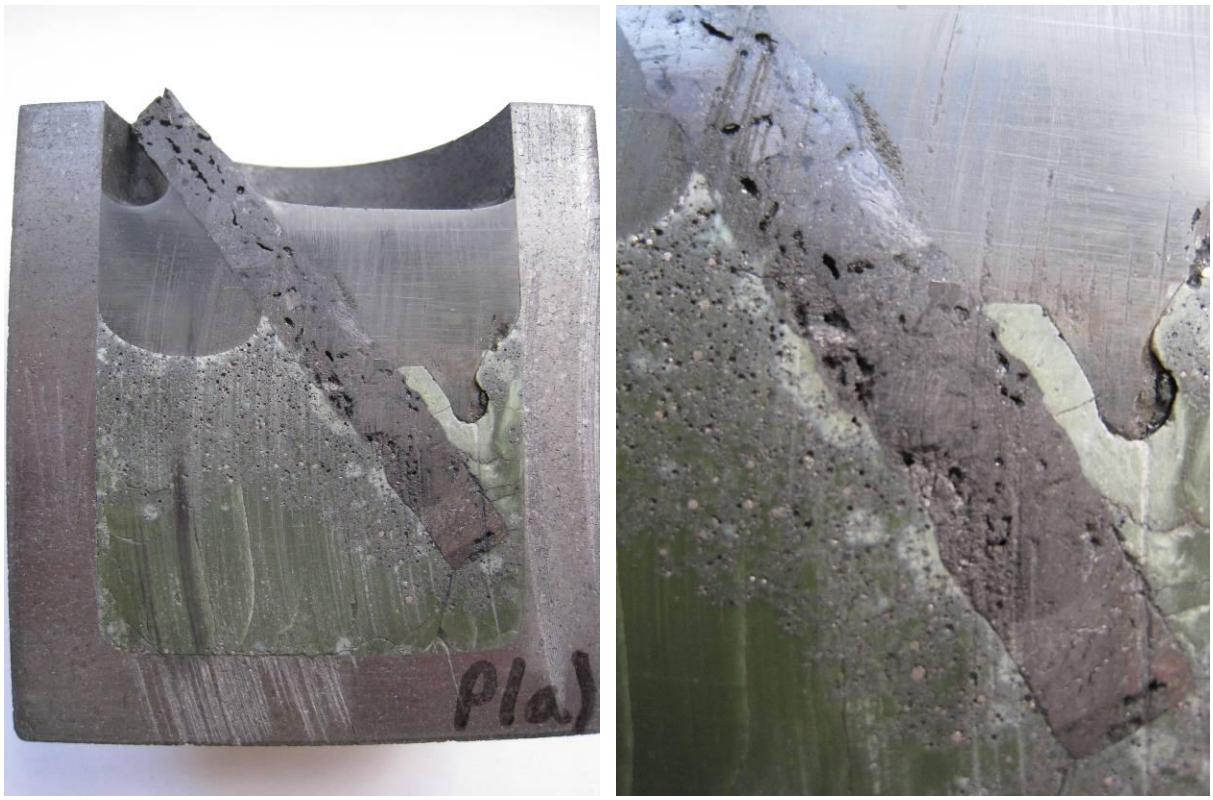

Figure 4.40: Intersected crucible after experiment P.1a). Left: Entire crucible. Right: Close-up

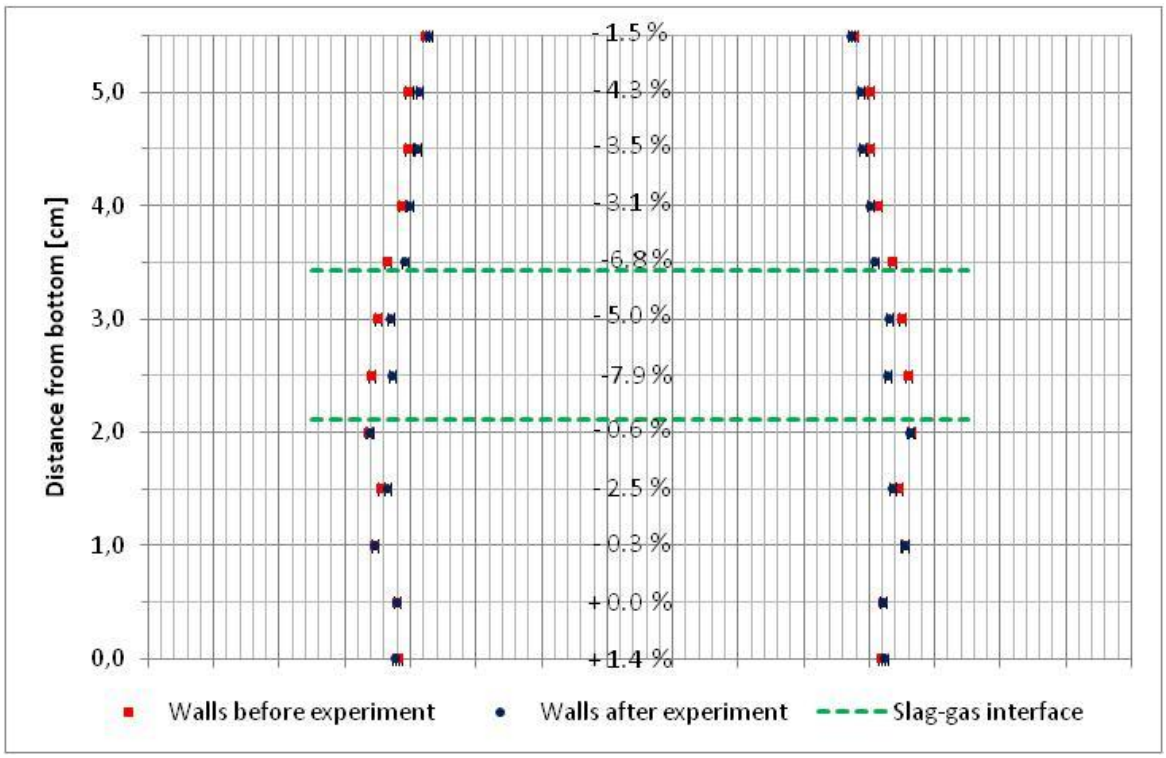

Figure 4.41: Wear profile experiment P.1a)

Close to the slag-gas interface, visualized in Figure 4.42, slag was observed to dissolve the refractory matrix, resulting in larger pieces of refractory(18a) being completely surrounded by slag(18b). White metal prills(18c), black gas pores(18d) and light grey SiC areas(18e) were also observed in this area. MnS clusters present in slag are barely visible in Figure 4.42.

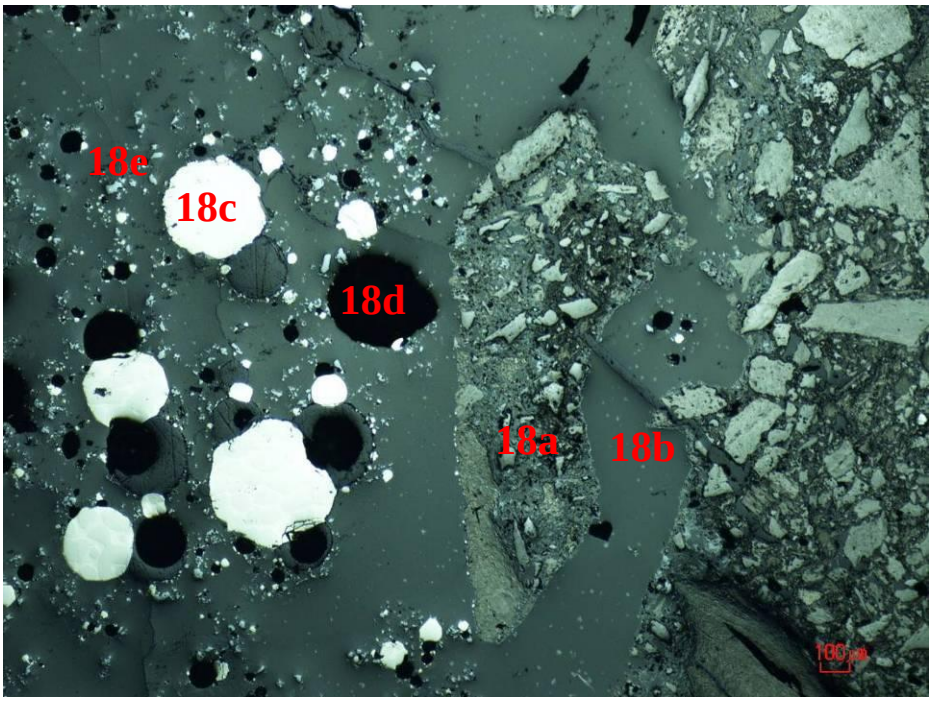

Figure 4.42: Slag surrounding a piece of refractory after experiment P.1a). Scale bar reads 100 µm.

Slag dissolving the matrix is better visualized in the backscatter electron SEM image in Figure 4.43, showing the grey slag phase penetrating and dissolving approximately 300 – 400 µm of the dark refractory phases:

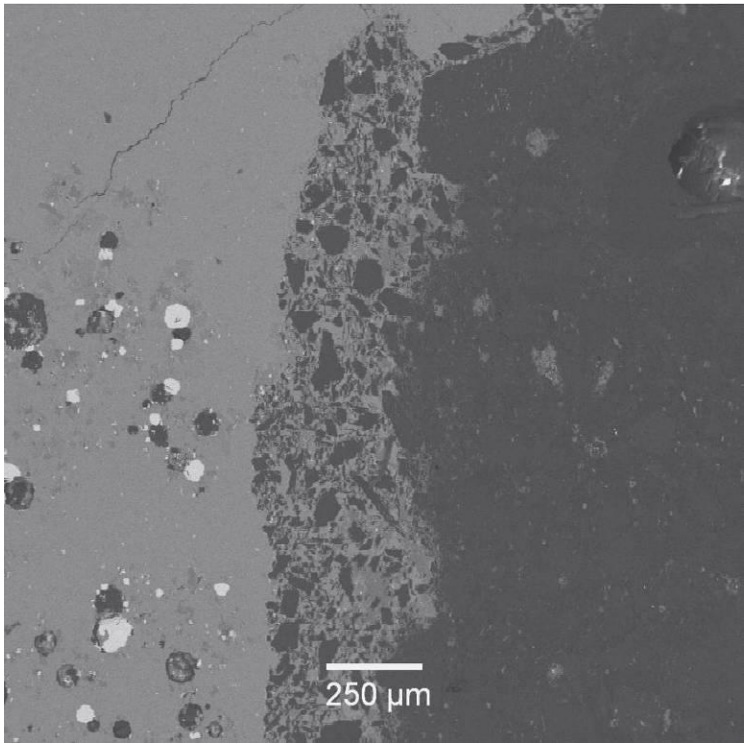

Figure 4.43: Slag dissolving and penetrating into refractory matrix during experiment P.1a)

A thin layer of SiC(19a) was observed at the slag-refractory interface, visualized in Figure 4.44. Metal prills(19b) with up to 88 wt% Mn were found inside refractory.

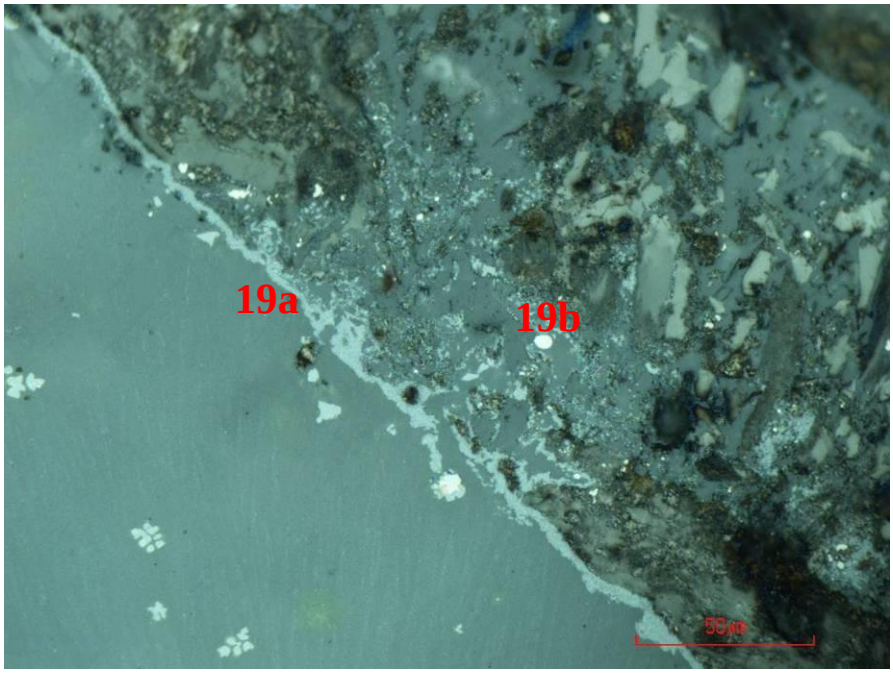

Figure 4.44: SiC formed on the slag-refractory interface during experiment P.1a). Scale bar reads 50 μm.

4.2.2 Electrode paste VS SiMn slag II

Figure 4.45 shows the intersected crucible after experiment P.2. Slag wetting of the electrode paste plate took place close to the slag-gas interface area, and limited slag-refractory interaction was observed here. Lower down in the crucible, slag-electrode paste contact and interaction was minimized. Gas bubbles and metal pearls with average composition 13.4 wt% Si, 74.6 wt% Mn and 11.6 wt% Fe were observed in the slag-gas interface area, and crystalline areas formed in the slag bulk during cooling. According to Tables A.9 and A.10 in Appendix A.6, no slag composition gradients can be concluded.

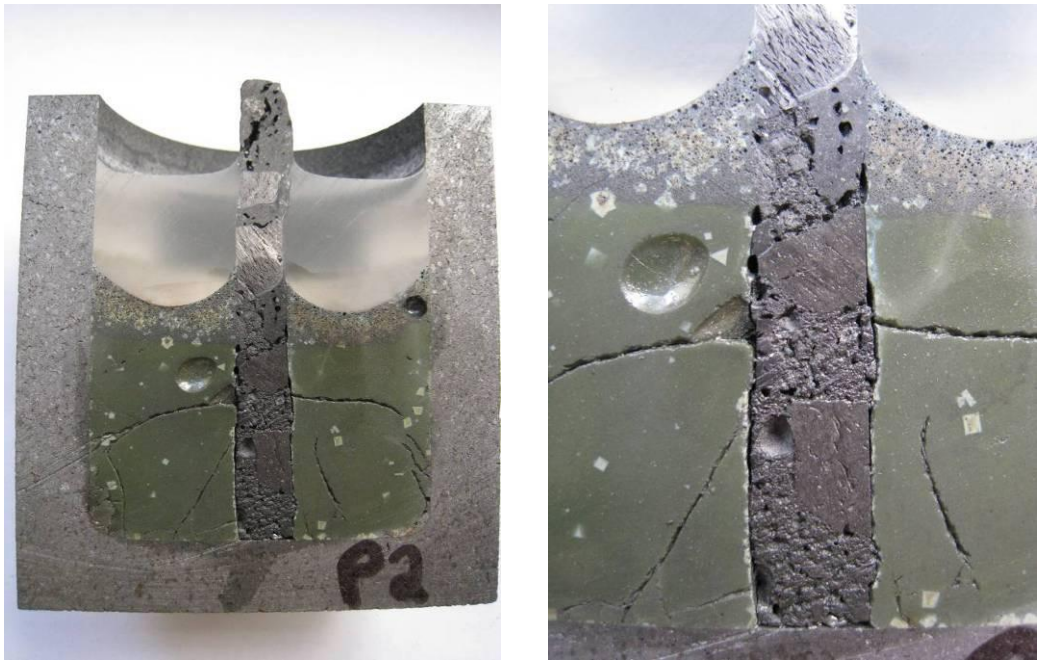

Figure 4.45: Intersected crucible after experiment P.2. Left: Entire crucible. Right: Close-up

Figure 4.46 visualizes the change in plate thickness during experiment P.2. Refractory wear was most extensive in and above the slag-gas interface area.

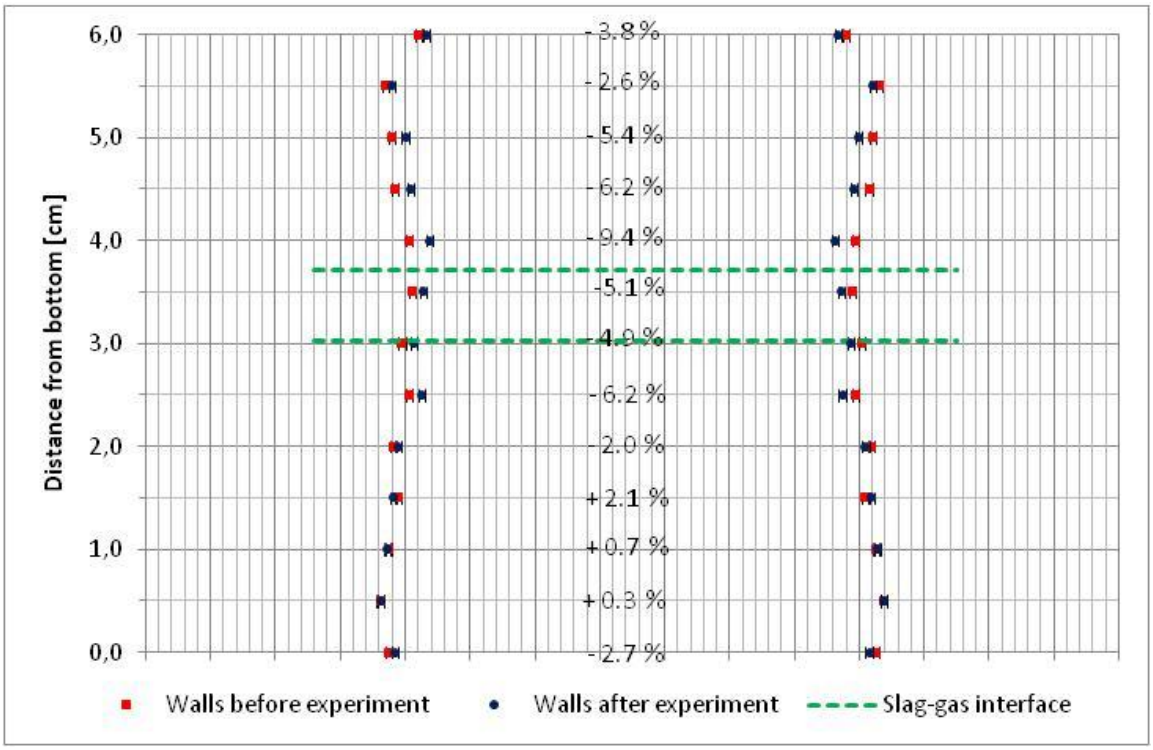

Figure 4.46: Wear profile experiment P.2

Figure 4.47 shows a backscatter image of grey slag dissolving the black refractory matrix. Less refractory material was dissolved during experiment P.2 compared to experiment P.1a).

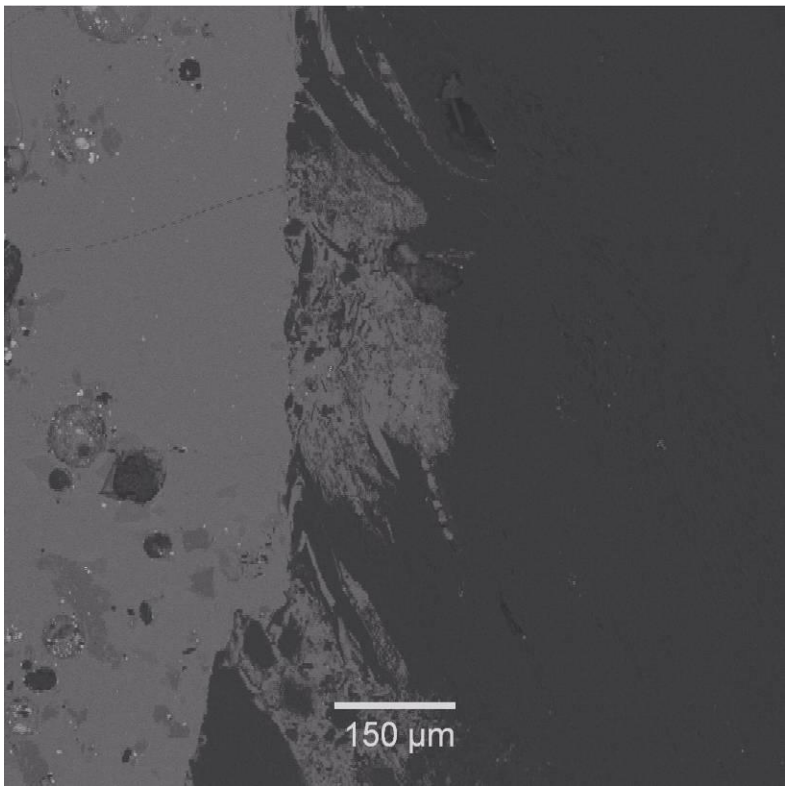

Figure 4.47: Slag dissolving and penetrating into refractory matrix during experiment P.2

Refractory particle disintegration is visualized in Figure 4.48:

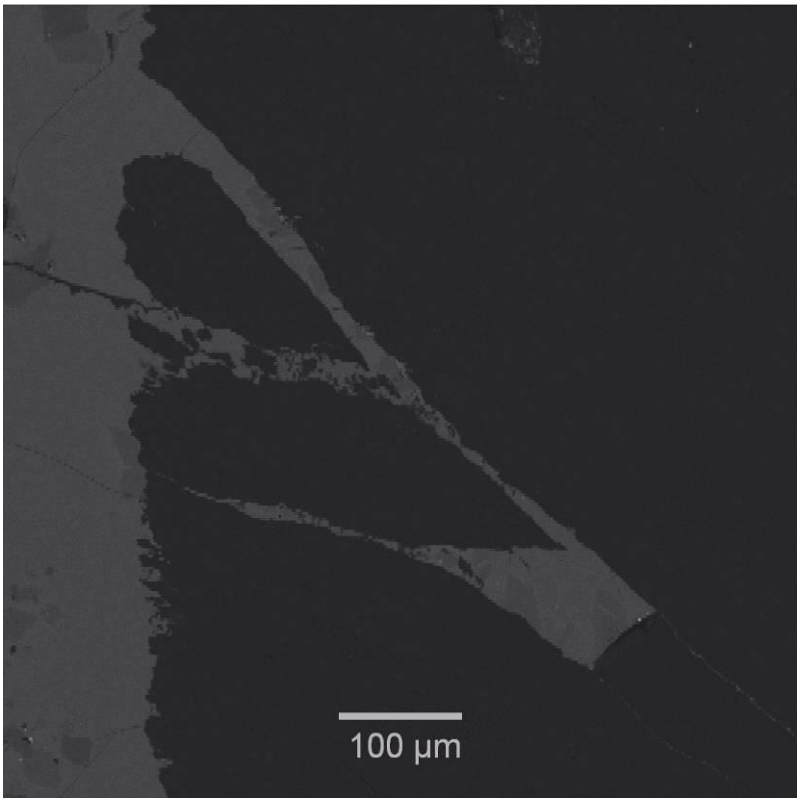

Figure 4.48: Refractory particle disintegration after experiment P.2

A SiC phase was observed at the slag-refractory interface after experiment P.2, similar to what was shown for experiment P.1a) in Figure 4.44 in Chapter 4.2.2. Figure 4.49 shows a C particle(20a) surrounded by SiC(20b) in the slag(20c) close to the slag-gas interface, visualizing refractory disintegration. Black areas(20d) are gas pores.

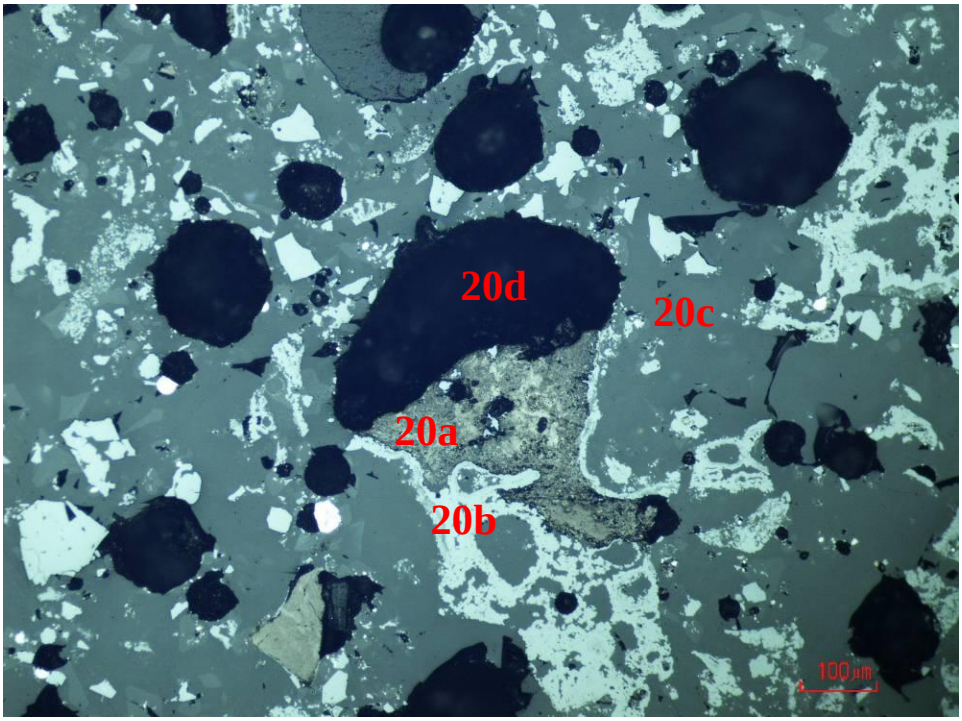

Figure 4.49: C particle observed close to slag-gas interface after experiment P.2. Scale bar reads 100µm

A low concentration of metal prills with up to 34.0 wt% Fe were found inside the refractory, but generally, slag-refractory interaction was limited during experiment P.2.

4.3 Mass considerations

Sample masses were recorded before and after each experiment quantifying the change in sample mass during the course of the experiment. Large scale gas formation is naturally accompanied by significant mass losses, and in this manner, measured mass changes indicate the nature of the interactions taking place within the system. During this investigation, possible gas forming processes were evaporation of volatiles and moisture, oxidation of graphite crucibles through equation (4.1) and gas liberating reduction reactions taking place between the refractory crucibles and process materials; e.g. direct metal oxide reduction with C(s) in accordance with equation (4.2):

$$(x+y)C(s)+\left(\frac{x}{2}+y\right)O_2(g)=xCO(g)+yCO_2(g) \quad (4.1)$$

$$M_xO_y(l)+yC(s)=xM(l)+yCO(g) \quad (4.2)$$

Mass changes presented in Table 4.1 were calculated with respect to total crucible masses before experiments:

Table 4.1: Mass changes during experiments

Experiment	Mass of process materials [g]	Total crucible mass before experiment[g]	Change in total crucible mass during experiment [%]
C.1a)	34.9680	323.51	-1.14
C.1b)	40.0162	328.29	-1.13
C.1c)	37.1906	323.74	-1.66
C.1d)	38.8866	321.20	-3.77
C.2a)	34.8867	315.79	-1.12
C.2b)	34.1267	324.85	-2.05
C.3	34.8412	648.65	-1.04
C.4	34.9615	645.10	-1.36
C.5	36.8638	386.69	-1.99
C.6	37.7102	385.14	-1.79
C.7	29.6644	398.72	-5.26
C.8	28.8762	403.98	-5.10
P.1a)	135.1482	382.34	- 0.59
P.2	132.5230	377.22	- 0.65

It can be observed that mass changes were in the range ~1 – 2 % during all crucible tests except experiment C.1d), conducted at a higher holding temperature, and for combinations involving tap hole clay crucibles, experiments C.7 and C.8. Mass losses during static plate tests P.1a) and P.2 were less than 1 %. Industrially, a mass change of 1 – 2 % is not considered significant[37]. Mass losses are discussed further in Chapter 5.1.5.

5. Discussion

5.1 Refractory wear mechanisms

Different refractories interact differently with corrosive and erosive process materials. Through the process of determining refractory wear mechanisms, critical components of the refractory materials can be identified and possibly improved for better refractory-process material compatibility. In this chapter, different possible mechanisms leading to refractory wear, as well as general trends observed after experiments, are discussed, and the following conclusions can be drawn:

- Slags not saturated in refractory components can dissolve oxides present in the refractory matrix, embedding larger refractory particles in slag.
- Gas formation and phase transformations during experiments can result in refractory particle cracking and disintegration.
- Metal prills observed after experiments were present initially, or were formed as a result of direct reduction or partial slag-metal equilibriums.
- Slags contain virtually no Fe_2O_3, so Fe found inside refractories after experiments most likely originates from Fe_2O_3 initially present in refractories.
- Minimal reduction of industrial slags was expected since equilibrium with C(s) at 1600°C should already have been established.
- SiC phases observed in the slags before and after experiments are expected to be SiC originally present in the slags, as well as SiC formed during the experiments.
- Gas pores present in slag after experiments are most likely evidence of gasses trapped by the slag surface tension.
- Mass losses during experiments were generally in the range ~1 – 2 %, thus not critical. Losses can be explained through evaporation of volatiles, C-oxidation, interaction between process and refractory materials and reactions within refractory materials.

5.1.1 Refractory matrix dissolution and refractory particle disintegration

Most refractories consist of particles bonded together by a matrix phase. C-based refractories investigated in this study contain oxide phases listed as ash in Table A.5 in Appendix A.3. Ash analyses presented in Table A.6 in Appendix A.3 show significant amounts of Al_2O_3, SiO_2 and Fe_2O_3. Considering the oxide nature of slags, there is a high possibility of interaction between the slag and the refractory matrix; slags dissolving the oxide rich phases. In order to avoid refractory matrix dissolution in slag it is therefore important that slags are saturated in refractory components. C particles are not soluble in the slag, but will be able to interact with metal phases not saturated in C.

Figure 5.1 shows examples of refractory matrix dissolution by slag after experiments C.1c) and P.1a). In Figure 5.1 – left, the slag penetrates and dissolves ramming paste matrix, while in Figure 5.1 – right, slag dissolves the electrode paste matrix. As discussed above, this is believed to be due to oxides from the refractory matrix dissolving in the slag liberating larger refractory particles.

Refractory particle disintegration was also observed after some compatibility experiments conducted during this investigation. Figure 5.2 shows examples of refractory particle disintegration after experiments C.4 and P.2. In Figure 5.2 – left, a SiC particle has cracked and disintegrated, while in Figure 5.2 – right, disintegration is observed for a C-particle present in electrode paste. Refractory particle disintegration can be due to gas formation in the

system followed by bubble bursting, or due to phase transformations in the material[38] resulting in expansion. This will be discussed further for specific refractories in Chapter 5.2.

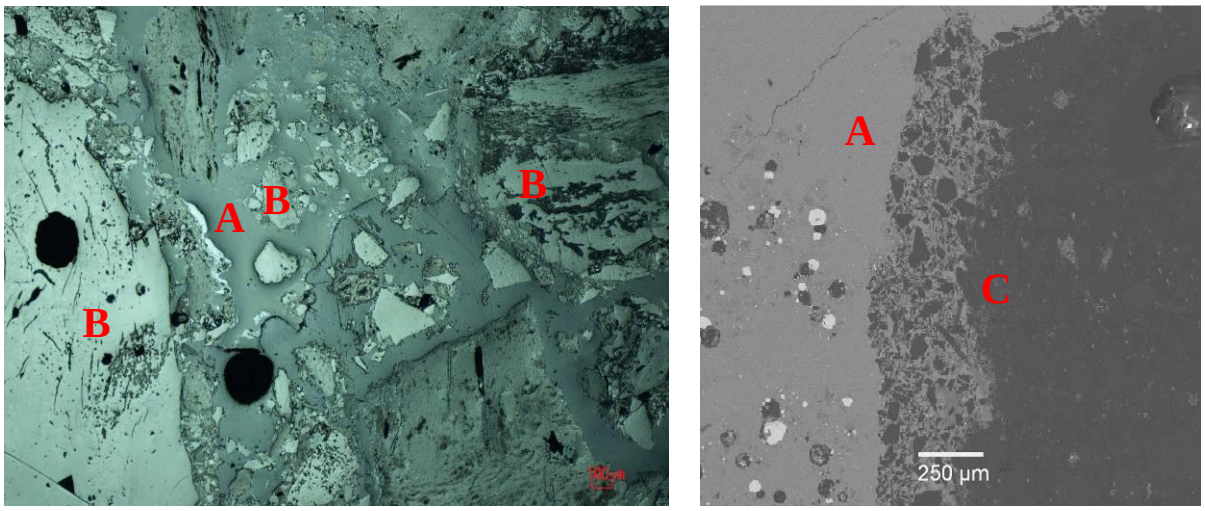

Figure 5.1: Refractory matrix dissolution by slag.
Left: Slag(A) dissolves ramming paste matrix and surrounds refractory particles(B). Scale bar 100µm.
Right: Slag(A) dissolves electrode paste(C) matrix.

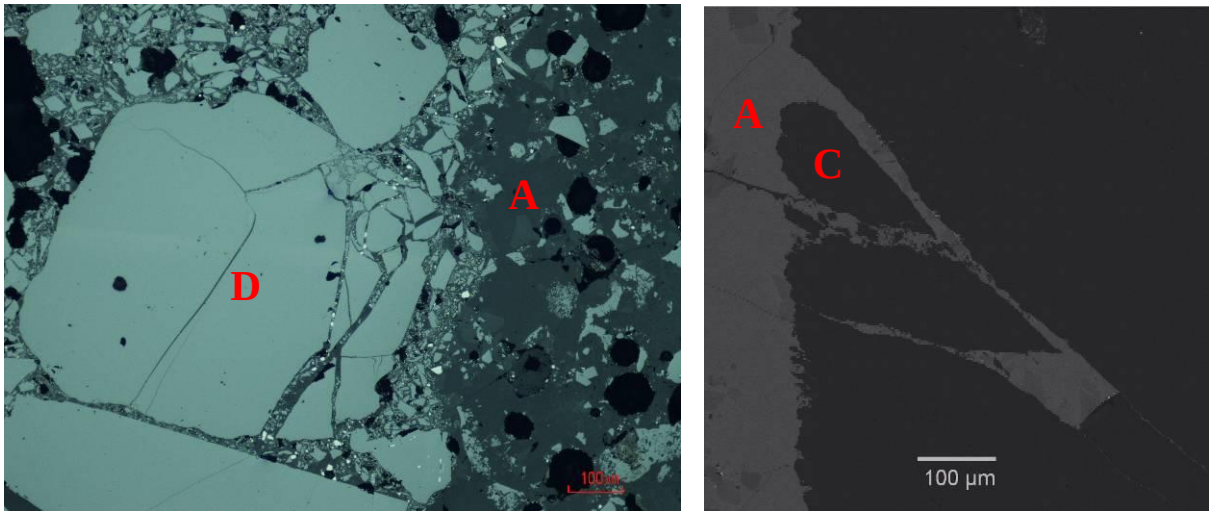

Figure 5.2: Refractory particle disintegration.
Left: SiC particle(D) disintegration and slag(A) penetration. Scale bar 100µm.
Right: C-particle disintegration and slag(A) penetration after electrode paste(C) experiment.

5.1.2 Oxide reduction mechanisms

Due to density differences between slag and metal, metal prills originally present in the SiMn slags were expected to be found below the slag after the experiments. Based on densities from SI Chemical Data[35] and slag and metal compositions in Tables A.2 and A.8 in Appendix A.3, respectively, the densities of SiMn metal I and II can be calculated to 6.40 g/cm^3 and 5.85 g/cm^3, respectively, while the densities of SiMn slag I and II are 3.33 g/cm^3 and 3.23 g/cm^3, respectively. Despite the large density differences between slags and metals, most of the metal prills were found close to the slag-atmosphere interface after the experiments. A relatively small concentration of metal prills was observed close to the slag-refractory interface and inside the refractory material. Results in Chapter 4 and in Tables A.12 through A.14 in Appendix A.6 show that metal prills found close to slag-gas interface can be assumed to exist naturally in the slag, while metal prills found closer to slag-refractory interface have increased

contents of Fe and/or Mn indicating slag-metal interaction. Metal prills found inside refractory have very high Fe or Mn contents, but with relatively small differences in Si content compared to metal prills found in bulk slag.

Observation of fine metal prills with increased Fe or Mn content close to and inside refractory might indicate interaction between slag and refractory, resulting in reduction of the most easily reducible oxides. In correspondence with the Ellingham diagram[11] shown as Figure A.1 in Appendix A.1, both Fe_2O_3 and MnO can be reduced by C(s) above 1425°C through reduction reactions shown as equations (5.1) and (2.7):

$$Fe_2O_3(l) + 3C(s) = 2Fe(l) + 3CO(g) \quad (5.1)$$

$$MnO(l) + C(s) = Mn(l) + CO(g) \quad (2.7)$$

According to Table A.2 in Appendix A.3, silica-rich SiMn slag I contains 0.34 wt% Fe_2O_3 and 7.37 wt% MnO, while SiMn slag II contains 0.11 wt% Fe_2O_3 and 2.94 wt% MnO, which indicates virtually no Fe_2O_3 in the slags. Also, since industrial slags were utilized during this investigation, equilibrium with C(s) at 1600°C should already have been established, and a low degree of reduction at 1367°C and 1464°C is expected. Still, reduced levels of MnO in the bulk slags and observations of MnO gradients after the experiments indicate that reduction of MnO has taken place. Refractory ash analyses in Table A.6 in Appendix A.3 suggest that metallic Fe stems from Fe_2O_3 originally present in the refractories, and that the refractory goes through "self-reduction" at high temperatures without interaction with the slag. Fe rich prills found inside refractories, but far from the slag phase, support this assumption.

The possibility of establishing partial slag-metal equilibriums also has to be evaluated, since partial slag-metal equilibriums are considered to be much faster than direct carbothermic reactions, as discussed in Chapter 2.1.4. During the establishment of partial slag-metal equilibriums, the least stable oxide is reduced to metal, donating the oxygen atoms to form more stable oxides. This process is expected to take place at the slag-metal interface. In the charged slags, Fe_2O_3 is the least stable oxide and can interact with Si and Mn in SiMn metal prills originally present in the slag. Partial slag-metal equilibriums shown in equations (5.2) and (5.3) may be established:

$$2Fe_2O_3 + 3Si = 4Fe + 3SiO_2 \quad (5.2)$$

$$Fe_2O_3 + 3Mn = 2Fe + 3MnO \quad (5.3)$$

SiO_2 is the most stabile of these two oxides, so the equilibrium in equation (5.2) is expected to establish as long as Si metal is present.

5.1.3 Silicon carbide

Silicon carbide particles, visualized as particle D in Figure 5.3 - left, were observed in slags both before and after heat treatment. After the experiments, a SiC "rim" was also often observed on slag-refractory interfaces with high concentrations of metal prills, visualized in Figure 5.3 – right.

Table A.15 in Appendix A.6 presents compositions of SiC phases after selected experiments. Deviation from 50 - 50 atom ratio is believed to be due to the use of EDS instead of more accurate equipment such as Electron Probe Micro-Analyzer (EPMA). However, the detection of Si and C peaks as the only plausible peaks in the X-ray spectra rule out a pure SiO_2 phase, and the non-spherical nature of the particles rule out the presence of metallic Si, since Si

metal melts at 1410°C[35]. Metallic Si would therefore have been molten at 1464°C, forming metal prills similar to the SiMnFe prills observed in Figure 4.18 in Chapter 4.1.3.

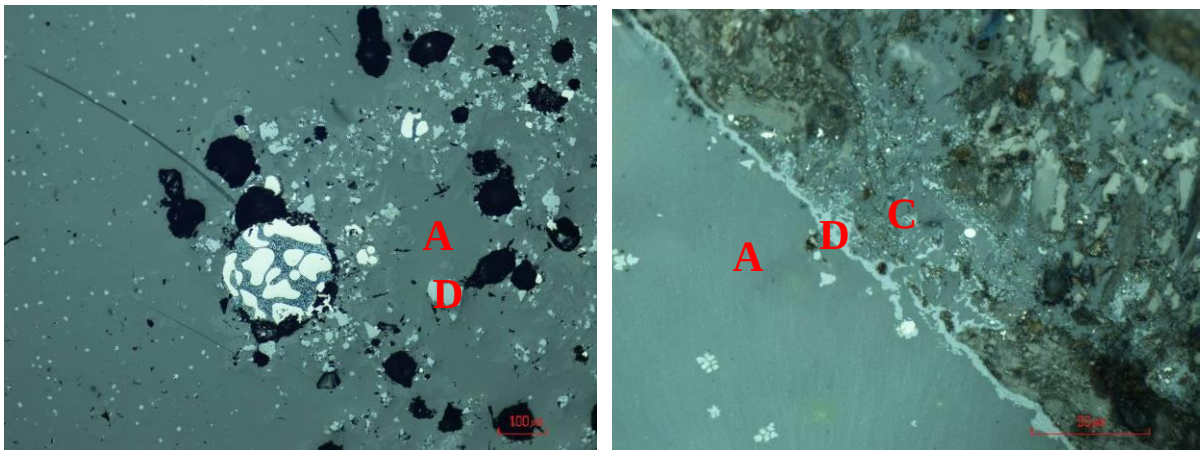

Figure 5.3: SiC observations after experiments. Left: SiC(D) originally present in slag(A). Right: SiC "rim"(D) formation on slag(A)-refractory(C) interface

According to Olsen, Tangstad & Lindstad[1], SiC is the stable carbon phase in molten SiMn metal with high Si and low C content. Park et al.[39] claim that SiC in the metal can be transported to the metal-slag interface in the furnace and might dissolve in the slag. This can explain why SiC phases were observed close to metal prills in the slag before heat treatment.

During heat treatment, formation of SiC might take place through reactions between Si and C and between SiO_2 and C, shown as equations (5.4) and (5.5):

$$Si(l) + C(s) = SiC(s) \quad (5.4)$$

$$SiO_2(s,l) + 3C(s) = SiC(s) + 2CO(g) \quad (5.5)$$

Based on Factsage[32] calculations, the reaction in equation (5.4) was found thermodynamically favorable at 1464°C, while the reaction in equation (5.5) only is thermodynamically favorable from 1515°C. At the slag-refractory interface, metal in the slag will be able to react with C(s) according to (5.4) upon establishment of favorable reaction kinetics. It can be assumed that reaction kinetics are favorable when Si is in the liquid state above 1410°C[35], and SiC is formed at the slag-refractory interface. Observations of SiC "rims" in areas with high concentrations of metal prills supports the assumption that SiC formation takes place through equation (5.4).

Formation of SiC on the slag-refractory interface can have a positive effect on refractory wear. As described in Chapter 2.3.3, SiC has high strength, advantageous thermal properties and excellent abrasion resistance, and can to some extent protect the refractories from wear caused by slag and metal. Visualized in Figure 5.3 – left; SiC was observed to form a continuous layer on some parts of the slag-refractory interface after compatibility experiments, however for improved protection, a continuous SiC layer is required. This did not form during most experiments.

5.1.4 Gas pore formation

All intersected crucibles except sample C.4 had large concentrations of gas pores close to the slag-gas interface. Gas pores might have been formed as a result of trapped gasses present from the beginning of the experiment, or might indicate gas formation due to oxide reduction during the experiments, in correspondence with equations (5.1) and (2.7).

Since the crucibles were charged with milled slags, air initially filled the volume between the slag particles. Based on charged masses shown in Table 4.1 in Chapter 4.3, calculated densities for the slags utilized and the volume of the crucible cavity, cavity fill factors at 25°C were in the range 40 – 50 %. The rest of the cavity volume was trapped air. Generally, density decreases with temperature, since its reciprocal, specific volume, generally increases with temperature. This should result in a higher fill factor at increased temperatures. The gas volume will also increase as a result of increasing temperature in correspondence with Charles' law.

During solid state heating, gasses present in the slag or inside the crucible walls were able to escape through the slag. Once the slag was molten, the slag viscosity and surface tension prevented gasses from escaping through the slag-gas interface, and gas pores were thus formed. Since most of the gas pores were found close to this interface, the slag surface tension appears to have been the main impediment for unrestricted gas movement.

As slag-refractory interaction was expected to take place when slag was in liquid state, produced gasses would also be prevented from escaping the system. A fraction of the trapped gas pores at the slag-gas interface is therefore expected to have contained reaction products.

5.1.5 Mass losses

Mass losses during experiments are presented as Table 4.1 in Chapter 4.3. Generally, mass losses were within ~1 – 2 %, which is negligible industrially[37]. Compared with Table A.5 in Appendix A.3, mass losses were generally lower than the volatile content of green refractories. However, since most of the refractory crucibles were baked before the experiments, mass losses cannot be explained through evaporation of volatiles, only.

For experiments utilizing a graphite shell to support the refractory materials, mass losses can be partly explained through possible oxidation of graphite. Figure A.11 in Appendix A.5 presents data from p_{O2} measurements during an experiment holding a ramming paste crucible at 1367°C for 4 hours. The data clearly shows that for the time spent at high temperatures, p_{O2} was above the critical limits for C(s) oxidation in correspondence with equations (A.2), (A.3) and (A.4). Large scale oxidation was however not observable during visual inspection of the graphite crucible after the experiment, possibly due to low graphite reactivity. Aspects ruling out low graphite reactivity are observable oxidation after crucible baking in a muffle furnace and after experiments C.1c) and C.2b), when the bottom furnace tube fittings were not tightly fastened. Another explanation for low visible graphite oxidation after p_{O2} measurements could be unfavorable reaction kinetics under the experimental conditions.

A gas leakage was discovered after experiment C.2b), possibly explaining the higher mass loss in samples C.1c) and C.2b) compared to the other combinations involving ramming paste. Increased holding temperatures compared to previous experiments should also imply more extensive interaction between refractory and slag, possibly leading to increased mass loss. Larger mass loss during experiment C.1d) can possibly be explained through interaction between SiMn slag I and ramming paste, forming metal as well as gasses escaping from the system. Volatiles and moisture are assumed to vaporize and escape during the baking process, although evaporation of volatiles will continue during experiments at increased temperature.

During experiments C.3 and C.4, SiO(g) could have been formed through equation (5.6):

$$2SiO_2(s,l) + SiC(s) = 3SiO(g) + CO(g) \tag{5.6}$$

Gas pores observed inside SiC crucibles after experiments and condensed SiO(g) found on the alumina support rod after experiments C.3 and C.4 support this statement.

Mass losses during experiments C.5 and C.6 are harder to account for, since insignificant levels of interaction between C tap block and refractory were observed both macroscopically and microscopically. Table A.5 in Appendix A.3 reports no surface moisture and a very low volatile content in this refractory material. However, since the carbon tap block crucibles were not baked before usage, vaporization of volatiles can be assumed to account for approximately half of the mass loss during the experiments. With a C content of 75.7 wt%, some oxidation of carbon can also be expected, even though no large scale oxidation was observed after experiments.

Experiments utilizing tap hole clay crucibles had the highest mass loss during this investigation. According to Table A.5 in Appendix A.3, tap hole clay has a higher volatile content than the other refractories investigated during crucible tests, and as stated earlier in this chapter, even though tap hole clay crucibles were preheated, continued evaporation of volatiles was assumed to take place during experiments. Since minimal slag-refractory interaction was observed upon crucible cutting, visualized in Chapters 4.1.7 and 4.1.8, mass losses can also be explained through reactions taking place within the refractory material: The mica mineral biotite has been showed to go through a dehydroxylation process[40] resulting in the loss of hydroxyl groups, OH^-, which will evaporate as steam. In air, this process takes place in three steps at ~400°C, ~800°C and above 1000°C. At low p_{O2}, some of the dehydroxylation steps are shifted to higher temperatures. Hydrothermal processes will also transform biotite to vermiculite[41], discussed further in Chapter 5.2.4.

Static plate experiments showed the lowest mass loss during the course of the experiment, contrary to Table A.5 in Appendix A.3 showing that green electrode paste has the highest level of volatiles of all refractories investigated. This indicates that most of the volatiles evaporated during baking. Static plate experiments were conducted using a graphite support shell, and due to the limited extent of interaction between slag and refractory, mass losses can most likely be explained through limited oxidation of the graphite.

5.2 Specific refractory wear

Depending on process and refractory materials, refractory wear can take place through several different mechanisms, as discussed in Chapter 5.1. This chapter discusses specific refractory wear for materials investigated, and the following conclusions can be drawn:

- Ramming paste cannot be considered suitable in contact with SiMn slag I at 1600°C. At 1367°C and 1464°C, slag-metal-ramming paste interaction through direct reduction and partial slag-metal equilibriums was observed. Holding temperatures during ramming paste crucible tests were shown to critically affect measured wear.
- Large scale SiC tap block wear was not proven, but microscopically, direct reduction of Fe_2O_3 was observed, as well as gas pores indicating SiO(g) and CO(g) formation.
- C tap block appears to be chemically stabile in contact with SiMn slags at 1464°C.
- Minimal slag-refractory interaction was observed during tap hole clay experiments, possibly due to incomplete slag melting. The expanding and insulating properties of the refractory material were demonstrated.
- Electrode paste wear took place through the interfacial convection mechanism, and the slags were observed to dissolve the refractory matrix as well as disintegrate refractory particles.

Table 5.1 presents a summary of refractory wear observed during this investigation for different combinations of process and refractory materials, holding temperatures and times. Abbreviations DR, SME and SF stand for direct reduction, partial slag-metal equilibrium and SiC formation, respectively:

Table 5.1: Summary of relative refractory wear observed during this investigation

Refractory	**Process material**	**Holding temperature [°C]**	**Holding time [hours]**	**Macroscopic wear**	**Microscopic wear**
Ramming paste	SiMn slag I	1367 ± 1.8°C	2	Less significant	Not investigated
Ramming paste	SiMn slag I	1367 ± 1.8°C	4	Less significant	Not investigated
Ramming paste	SiMn slag I	1464 ± 2.1°C	4	Significant	Refractory penetration and disintegration, DR, PSME, SF
Ramming paste	SiMn slag I	1600 - 0.6°C/ + 0.2°C	4	Extensive	Not investigated
Ramming paste	SiMn slag II	1367 ± 1.8°C	2	Less significant	Not investigated
Ramming paste	SiMn slag II	1464 ± 2.1°C	4	Significant	Refractory penetration and disintegration, DR, PSME, SF
SiC tap block	SiMn slag I	1464 ± 2.1°C	4	Not significant	Refractory matrix dissolution, SiC particle disintegration, gas formation, DR
SiC tap block	SiMn slag II	1464 ± 2.1°C	4	Not significant	Refractory matrix dissolution, SiC particle disintegration, gas formation, DR
C tap block	SiMn slag I	1464 ± 2.1°C	4	Not significant	DR, SF
C tap block	SiMn slag II	1464 ± 2.1°C	4	Not significant	DR, SF
Tap hole clay	SiMn slag I	1464 ± 2.1°C	4	Less significant	Refractory expansion, incomplete melting, DR, PSME, SF
Tap hole clay	SiMn slag II	1464 ± 2.1°C	4	Less significant	Refractory expansion, incomplete melting, DR, PSME, SF
Electrode paste	SiMn slag I	1464 ± 2.1°C	2	Less significant	Interfacial convection, refractory matrix dissolution, DR, PSME, SF
Electrode paste	SiMn slag II	1464 ± 2.1°C	4	Less significant	Interfacial convection, refractory matrix dissolution, particle disintegration, DR, PSME, SF

5.2.1 Ramming paste wear

After experiments involving ramming paste, slag was observed to have disintegrated the refractory, and metal prills with high Fe content found close to large refractory particles suggest direct reduction of oxides by C(s) present. Reduced MnO contents in bulk slags were observed. These results indicate a mix of the two oxide reduction mechanisms described in Chapter 5.1.2:

Firstly, Fe_2O_3 in slag is reduced in contact with SiMn prills initially present forming SiO_2 through the slag-metal equilibrium in equation (5.2). However, the slags utilized in this investigation were industrial slags containing virtually no Fe_2O_3, indicating that partial slag-metal equilibriums should already be established and Fe should exist as metal initially. Secondly, Fe_2O_3 and MnO are reduced through direct reduction by C(s) in contact with large refractory particles. As discussed in Chapter 5.1.2, reduced Fe_2O_3 is believed to originate from the refractory material itself. Since most Fe-rich metal prills are found in close proximity to refractory particles, the second step is expected to take place at the largest extent.

SiC particles were observed in the slag and on the slag-refractory interface. Based on the discussion in Chapter 5.1.3 it is plausible that SiC was formed during the experiment.

Comparing the macroscopic wear profiles of experiments C.1c) and C.2b) presented in Figure 4.7 in Chapter 4.1.1 and Figure 4.13 in Chapter 4.1.2, respectively, SiMn slag II seems to be causing less ramming paste wear than SiMn slag I. This is the opposite trend of what is experienced industrially, where SiMn slag II has been observed to be more corrosive towards the refractory lining. The trend observed during this investigation can however in no way be considered conclusive, since only one wear test was conducted at every experimental condition. Industrially, the interaction temperatures are also expected to be higher. For more conclusive results, experiments should be repeated.

Observations of crystalline areas after ramming paste experiments may be a demonstration of the thermal properties of the refractory material. Formation of crystalline areas includes nucleation and growth processes[42]; nucleation being the slowest. Nucleation can take place in a homogeneous or heterogeneous manner, the latter requiring the presence of nucleation points. Crystal formation within the bulk slag may therefore indicate the presence of solid particles, possibly SiC, in the liquid slag, while formation of crystalline areas close to the cavity wall may indicate that heat transfer in the refractory wall is slower than in the bulk slag. Generally, refractory materials are assumed to have superior heat transfer properties, indicating that the crystalline slag areas in Figure 4.10 - right most likely have a different melting point than the bulk slag due to interactions with the refractory wall. As described in Chapter 2.4.5, a decreased liquidus temperature is expected as a result of increased MnO content in the slag. A lower MnO content was measured in the slag forming the crystalline slag phase, so increased liquidus temperature is expected. Rapid heat transfer at the slag-refractory interface will therefore result in faster slag solidification at the interface than for the bulk slag. Dendrite formation was then possibly a result of slag composition.

Except for metal prills on the cavity wall and bottom, the crucible cavity appears to be empty after experiment C.1d) conducted at 1600°C, as observed in Figure 4.8 in Chapter 4.1.1. Clearly, slag has penetrated into the ramming paste, and MnO, Fe_2O_3 and SiO_2 may possibly have been reduced in correspondence with the Ellingham diagram[11] in Figure A.1 in Appendix A.1 and equations (5.1), (2.7) and (2.8). As discussed in Chapter 5.1.2, slag-C(s)

equilibrium at 1600°C should already have been established in the industrial slags, and further reduction was not expected to take place.

$$SiO_2(s,l) + 2C(s) = Si(l) + 2CO(g) \quad (2.8)$$

Upon cutting, a white phase was observed inside the refractory material, most likely consisting of a mix of Fe, Mn and Si metal, as well as oxides Al_2O_3, CaO and MgO not reducible by C(s) at 1600°C. Studying the interaction further in an optical microscope and in the SEM would be very interesting, but time limitations unfortunately prevented this. However, as expected, increased wear compared to experiments conducted at a lower temperature can be concluded, and ramming paste cannot be considered suitable in contact with SiMn slag I at 1600°C.

Figure 5.4 visualizes the effect of holding temperature and time on ramming paste wear by SiMn slag I during crucible tests, based on wear profiles in Chapter 4.1.1. Percentage change in affected crucible cavity diameter is plotted as a function of height in the crucible for experiments C.1a) through C.1d). The grey area indicates change that has to be tolerated due to uncertainty in diameter measurements:

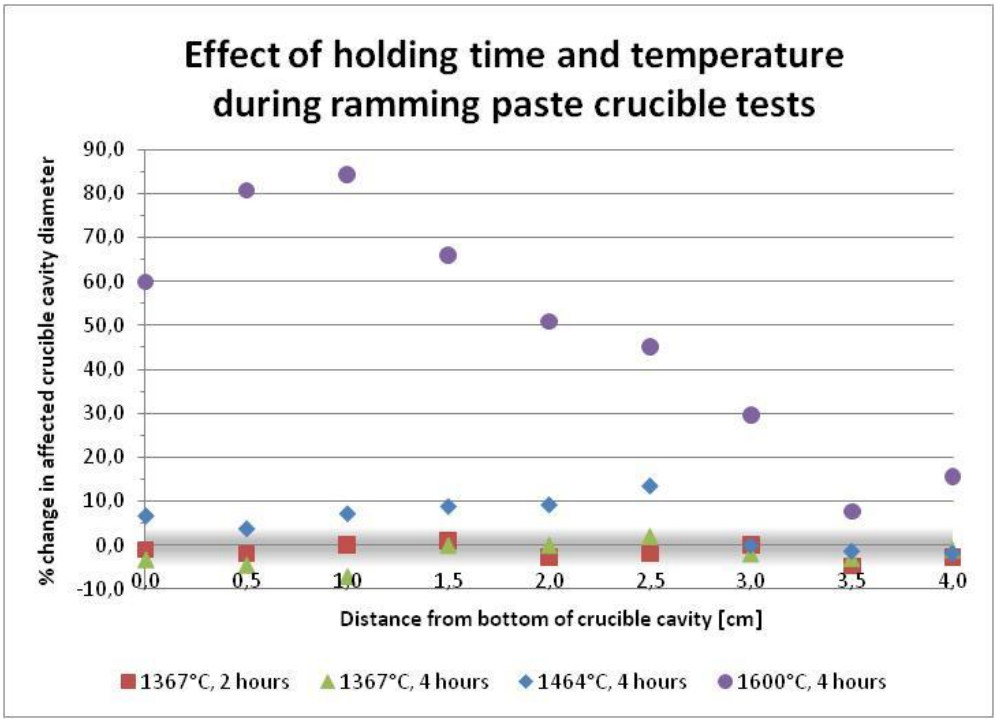

Figure 5.4: Comparison of relative wear of ramming paste by SiMn slag I as a function of holding time and temperature. Grey area indicates change within uncertainty.

It can be observed that temperature had a large effect on the measured wear after the ramming paste crucible tests, as expected. Measured wear profiles after experiments conducted at 1367°C showed insignificant change in cavity diameter. Significant wear was measured below the slag-gas interface when the holding temperature was increased to 1464°C; percentage change increasing towards the slag-gas interface 1.5 – 3.0 cm from the cavity bottom. Above the slag-gas interface, measured change was insignificant due to measurement uncertainties.

Experiment C.1d) conducted at 1600°C was dramatically different from the other three experiments investigating the combination of ramming paste and SiMn slag I. Refractory

wear increased 12 times 1 cm above the crucible bottom compared to experiment C.1c) at 1464°C, and change in affected area was most extensive in the bottom parts of the crucible. From Figure 4.8 in Chapter 4.1.1 it can be observed that the slag penetrated all the way to the graphite support shell, and it is expected that penetration would have continued further, if possible. Penetration is also a function of the force used to ram the refractory material into the support shell, highlighting the importance of uniform ramming.

Doubling the holding time did not have a significant effect at 1367°C, but increased holding time is expected to result in significantly increased refractory wear at 1464°C and 1600°C.

5.2.2 Silicon carbide tap block wear

According to wear profiles in Figures 4.15 and 4.20 in Chapters 4.1.3 and 4.1.4, respectively, no significant macroscopic wear of SiC could be proven. Optical microscope images in Figures 4.16 and 4.18 and Figures 4.21 through 4.23 show that slag is interacting with SiC on a microscopic level.

The SiC crucible wall is porous, and slag penetrates easily into the refractory structure. XRD analyses in Table A.3 in Appendix A.3 show that the SiC tap block contains SiO_2, which is possibly dissolved in slag during experiments. Metal prills with high Fe content were observed far from the slag bulk, indicating reduction of Fe_2O_3 within the refractory. This can take place through reduction with SiC according to equation (5.7) or through the partial slag-metal equilibriums in equations (5.2) and (5.3). As stated previously: Since industrial slags were used, partial slag-metal equilibriums are expected to be established already, so Fe was most likely formed through the reaction in equation (5.7). The origin of Fe_2O_3 is uncertain, since industrial slags contain virtually no Fe_2O_3. An XRF analysis of SiC tap block ash is expected to show amounts of Fe_2O_3 present in the tap block binder phase.

$$Fe_2O_3(s,l) + SiC(s) = 2Fe(l) + SiO_2(s,l) + CO(g) \tag{5.7}$$

MnO gradients in the slags, visualized in Figure 4.17 in Chapter 4.1.3, and large concentrations of gas pores observed inside the refractory wall indicate reduction of MnO in contact with SiC. Turkdogan[43] lists possible gas forming reactions taking place at the interface of MnO slags and SiC particles:

$$3MnO(l) + SiC(s) = 3Mn(l) + SiO_2(s,l) + CO(g) \tag{2.15}$$

$$2SiO_2(s,l) + SiC(s) = 3SiO(g) + CO(g) \tag{5.6}$$

$$MnO(l) + SiC(s) = Mn(l) + SiO(g) + C(s) \tag{5.8}$$

Of these three reactions, only equation (2.15) is thermodynamically favorable at 1464°C according to Factsage[32] calculations assuming activities equal to 1. According to Davidsen[44], the activity of SiO_2 at 1464°C in slags with compositions similar to the slags utilized in this study is ~0.30 for both SiMn slag I and II. This reduces the driving force for the reaction in equation (5.6) additionally. The activities of MnO at 1464°C were estimated to ~0.026 and ~0.012 for SiMn slags I and II, respectively[44]. The extent of the reactions in equations (2.15) and (5.8) also depends on the activity of Mn in the metal prills.

Even though equations (5.6) and (5.8) are not thermodynamically favorable at 1464°C, observations of reaction products can however still be expected since product gasses will escape from the system upon establishment of local equilibriums, assuring a constant slight shift to the right.

Park et al.[39] studied dissolution of SiC particles in CaO-SiO_2-MnO slags at 1600°C and predicted increased dissolution and gas formation with increasing CaO/SiO_2 ratio in slag, based on agreements between experimental results and calculations utilizing FactSage[32]. The researchers also stated that increased gas formation at higher CaO/SiO_2 ratios results in faster mass transport through the boundary layer, accelerating reaction kinetics. According to Table A.2 in Appendix A.3, SiMn slag II has a higher CaO/SiO_2 ratio than SiMn slag I, so increased gas formation is expected to have taken place during experiment C.4. This trend is also indicated by Table 4.1 in Chapter 4.3, showing increased mass loss after experiment C.4 compared to experiment C.3. Condensed SiO(g) was observed on the alumina support rod after experiments C.3 and C.4 confirming that one or both of the reactions in equations (5.6) and (5.8) have taken place to some extent. Low MnO content in slag found inside refractory wall indicates that equation (5.8) was most dominant. Refractory particle cracking and disintegration observed in Figure 4.22 in Chapter 4.1.4 may thus be a result of gas bubbles bursting at the slag-refractory interface.

Cracking and disintegration of particles are also typical indications of expansion as a result of phase transformations[38]. The phase transformation from cubic β-SiC to hexagonal or rhombohedral α-SiC takes place at ~1700°C, and over 200 different polytypes of α-SiC involving minor variations in stacking sequence are known from the literature[44]. XRD analyses in Table A.3 in Appendix A.3 show that the SiC tap block investigated consists of hexagonal and rhombohedral SiC polymorphs, α-SiC. Since the holding temperature during experiments C.3 and C.4 was lower than 1700°C, SiC particles may have gone through a phase transformation to β-SiC, or minor phase transformations between α-SiC polytypes, during the experiments, possibly causing SiC particle cracking and disintegration.

The observation of pure Si metal and increased SiO_2 content combined with very low MnO content in slag inside a SiC particle in Figure 4.23 in Chapter 4.1.4 might also indicate SiO(g) formation according to equation (5.8). As the gas was trapped inside the SiC particle, condensation according to equation (2.30) followed during cooling:

$$2SiO(g) = Si(s,l) + SiO_2(s,l) \tag{2.30}$$

An increased level of interaction is expected at higher temperatures, based on thermodynamic calculations in Factsage[32], as well as accelerated reaction kinetics due to increased gas formation as stated by Park et al.[39] Decreased slag viscosity at higher temperatures will ease slag penetration into refractory pores. Increased macroscopic wear as a result of chemical interaction can therefore be expected.

5.2.3 Carbon tap block wear

Compared to the other refractory materials investigated, C tap block crucibles were relatively unaffected by SiMn slags at 1464°C. According to Figures 4.25 and 4.29 in Chapters 4.1.5 and 4.1.6, respectively, no macroscopic wear of carbon tap block crucibles could be proven. Optical microscope images in Figures 4.26 and 4.27 and Figures 4.30 through 4.32 confirm that microscopic interaction also was minimal during experiments C.5 and C.6. Minimal interaction may be due to low reactivity of the graphite of which the carbon tap block is manufactured, limited wetting, low porosity or slow reaction kinetics.

According to Table A.5 in Appendix A.3, C tap block has a large ash content only exceeded by tap hole clay. SiMn slags I and II contain 0.98 wt% and 0.81 wt% K_2O, respectively, which according to Silva et al.[22] can react with Al_2O_3 and SiO_2 present in refractory ash to form kaliophilite and leucite in accordance with equations (2.27) and (2.28), described in

Chapter 2.4.2. Alkali attack has been shown[20,22] to be most prominent in the temperature range 800 – 1100°C, forming liquid phases resulting in structural spalling of the refractory material.

$$K_2O(s,l) + Al_2O_3(s) + 2SiO_2(s) = K_2O \cdot Al_2O_3 \cdot 2SiO_2(l) \quad (2.27)$$

$$K_2O \cdot Al_2O_3 \cdot 2SiO_2(l) + 2SiO_2(s) = K_2O \cdot Al_2O_3 \cdot 4SiO_2(l) \quad (2.28)$$

Even though the slag-refractory system passed through the critical temperature range both during heating and cooling, the occurrence of structural spalling cannot be proven.

The C tap block appears to be chemically stabile in contact with SiMn slags at 1464°C, but increased interaction can be expected at higher temperatures and longer interaction times. Utilizing other refractory wear tests exposing the refractory to wear mechanisms such as thermal stress and erosion may result in more extensive refractory wear.

5.2.4 Tap hole clay wear

Minimal interaction between slag and refractory was observed after experiments involving tap hole clay crucibles. A few metal prills with increased Fe content and a SiC phase were observed close to the slag-refractory interface, as well as some Fe-rich metal prills inside the refractory. This indicates the establishment of a partial slag- metal equilibrium as Fe_2O_3 in the slag reacts with Si in the metal prills according to equation (5.2) and direct reduction of Fe_2O_3 inside the refractory according to equation (5.1). SiC observed on the slag-refractory interface can be considered to be a reaction product as Si reacts with C(s) according to equation (5.4), discussed in Chapter 5.1.3.

As discussed in the previous chapter, and in accordance with Table A.5 in Appendix A.3, tap hole clay has the largest ash content of all the refractories investigated. Structural spalling due to alkaline attack was therefore expected, but results in Chapters 4.1.7 and 4.1.8 show that this cannot be concluded.

After the experiments involving tap hole clay, clay expansion was observed decreasing the size of the crucible cavity. The expansion process can be explained as exfoliation, a property characteristic of the mica mineral vermiculite upon intense heating[41]. According to Table A.4 in Appendix A.3, the green tap hole clay utilized during this investigation did not contain vermiculite, but contained the vermiculite-related minerals biotite, chlorite and kaolinite. Biotite is known to convert to vermiculite upon hydrothermal alteration[41], as mentioned in Chapter 5.1.5. Chlorite and kaolinite are both associated with vermiculite, being products of hydrothermal processes and weathering, respectively[45]. Tap hole clay expansion was also observed after baking, indicating that 4 hours at 800°C is sufficient to start the biotite to vermiculate alteration process for clay with 2.5 wt% moisture content. Expansion of tap hole clay can be considered very useful in order to assure tight plugging of the tap hole between taps.

Based on wear profiles in Figures 4.34 and 4.38 in Chapters 4.1.7 and 4.1.8, respectively, SiMn slag I seems to promote the expansion of clay, while SiMn slag II was observed to hinder clay expansion. As described in Chapters 4.1.8 and 4.1.9, small gas pores and grain contours were observed in both slags after the experiment, and was explained as incomplete slag melting during tap hole clay experiments. Incomplete slag melting can also explain the difference in regions of significant clay expansion: SiMn slag I was probably less viscous

than SiMn slag II during the course of the experiments, meaning that a larger fraction of SiMn slag I was in the liquid state allowing the refractory to expand.

Incomplete slag melting in bottom areas of the cavity during experiments is a demonstration of the insulating properties of tap hole clay. At higher temperatures, complete slag melting is expected, resulting in increased interaction between slag and refractory.

5.2.5 Electrode paste wear

During experiments investigating electrode paste wear, most of the slag-refractory interaction took place close to the slag-gas interface. This type of refractory wear can be explained through the interfacial convection mechanism suggested by Dunkl[7], visualized in Figure 2.27 a) in Chapter 2.5.5. In correspondence with this mechanism, refractory wear takes place mostly at the slag-gas interface due to density differences between glass melt and glass melt saturated with refractory components. In this case: As slag dissolves the refractory matrix, slag saturated with reaction products sinks while fresh slag continues the refractory attack.

As described in Chapters 4.2.1 and 4.2.2, SiMn slag I was observed to dissolve 300 – 400 μm of the refractory matrix during 2 hours at 1464°C, while SiMn slag II was observed to dissolve ~200 μm of the matrix as well as disintegrating some larger refractory particles during 4 hours at the same temperature. This indicates that SiMn slag I did more damage to electrode paste than SiMn slag II.

Metal prills with high contents of Fe were found in slag close to the refractory, and metal prills with high content of Mn were observed inside refractory. This indicates both partial slag-metal equilibrium and direct reduction mechanisms in correspondence with equations (5.1) through (5.3) and equation (2.7). Table A.6 in Appendix A.3 shows that electrode paste ash contains Fe_2O_3 available for reduction in contact with C(s) at high temperatures, and Table A.9 and A.10 in Appendix A.6 justify MnO reduction through a measured MnO gradient in the slag after experiment P.1a). A thin SiC phase was formed through equation (5.4) on parts of the slag-refractory interface during both experiments.

Since slags were shown to dissolve refractory matrix at 1464°C, increased interaction is expected at higher temperatures, possibly causing as much damage as observed for ramming paste at 1600°C.

5.3 Relative refractory wear

General trends and individual wear mechanisms discussed in Chapter 5.2 form a solid foundation for a relative comparison of the refractory materials investigated. In this chapter, relative refractory wear, as well as factors influencing refractory wear, are discussed, and the following conclusions can be drawn:

- The ramming paste investigated was not compatible with SiMn slags.
- SiC tap block and electrode paste showed incipient signs of refractory disintegration and should be investigated further.
- C tap block and tap hole clay were found to be compatible with SiMn slags.
- Refractory porosity seemed to have greater effect on refractory wear than ash content.
- Measured wear profiles indicate that SiMn slag I was more corrosive towards ramming paste and electrode paste than SiMn slag II.

5.3.1 Refractory compatibility with process materials

Based on results in Chapter 4 and discussions in Chapters 5.1 and 5.2, the following compatibility table can be constructed, shown in Table 5.2:

Table 5.2: Compatibility table

Refractory / Process material	Ramming paste	SiC tap block	C tap block	Tap hole clay	Electrode paste
SiMn slag I	Non-compatible	Non-conclusive	Compatible	Compatible	Non-conclusive
SiMn slag II	Non-compatible	Non-conclusive	Compatible	Compatible	Non-conclusive

Ramming paste experiments showed incipient refractory disintegration at 1464°C, and at 1600°C, SiMn slag I penetrated completely into refractory walls. SiMn slag I can therefore be considered to be non-compatible with the ramming paste investigated, and suitable replacements should be considered. Since SiMn slag II showed similar behavior as SiMn slag I at 1464°C, non-compatibility is expected at 1600°C.

Insignificant macroscopic wear was observed after SiC tap block experiments at 1464°C. Microscopically, slag-refractory interaction was observed, and increased interaction is expected at increased temperatures. Results are non-conclusive, and SiC tap block wear should be investigated further.

Electrode paste wear showed similar trends to ramming paste wear at 1464°C, and increased wear at 1600°C is thus expected. Electrode paste wear should be investigated further before compatibility conclusions can be drawn.

C tap block experiments showed insignificant macroscopic wear at 1464°C as well as minimal microscopic wear. Even though increased interaction is expected at 1600°C, the C tap block investigated seems to be compatible with SiMn slags.

Insignificant macroscopic wear was measured after tap hole clay experiments at 1464°C, and minimal interaction was observed microscopically. However, indications of non-complete slag melting were observed, most likely limiting the extent of slag-refractory interaction. Based on the experiments conducted during this investigation, tap hole clay seems to be compatible with the process materials investigated, although different conclusions might be drawn upon experiments achieving complete slag melting.

5.3.2 Factors influencing refractory wear

As discussed in Chapter 5.1.1, slags can dissolve oxide phases serving as refractory binder, resulting in refractory disintegration. XRD analyses of refractory ash in Table A.6 in Appendix A.3 show that oxide phases within refractories contain Fe_2O_3 which can be reduced in contact with C(s). In accordance with Table A.5 in Appendix A.3 and results in Chapter 4, tap hole clay and C tap block have the highest ash contents, although show the lowest degree of refractory wear. Ramming paste, SiC tap block and electrode paste have lower ash content, but are more porous than C tap block and tap hole clay. Larger measured wear was observed after the experiments investigating the three porous refractories. With increased refractory porosity, slag is allowed to penetrate into the refractory materials, possibly interacting with

oxide phases increasing the porosity further. Comparing relative refractory wear as a function of refractory compositions and properties, porosity seems to have a larger effect on refractory wear than ash content.

Compositions, basicities and estimated viscosities and liquidus temperatures for the slags utilized in this investigation are presented in Table 3.2 in Chapter 3.1. Based on these data, only minor differences in slag behavior were expected. Industrially, SiMn slag II has been observed to cause more refractory wear than SiMn slag I, but during this investigation, the opposite seemed to be the case:

Based on wear profiles in Chapter 4.1, SiMn slag I caused more macroscopic ramming paste wear than SiMn slag II. For electrode paste, SiMn slag I caused as much refractory wear during 2 hours at 1464°C as SiMn slag II did during 4 hours at 1464°C. After SiC tap block, C tap block and tap hole clay experiments, wear profiles were non-conclusive with respect to difference in slag behavior.

Based on mass changes in Table 4.1 in Chapter 4.3, mass losses were larger after the experiment investigating SiMn slag II in combination with SiC tap block than after SiMn slag I in combination with SiC. This can possibly be explained through a higher CaO/SiO_2 ratio for SiMn slag II as discussed in Chapter 5.2.2. For C tap block and tap hole clay, mass changes were smaller after SiMn slag II experiments, but only 0.20 % and 0.16 %, respectively. After electrode paste experiments, mass losses were small and almost identical, possibly indicating that SiMn slag I is more corrosive due to difference in holding times during experiments. Non-conclusive results were observed after ramming paste experiments.

Since mass losses during experiments were small and virtually negligible, difference in mass losses between experiments cannot be used to draw conclusions regarding difference in slag behavior. As discussed in Chapter 5.1.5, mass losses were most likely due to other factors than slag-refractory interaction, such as evaporation of volatiles and C oxidation. Wear profiles provided a more reliable basis for conclusions regarding difference in slag behavior. Difference in slag behavior can thus only be concluded after experiments investigating ramming paste and electrode paste, and based on one experiment per material combination, SiMn slag I seems to have caused more refractory wear than SiMn slag II.

5.4 Evaluation of test methods and equipment

Refractory wear testing involves thorough test selection among the tests described in Chapter 2.5. Different wear mechanisms are dominant during different tests, so depending on test selection, different results can be acquired, possibly leading to test-specific conclusions for situations not necessarily resembling the industrial conditions desirable for investigation. In this chapter, the selection of refractory wear tests and the furnace setup utilized during this investigation are evaluated, and the following conclusions can be drawn:

- The crucible test is preferred in many cases due to its simplicity and ease of repeatability, while the static plate test is valued for depicting the most realistic wear at isothermal conditions accompanied with good reproducibility.
- Dynamic tests will provide information regarding wear mechanisms more critical for tap hole refractories such as thermal stress and erosion. Crucible and static plate tests are more suitable for initial investigations of refractories to be used inside the furnace.
- Ideally, a different furnace should have been utilized during this investigation allowing for rapid heating of the sample, combined with furnace design allowing for sample quenching upon heat treatment.

Both refractory wear tests utilized during this investigation are classified as static tests, not taking into account thermal stress and erosion wear mechanisms. As described in Chapters 2.5.3 and 2.5.5, respectively, the crucible test visualizes wear as a result of chemical interaction between slag and refractory as well as structural spalling due to slag penetration into refractory, while the static plate test visualizes interfacial convection and free density convection mechanisms. However, when investigating industrial SiMn furnace tap hole wear, examining thermal stress and erosion mechanisms are probably more relevant, since the tap hole is opened and plugged several times every day allowing slag and metal to be tapped from the furnace. Tap hole refractories are therefore to a high extent exposed to thermal stresses and erosive media, possibly causing refractory wear. Utilizing isothermal static wear tests will in this case only give an indication of the situation at the tap hole hot face when the tap hole is plugged. Crucible and static plate tests can therefore be considered more suitable for initial investigations of refractories to be used inside the furnace. Dynamic tests will give indications of the erosive effects of fluid motion, and induction furnace tests can establish a horizontal temperature gradient in the refractory for thermal stress investigations. However, as stated in chapter 2.5.3, the crucible test is often preferred due to its simplicity and ease of repeatability, and serves as a good starting point and reference for refractory behavior evaluation.

Based on work drawings in Appendix A.4, a maximum of 22.1 cm^3 process material was in contact with a maximum of 40.3 cm^2 refractory surface area during the crucible tests conducted as a part of this investigation. This gives a volume-to-surface ratio of ~0.5. Due to surface roughness, the effective cavity surface area can be assumed to be larger, resulting in an even lower volume-to-surface ratio. During the static plate tests, a maximum of 74.5 cm^3 process materials were in contact with a maximum of 27.0 cm^2 refractory surface area. This gives a volume-to-surface ratio of ~2.8. Electrode paste plate surface roughness results in a larger effective surface area, decreasing the volume-to-surface ratio. A low volume-to-surface ratio leads to slags rapidly becoming saturated with reaction products from slag-refractory interaction, drastically reducing the driving force for refractory corrosion[7]. Slags will also be rapidly depleted of alkalis due to alkali diffusion, resulting in an unrealistically low alkali attack of the refractories, if applicable. The higher volume-to-area ratio during static plate tests reduces these effects and also allows for optimal development of convection flow in the system. Based on comparisons of static crucible, finger and plate tests, Dunkl[7] concluded that the static plate test gives the most real refractory wear at isothermal conditions accompanied with a good reproducibility, as stated in Chapter 2.5.11.

The slow heating and cooling rates utilized during this investigation most likely had an effect on the refractory wear observed after the experiments. Even though the holding times and temperatures were specifically defined for each experiment, reactions taking place during heating and cooling cannot be differentiated from reactions taking place during holding at maximum temperature. However, assuming that the slag-refractory interaction only took place after the slags reached liquid state, the four hours holding time at 1464°C still is twice the amount of time it took to heat and cool the samples from liquidus temperatures ~1300°C to 1464°C. Also, based on the temperature dependency of the reaction rate constant, k(T), expressed as the Arrhenius equation shown in equation (5.9), the main part of the interaction most probably took place during the four hours at holding temperature. In equation (5.9), A is the pre-exponential factor, E_a is the activation energy, R is the gas constant and T is temperature.

$$k(T) = A \cdot \exp\left[\frac{E_a}{RT}\right] \tag{5.9}$$

Ideally, the sample should have been heated rapidly to the specific holding temperatures and cooled rapidly through quenching to freeze all reactions in the state they occurred at high temperatures. Due to furnace design, sample quenching upon holding was difficult, and furnace material properties prevented rapid heating to high temperatures. The recommended heating and cooling rates for an Al_2O_3 furnace tube depend on tube diameter; larger diameter tubes resulting in increased brittleness at high temperatures. For the Φ_{outer} = 91 mm furnace tube utilized during this investigation, the recommended heating and cooling rates are in the range 2 – 5°C/min[46]. Graphite tubes have excellent thermal properties allowing for increased heating and cooling rates: The maximum heating rate for a graphite tube with Φ_{outer} = ~70 mm is 40°C/min[47], making it possible to heat the tube from room temperature to 1500°C in 75 minutes. Heating rates of 25°C/min[46] and 45°C/min[48] have been achieved utilizing induction furnaces, and as described in Chapter 2.5.6, utilization of an induction furnace allows for the establishment of a horizontal temperature gradient in the samples as well as slag convection. An infrared furnace can achieve heating rates of up to 1200°C/min[46] depending on sample size and reflectivity. For the sample sizes utilized in this investigation, such extreme heating rates would not be obtainable, but it can be assumed that considerably improved heating rates could be obtained utilizing an infrared furnace.

In conclusion, a different furnace than the Al_2O_3 tube furnace allowing for rapid heating of the sample should be utilized, and changes to the design making sample quenching possible should be considered, in order to produce conclusive temperature specific results for slag-refractory interaction at high temperatures. However, a full experimental series exposing the samples to identical heating programs, shown in Table 3.4 and Figure 3.15 in Chapter 3.5.1 and Table 3.5 in Chapter 3.5.2, was completed during this investigation, and a comparison of the investigated refractories can be done based on their relative behavior under identical conditions.

5.5 Experimental uncertainties

Temperature and diameter measurements served as important sources of information with regard to furnace control and industrial relevance of compatibility experiments, and for visualization of macroscopic wear profiles during this investigation, respectively. In this chapter, uncertainties in the temperature and diameter measurements are discussed, and the following conclusions can be drawn:

- Temperature logging system inaccuracies introduced the most critical uncertainties in temperature conditions during the experiments.
- Several methods are available for temperature validations, and based on the required level of accuracy during this investigation, the wire-bridge method was utilized.
- Upon conducting temperature validations, the author feels confident that the uncertainties in temperature measurements during this investigation were quantified, and that reported sample holding temperatures are accurate within ± 1.8°C at 1367°C, ± 2.1°C at 1464°C and - 0.6°C / + 0.2°C at 1600°C.
- An uncertainty of ± 0.05 cm has to be tolerated for inside diameter measurements before experiments, while an uncertainty of ± 0.005 cm can be expected for diameter measurements after experiments. A diameter change within ± 2 % can therefore not be considered conclusive for macroscopic refractory wear.
- For increased sensitivity during quantification of macroscopic refractory wear, utilization of more accurate technology should be explored.

5.5.1 Uncertainties in temperature measurements

In a compatibility study of refractory materials and process materials, the choice of interaction temperature plays a very important role. Safe to say, the temperature in the system affects almost every aspect of the interaction, including thermodynamics and kinetics, and choice of temperature should therefore be based on the industrial conditions desirable for investigation. Temperature measurements during the experiments served to confirm the temperature in the system, and it was therefore of outmost importance that these measurements were reliable.

A B-type thermocouple made from Pt alloyed with 30% Rh and Pt alloyed with 6% Rh wires was used to control the Carbolite PVT 18/80 vertical tube furnace utilized in this investigation. This thermocouple has a range from 0 – 1700°C[49] during continuous operation, but can be used up to 1860°C[50] for short periods of time. Commercial producers[49] indicate an accuracy of ±0.5°C above 800°C when used under inert or slowly oxidizing conditions. Naturally, thermocouples age, so the accuracy will be lower for older thermocouples. It is also important to remember that inaccuracy in temperature readings depends, not only on the thermocouple, but on the temperature logging system as a whole, including extension wires and data logging unit.

An R-type thermocouple made from pure Pt and Pt alloyed with 13% Rh wires was used to measure the temperature inside the furnace tube during the experiments. Recommended operating range for this type of thermocouple is 0 – 1650°C[50] under oxidizing conditions, but the thermocouple can be used up to 1760°C[51] for short periods of time. According to WIKA[52], R-type thermocouple (tolerance class 1) accuracy is within ± 1.0°C in the temperature range 0 – 1100°C and [1 + (Temperature - 1100) x 0.003]°C in the temperature range 1100 – 1600°C.

At sample temperature 1600°C, measured by the R-type thermocouple inside the furnace tube, the furnace temperature, measured by the B-type thermocouple inside the furnace wall, was 55°C higher. This difference is believed to be due to the relative distance from the heating elements: The B-type thermocouple was placed between two heating elements inside the furnace wall, while the R-type thermocouple measured the temperature inside the furnace tube, affected by all six heating elements, but at a greater distance from all of them. This temperature difference had to be taken into consideration when selecting furnace set points.

When recording the temperature gradients shown in Figures 3.9 and 3.10 in Chapter 3.3, the R-type thermocouple measured the temperature inside an alumina tube in the center of the furnace tube. The alumina tube will, due to its low thermal conductivity, have an effect on the measured temperature, but this cannot be considered critical at the temperatures of operation. During the experiments, the R-type thermocouple measured the temperature inside an alumina tube 22.5 mm from the center of the furnace tube. Based on temperature gradients and measured temperatures during experiments presented in Figures 3.9, 3.10 and 3.15 in Chapters 3.3 and 3.5.1, the horizontal temperature gradient at a specific height in the hot zone of the furnace tube can be considered negligible as it is within 1°C.

Uncertainties in thermocouple readings can have dramatic effects, both in terms of controlling experimental conditions and the general safety of researchers conducting experiments. Inaccuracies in the B-type thermocouple readings could in this case possibly cause a furnace meltdown, since the B-type thermocouple output served as the main source of information for the Eurotherm 818P Programmer controlling the furnace. Also, the furnace controller had to be configured for the thermocouple type installed in the furnace, considering that each

thermocouple type has a unique output voltage to temperature relationship. Since the thermocouple was replaced, and the furnace was maintained shortly before start of experiments; B-type thermocouple aging and thermocouple-furnace controller miscommunication was not considered to be critical for this investigation.

Inaccurate R-type thermocouple readings greatly influenced the experimental conditions during this investigation. The thermocouple was used to record temperature gradients at set points 1500°C and 1520°C and to measure the temperature close to the sample during experiments. Since both the thermocouple and the data logging unit were brand new before the experiments, the temperature measurements were considered accurate readings of actual sample temperatures, and furnace set points were therefore adjusted accordingly. As described in Chapter 3.4, miscommunication within the components of the data logging unit was detected during the experimental series, resulting in an ~80°C drop in temperature readings per additional thermocouple connected to the unit. The actual experimental temperatures were later shown to be ~133 – 136°C lower than initially measured.

Upon repair of the data logging unit, the wire-bridge method was utilized to validate temperature measurements, as described in Chapter 3.4. Based on accuracy estimates provided by Crovini et al.[34], the wire-bridge method was found sufficiently accurate for this investigation, but several other temperature validation and calibration techniques are also available: In the pyrometallurgical industry[53], the principle of redundancy is commonly used, involving measuring critical temperatures utilizing several independent thermocouples. This allows for critical evaluation of temperature measurements, since values that are clearly different from the average can be disregarded. In pottery[54], pyrometric cones are used to verify kiln conditions before glazes are fired. The cones contain refractories and melting agents and are carefully designed to soften in a certain temperature range under certain atmospheric conditions.

The fixed point method can be applied for high-accuracy thermocouple calibrations. This method involves constructing a fixed point cell, utilizing the established melting point of a metal[55] or a eutectic[56]. The voltage output of the thermocouple is measured as the cell is heated and cooled through the melting point of the metal or eutectic, and melting and freezing plateaus are observed. It has been proved that melting plateaus show the highest degree of reproducibility and are most suitable for accurate thermocouple calibration[56].

Upon conducting temperature validations, the author feels confident that the uncertainties in temperature measurements done after data logger unit repair have been quantified. At 1367°C, the formula provided by WIKA[52] indicates an R-thermocouple accuracy of ± 1.8°C. Comparing this value with the temperature logging system offset at the melting points of Au and Pd shows reasonable agreement. At holding temperature 1600°C, temperature validations indicated an average temperature offset in the range 0.2°C ± 0.4°C for the temperature logging system as a whole. This value is significantly better than the R-thermocouple accuracy of ± 2.5°C suggested by WIKA. Holding temperature 1464°C was estimated based on change in furnace set points and temperature responses measured before data logger unit repair. WIKA indicates an R-type thermocouple accuracy of ± 2.1°C at 1464°C, and based on temperature validations at melting points of Au and Pd, this seems reasonable for the temperature logging system as a whole. It can therefore be concluded that the temperature histories presented in Figure 3.15 in Chapter 3.5.1 describe the actual heat treatment of the samples within experimentally verified uncertainties.

5.5.2 Uncertainties in diameter measurements

An inside caliper was used to measure the inside crucible diameter before each crucible test. Due to lack of scale bars on the inside caliper, a vernier caliper was utilized to quantify the inside diameter using a unique distance-to-distance relationship: Based on distance measurements at a specific point on the inside caliper at different caliper openings, diameter estimations could be produced having an uncertainty of ±0.05 cm. At an ideal cavity diameter of 2.5 cm this represents ± 2 %.

Utilization of several calipers and the developed relationship between them introduce systematic errors dependent on the researcher's interpretation. In order to avoid introducing even larger systematic errors in inside diameter measurements, it is therefore recommended that each researcher develops a unique "scale" relating inside caliper distances.

Material integrity was a challenge during inside diameter measurements, especially for ramming paste crucibles. In certain positions, the inside caliper would exert to large of a force on the crucible wall, causing damage and possibly increasing the inside diameter. During crucible cutting this was taken into consideration, as intersection was done preferentially in areas not damaged during preliminary measurements.

A vernier caliper was used to measure the inner crucible diameter after the experiments. When the caliper nonius was utilized, the uncertainty of this instrument was ± 0.005 cm. At an ideal cavity diameter of 2.5 cm this represents ± 0.2 %.

Uncertainties in the diameter measurements affected the measured wear profiles, and a diameter change within ± 2 % could not be considered conclusive for macroscopic refractory wear by the process materials. A more sensitive method for determining change in crucible cavity diameter would be desirable.

Minteq spinoff Ferrotron has developed a system for non-contact measurements of refractory linings in metallurgical reaction and transport vessels[57]. The LaCam® refractory lining measuring system is specially designed for electric arc furnaces and provides the tools to monitor refractory linings within 0.635 cm (¼ inch) accuracy. The technology utilizes a laser scanner to monitor the residual brick thickness of the refractory, brick development, rate of wear of different refractory materials, EAF volume and shell deformation. Utilizing this technology, the need for manual measurements is rendered unnecessary, increasing the safety and accuracy involved in providing data as a basis for informed management of the EAF refractory-lining system. If 0.635 cm accuracy can be achieved for large industrial furnaces, a downscaled LaCam® refractory lining measuring system may also achieve satisfying accuracies for refractory crucibles of the size utilized in this investigation. For further investigations, the possibility of utilizing laser technology to provide accurate crucible cavity profile measurements should therefore be explored.

5.6 Industrial relevance

The main purpose of compatibility studies is to investigate refractory behavior during interaction with the specific process material under simulated industrial conditions. Conducting experiments in laboratory scale is a lot easier and less resource demanding than experimenting at the plants, and the risks of damage to personnel and valuable equipment are reduced considerably. However, in order for test results to be of industrial relevance, test methods and experimental conditions must be thoroughly selected in order to simulate industrial conditions. Also, taking into account the intended usage of the refractory material, a

certain degree of wear might be acceptable for some components of the refractory lining, but might be critical for others, and alternative refractory materials should be utilized. In this chapter, the industrial relevance of this investigation is discussed, and the following conclusions can be drawn:

- Even though experimental holding temperatures were lower than industrial tapping temperatures, results from compatibility tests are still industrially relevant due to temperature gradients within tap block during tapping.
- It can be assumed that ramming paste is responsible for two of the burn-throughs serving as entry point of this investigation. Replacements should be explored.

5.6.1 Temperature offset

Initially, industrial slag tapping conditions were selected as a basis for the compatibility tests. Due to the miscommunication within the data logging unit described in Chapter 3.4, holding temperatures were confirmed to be ~133 – 136°C lower than intended. Even though industrial tapping temperatures were not reached during most experiments, the presence of a temperature gradient within the tap block during tapping, visualized in Figure 5.5, supports the relevance of the compatibility experiments conducted during this investigation:

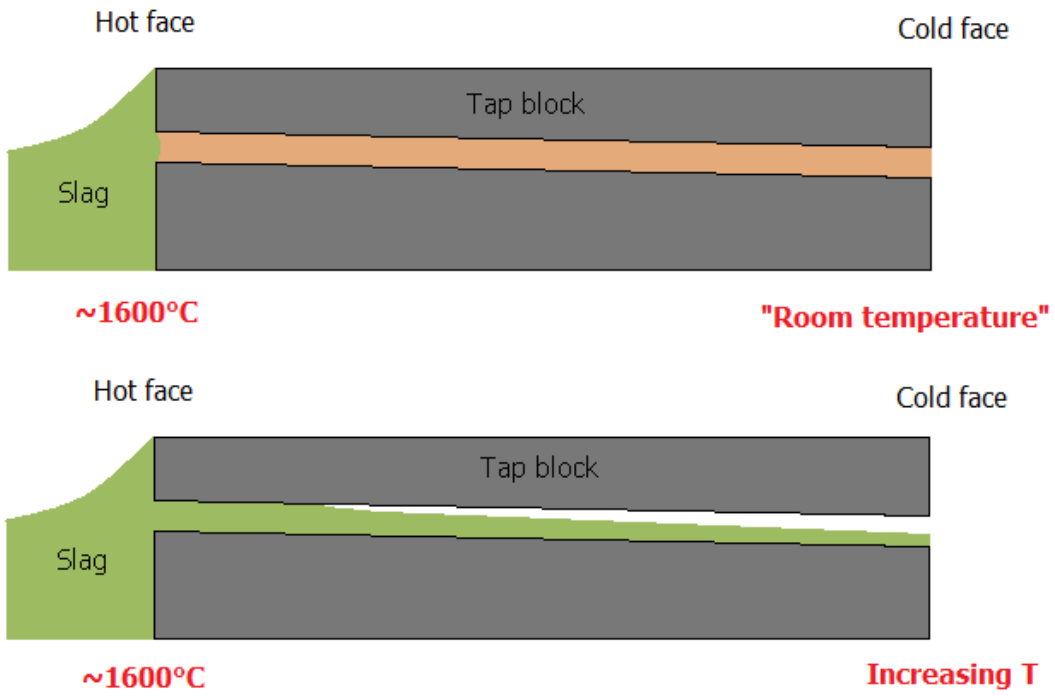

Figure 5.5: Cross section of tap blocks. Top: Plugged tap hole. Bottom: Open tap hole.

As observed in Figure 5.5, the temperature at the hot face of the tap block is assumed to be ~1600°C both when the tap hole is plugged and when it is open. At the cold face, the temperature is at "room temperature" when the tap hole is plugged, and increasing due to the flow of slag or metal when the tap hole is open. At some point within the tap block, slag at 1464°C interacts with refractory during tapping. Also, if critical wear is observed at 1464°C, wear will be even more extensive at 1600°C. Even though interaction conditions during tapping are not static, static wear tests at 1464°C serve as useful starting points for slag-refractory interaction, evaluated more thoroughly in Chapter 5.4.

5.6.2 Refractory lifetime

In accordance with tap hole descriptions in Chapter 2.2.2, different lifetimes are required for the different refractories utilized in the tap hole area., A certain degree of wear can be tolerated for some refractories, while for others, wear is more critical. Conducted in parallel with an ongoing Ph.D. study of an industrial SiMn tap hole, this investigation provides useful indications of which tap hole refractories that should be investigated in more detail as a part of the Ph.D. study.

Tap blocks are expected to last for a considerable amount of time, preferably years, while tap hole clay is replaced after every tap. Electrode paste used for tap hole maintenance is replaced every week, while ramming paste is used to repair the tap block until next major relining where a new tap block can be installed. Preferably, compatibility tests involving industrial time perspectives would be ideal, but since this is not possible, particularly for tap blocks both from a time and cost perspective, conclusions have to be made based on measured refractory wear after shorter amounts of time. If critical wear mechanisms are observed to take place after only 4 hours at industrial temperatures, significant wear can be expected after longer periods of time. Tap block wear during compatibility tests would therefore be an indication that more investigations should be conducted to explore the behavior of the tap block in contact with process materials. Clearly, the tap hole clay lifetime in contact with process materials is much shorter, and some wear can be tolerated. Even if incipient tap hole clay wear caused by interaction with process materials is observed, temperature gradients within the tap block will result in frozen process material within the tap hole obstructing further refractory wear.

Critical ramming paste wear was revealed during this investigation, calling for more detailed studies, possibly investigating several types of ramming paste, in order to find a ramming paste more suitable for this usage. A possible explanation for the series of occurrences serving as the entry point of this investigation can be suggested as follows: After the original tap block was damaged during lancing resulting in a burn-through in the tap hole area, the ramming paste used to repair the tap hole can be held responsible for the two burn-throughs following shortly after.

6. Conclusion

The compatibilities of five refractory materials with two process materials from an industrial silicomanganese production furnace were investigated through 12 static crucible tests and two static plate tests at different holding times and temperatures in a specially designed vertical tube furnace. A complete experimental series investigating all 10 slag-refractory combinations was conducted at 1464°C, enabling relative refractory comparison. An operational furnace design was developed, and improvements were suggested for further compatibility testing.

The static crucible test was selected based on simplicity, ease of repeatability and previous experience, while the static plate test was selected based on refractory material properties and reproducibility studies in the literature. Static refractory wear tests provided useful information regarding chemical and structural spalling wear mechanisms, and served as a good starting point for refractory behavior evaluation. Dynamic wear tests will provide additional information regarding wear mechanisms more critical for tap hole refractories, such as thermal stresses and erosion.

SiMn slags were observed to disintegrate ramming paste at 1464°C, and at 1600°C, extensive interaction between SiMn slag I and ramming paste was observed. The investigated ramming paste cannot be recommended for usage during tap block repair in an industrial SiMn furnace.

Incipient electrode paste disintegration by SiMn slags was observed during static plate tests at 1464°C.

SiC tap block showed no significant macroscopic wear, but microscopically, signs of gas formation and slag-refractory interaction were observed within the porous refractory material.

Tap hole clay expanded during heat treatment, but showed minimal interaction with process materials at 1464°C.

C tap block showed minimal signs of interaction with process materials at 1464°C.

Refractory wear mechanisms were identified as:

- Dissolution of refractory matrix due to solubility of oxide binder phases in SiMn slags.
- Disintegration of refractory particles due to gas formation at slag-refractory interface, or expansion as a result of phase transformations in refractory material.
- Direct reduction of MnO from slags and Fe_2O_3 present in refractories by C and SiC.

Establishment of partial slag-metal equilibriums between Fe_2O_3 and Si originally present in slag was observed, as well as formation of SiC at the slag-refractory interfaces. The latter can serve to protect the refractory material upon formation of a continuous SiC layer.

Refractory porosity seemed to have a larger effect on refractory wear than ash content. Contrary to industrial observations, SiMn slag I was more corrosive than SiMn slag II.

Uncertainties in temperature measurements were quantified utilizing the wire-bridge method. Holding temperatures were accurate within ± 1.8°C at 1367°C, ± 2.1°C at 1464°C and - 0.6°C/ + 0.2°C at 1600°C. An uncertainty of ± 2 % must be tolerated for inside diameter measurements. For increased sensitivity during quantification of macroscopic refractory wear, utilization of more accurate technology should be explored.

7. Further work

Upon completion of this investigation, several issues can still be explored increasing the knowledge on refractory-process material interaction in the tap hole area of a SiMn production furnace:

In order to provide more realistic refractory wear results under industrial conditions, slag-refractory interaction should be investigated at industrial tapping temperatures. As observed during this investigation, non-conclusive results were produced at 1464°C for SiC tap block and electrode paste, so investigating these two refractories further at industrial conditions would be of high interest. Also, since incomplete slag melting was experienced during tap hole clay experiments, increased interaction is expected at industrial tapping temperatures, possibly revealing critical refractory wear.

This study proved that the ramming paste investigated interacted with SiMn slags at 1464°C and 1600°C. A detailed investigation of several different types of ramming paste would be of interest in order to confirm the results of this investigation, as well as find a suitable ramming paste replacing the current.

The effects of oxygen lancing could be investigated through a series of experiments where refractories are oxidized in a muffle furnace before conducting compatibility tests[37]. As described in Chapter 2.2.2, it is believed that lancing damages the refractory materials increasing the susceptibility to wear by process materials. Exposing the refractories to oxidizing conditions for different lengths of time can possibly visualize the time effects of lancing.

In a combined tap hole, metal is tapped before slag, exposing the refractories to the effects of several process materials during one tap. Studying metal-refractory interaction would therefore also be of interest, since metals unsatured in C can interact with C particles in refractories. Refractory-refractory interaction could also be investigated for completeness.

Static refractory wear tests should be followed by dynamic wear tests investigating erosion wear mechanisms. As discussed in Chapter 5.4, this would be more relevant for the tap hole refractories, since static conditions are not valid during tapping. Even though C-based refractories are known to have good thermal properties, investigating the effects of thermal stresses through establishment of a temperature gradient in the refractory would also be of interest.

For future studies, a different furnace design allowing for rapid heating and sample quenching should be utilized. This way, reactions taking place during heating and cooling are minimized, and it can be concluded with more certainty that observed interaction took place during holding time at maximum temperature. Shorter experimental times will also be achieved, allowing for conduction of more experiments, possibly repeating each refractory-process material combination two or three times. This serves to rule out random errors, providing increased scientific background for well-founded conclusions.

References

1. Olsen, S. E., Tangstad, M., Lindstad, T., *Production of Manganese Ferroalloys*, SINTEF and Tapir Academic Press, Trondheim, 2007
2. Olsen, S. E., Tangstad, M., *Silicomanganese production - process understanding*, In Proceedings of the Tenth International Ferroalloys Congress*; INFACON X*, Cape Town, South Africa, 2004, pp. 231 - 238
3. *IMnI Production Estimates by Region*, International Manganese Institute, Paris, 2008
4. Hloben, P., *Refractory Materials - Major industrial applications*, Rexxon Corporation, Bryanston, South Africa, 2000
5. Duncanson, P. L., Toth, J. D., *The truths and myths of freeze lining technology for submerged arc furnaces*, In Proceedings of the Tenth International Ferroalloys Congress; INFACON X, Cape Town, South Africa, 2004, pp. 488 - 499
6. Hancock, J. D., *Practical refractories*, Cannon & Hancock cc, Vereeniging, South Africa, 2006
7. Dunkl, M., *Corrosion tests - A very important investigation method for the selection of refractories for glass tanks*, Glass Science and Technology: International Journal of the German Society of Glass Technology, 1994, *67* (12), pp. 325 - 334
8. Lee, W. E., Zhang, S., *Melt corrosion of oxide and oxide-carbon refractories*, International Materials Review, 1999, *44* (3), pp. 77 - 104
9. Craig, J. R., Vaughan, D. J., Skinner, B. J., *Resources of the Earth*, 3rd edition, Prentice Hall, New York, 2001
10. Institute, I. M., http://www.manganese.org/about_mn/ (accessed 16.02.11 09:30)
11. Hayes, P., *Process Principles in Minerals & Materials Production*, Third ed., Hayes Publishing CO, Brisbane, 2003
12. *Lecture notes in TMT4305 Elektrisk reduksjonssmelting*, NTNU, Trondheim, 2009
13. Gous, J., Personal communication - Transalloys, Pretoria, 2011
14. Allibert, M., Gaye, H., Geiseler, J., Janke, D., Keene, B. J., Kirner, D., Kowalski, M., Lehmann, J., Mills, K. C., Neuschütz, D., Parra, R., Saint-Jours, C., Spencer, P. J., Susa, M., Tmar, M., Woermann, E., *Slag atlas*, 2nd ed., Verlag Stahleisen, Düsseldorf, 1995
15. Matyas, A. G., Francki, R. C., Donaldson, K. M., Wasmund, B., *Application of new technology in the design of high-power electric smelting furnaces*, CIM Bulletin, 1993, *86* (972), pp. 92 - 99
16. Steenkamp, J., *PhD research proposal: Formation and maintenance of freeze linings in manganese ferroalloy production furnaces*, University of Pretoria, Pretoria, 2010
17. Steenkamp, J., *Presentation - Aspects influencing taphole life in manganese ferroalloys smelters*, University of Pretoria, Pretoria, 2010
18. Coetzee, C., Duncanson, P. L., Sylven, P., *Campaign Extensions for Ferroalloy Furnaces with improved Taphole Repair System*, In Proceedings of the Twelfth International Ferroalloys Congress*;*INFACON XII, Helsinki, Finland, 2010
19. Chesters, J. H., *Refractories - production and properties*, The Iron and Steel Institute, London, 1973
20. Tomala, J., Basista, S, *Micropore carbon furnace lining*, In Proceedings of the Eleventh International Ferroalloys Congress; INFACON XI, New Delhi, India, 2007
21. Levich, V. G., *Physicochemical hydrodynamics*, Prentice-Hall, Englewood Cliffs, NJ, 1962

22. Silva, S. N., Vernilli, F., Justus, S. M., Marques, O. R., Mazine, A., Baldo, J. B., Longo, E., Varela, J. A., *Wear mechanism for blast furnace hearth refractory lining*, Ironmaking and Steelmaking, 2005, *32* (6), pp. 459 - 467
23. Schei, A., Tuset, J. K., Tveit, H., *Production of High Silicon Alloys*, Tapir akademisk forlag, Trondheim, 1998
24. Mills, K., *The estimation of slag properties*, In Proceedings of the South African Pyrometallurgy Conference, Muldersdrift, South Africa, 2011
25. Tang, K., Tangstad, M., *Modeling viscosities of ferromanganese slag*, In Proceedings of the Eleventh International Ferroalloy Congress; INFACON XI, New Delhi, India, 2007
26. Tangstad, M., Safarian, J., *Compendium: New solar grade silicon production processes*, NTNU, Trondheim, 2008
27. Urbain, G., *Viscosity estimation of slags*, Steel Research, 1987, *58* (3), pp. 111 - 116
28. Riboud, P. V., Roux, Y., Lucas, L. D., Gaye, H., Fachber. Huttenprax. Metallweiterverarb., 1981, *19*, pp. 859 - 869
29. International, A., *Standard Test Method for Isothermal Corrosion Resistance of Refractories to Molten Glass*, ASTM International, West Conshohocken, Pennsylvania, 2009
30. International, A., *Standard Practice for Rotary Slag Testing of Refractory Materials*, ASTM International, West Conshohocken, Pennsylvania, 2009
31. International, A., *Standard Test Method for Disintegration of Refractories in an Atmosphere of Carbon Monoxide*, ASTM International, West Conshohocken, Pennsylvania, 2009
32. Bale, C. W., Pelton, A. D., Thompson, W. T., Eriksson, G., Hack, K., Chartrand, P., Decterov, S., Jung, I.-H., Melancon, J., Petersen, S., *FactSage(TM) version 6.2*, Thermfact and GTT-Technologies, 1976 - 2010
33. Mesures, B. I. D. P. E., *Melting Points of Gold (1064°C), Palladium (1555°C), and Platinum (1768°C) by the Wire-Bridge Method* , In *Techniques for Approximating the International Temperature Scale of 1990*, Organisation intergouvernementale de la Convention du Mètre, Sèvres, 1997, pp. 36-37
34. Crovini, L., Perissi, R., Andrews, J. W., Brookes, C., Neubert, W., Bloembergen, P., Voyer, G., Wessel, I., *Intercomparison of Platinum Thermocouple Calibrations*, High Temperatures - High Pressures, 1987, *19*, pp.179 - 194
35. Aylward, G., Findlay, T., *SI Chemical Data*, 5th ed., Wiley, 2002
36. de Villiers, J. P. R., Personal communication, 2011
37. Tangstad, M., Personal communication, 2011
38. Pistorius, C., Personal communication, 2011
39. Park, J. H., Park, J. G., Min, D. J., Lee, Y. E., Kang, Y.-B., *In situ observation of the dissolution phenomena of SiC particle in CaO-SiO_2-MnO slag*, Journal of European Ceramic Society, 2010, *30*, pp. 3181 - 3186
40. Sanz, J., González-Carreño, T., Gancedo, R., *On Dehydroxylation Mechanisms of a Biotite in Vacuo and in Oxygen*, Physics and Chemistry of Minerals, 1983, *9*, pp. 14 - 18
41. mindat.org, *Vermiculite*, http://www.mindat.org/min-4170.html (accessed 17.06.11)
42. De Yoreo, J. J., Vekilov, P. G., *Principles of Crystal Nucleation and Growth*, Reviews in Mineralogy and Geochemistry, 2003, *54* (1), pp. 57-93
43. Turkdogan, E. T., *Chapter 1* In *Physical Chemistry of High Temperature Technology*, Academic Press, New York, 1980
44. Davidsen, J., *Formation of Silicon Carbide in the Silicomanganese Process*, NTNU, Trondheim, 2011

45. Bassett, W. A., *The Geology of Vermiculite Occurences*, In Proceedings of the Tenth National Conference on Clays and Clay Minerals, Austin, TX, USA, 1961
46. Cromarty, R., Personal communication, 2011
47. Parry, G., Personal communication, 2010
48. Mølnås, H., *Investigation of remelting off grade material in the silicon process*, NTNU, Trondheim, 2011
49. N.I.S.T. Revised Thermocouple Reference Tables, http://www.omega.com/temperature/z/pdf/z212-213.pdf (accessed 07.06.11)
50. Liptak, B. G., *Ch. 4.13 - Thermocouples* In *Instrument Engineer's handbook - Process measurement & analysis*, 4th ed., CRC Press, 2003, pp. 673 - 696
51. N.I.S.T. ITS-90 Table for type R thermocouple, http://srdata.nist.gov/its90/download/type_r.tab (accessed 07.06.11)
52. *Tolerance graphs for thermocouples*, WIKA INSTRUMENTS, Johannesburg, 2001
53. Steenkamp, J., Personal communication, 2011
54. Peterson, B., *Pyrometric Cones*, http://pottery.about.com/od/temperatureclayglazes/tp/pyrocones.htm (accessed 07.06.11)
55. Kim, Y.-G., Gam, K. S., Kang, K. H., *A nickel freezing-point cell for thermocouple calibration*, Metrologia, 2001, *39*, pp. 319 - 323
56. Yamada, Y., Sakuma, F., Ono., A., *Short communication: Thermocouple observation of melting and freezing plateaus for metal-carbon eutectics between the copper and palladium points*, Metrologia, 2000, *37*, pp. 71 - 73
57. MINTEQ, *LaCam® Refractory Lining Measuring System for Electric Arc Furnaces*, http://www.minteq.com/our-products/iron-steel/electric-arc-furnace-products/lacam-for-eaf/ (accessed 08.06.11)
58. Steenkamp, J., *Carbolite PVT 18/80 vertical tube furnace*, University of Pretoria, Pretoria, 2009

Appendices

Appendix A.1: ***Supporting diagrams***

Figure A.1 shows the Ellingham diagram and Figure A.2 shows the MnO-SiO_2 binary phase diagram at low p_{O2}.

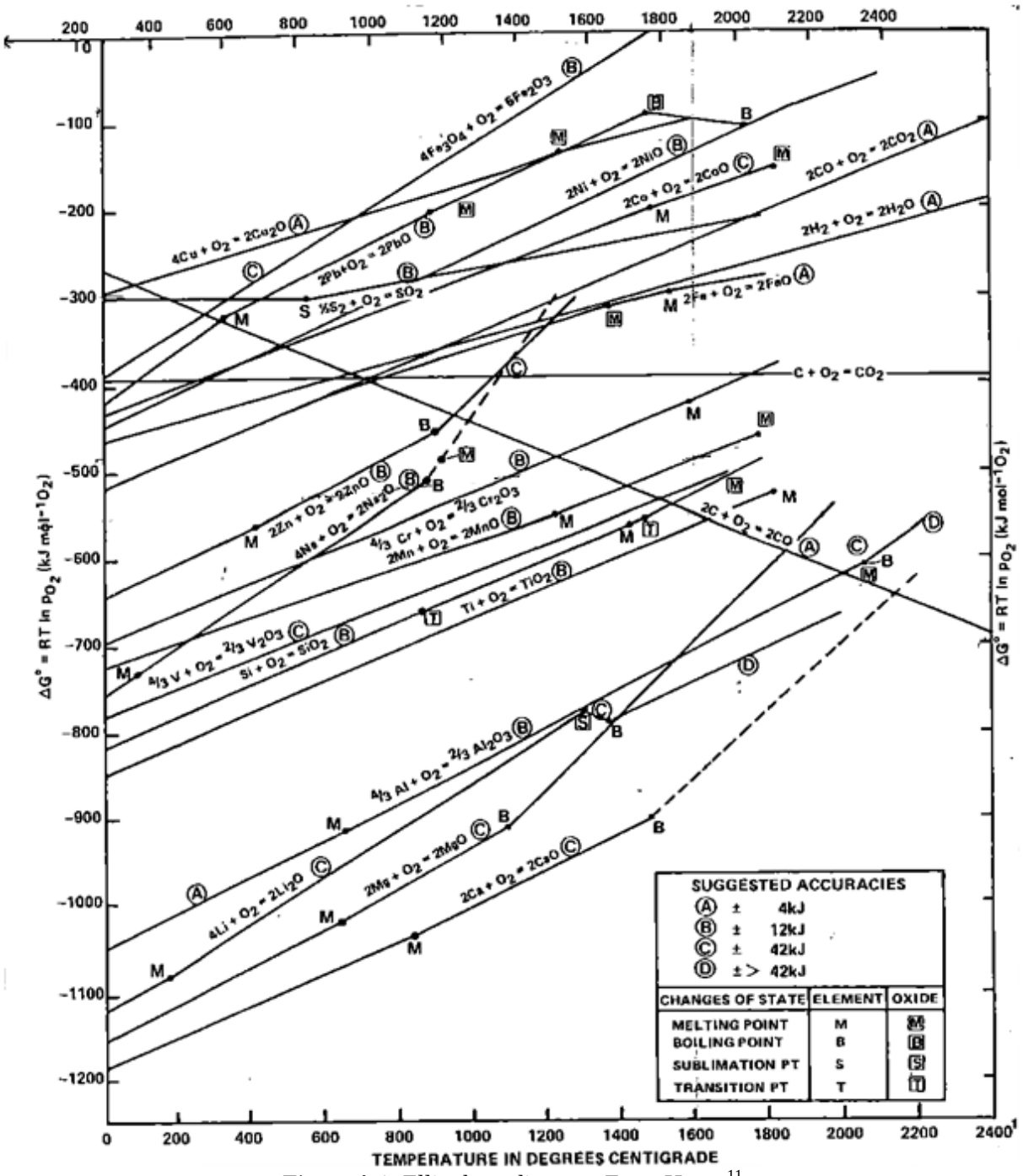

Figure A.1: Ellingham diagram. From Hayes[11]

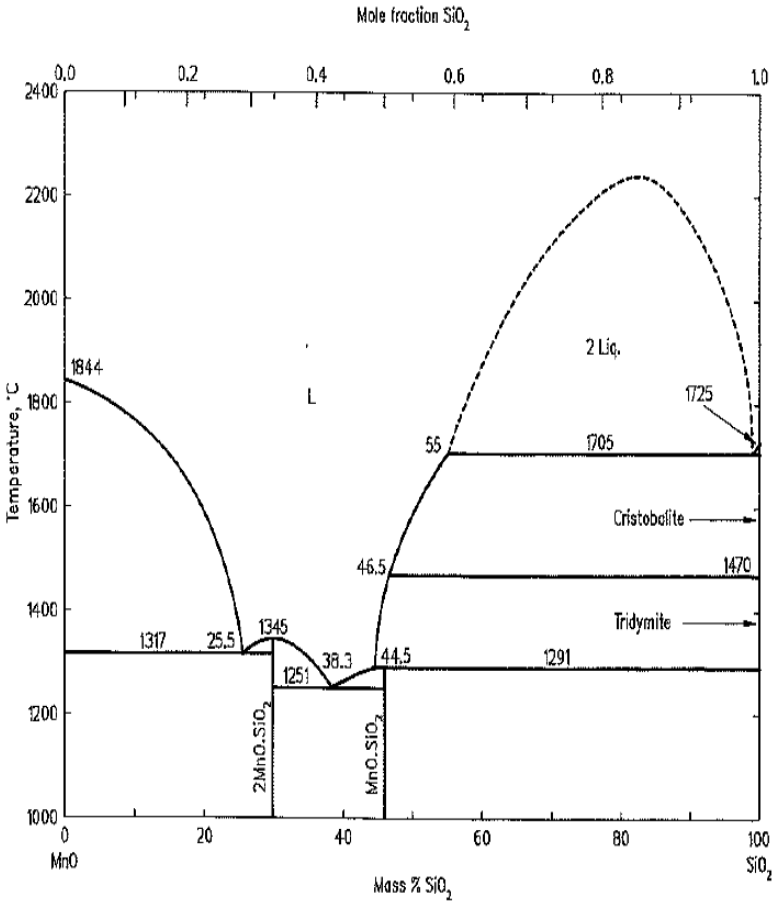

Figure A.2: MnO-SiO_2 phase diagram at low p_{O2}. From Allibert et al.[14]

Appendix A.2: ***Carbolite PVT 18/80 vertical tube furnace***

Figure A.3 shows a principle drawing of the Carbolite PVT 18/80 vertical tube furnace utilized during this investigation. Figures A.4 through A.7 visualize furnace tube fittings design described on the two following pages.

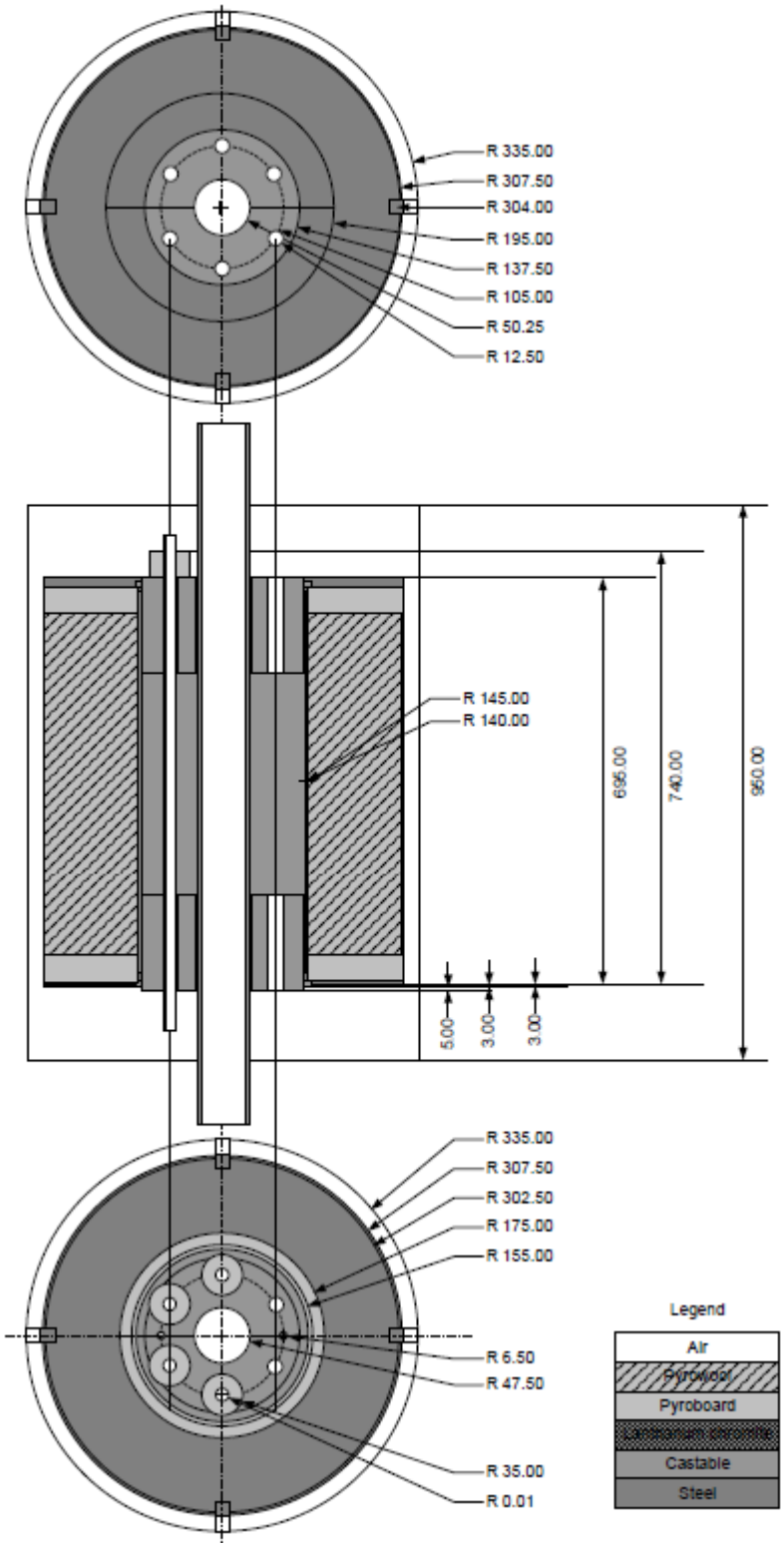

Figure A.3 Principle drawing of Carbolite PVT 18/80 vertical tube furnace. From Steenkamp[58]

Top furnace tube fittings:

Material: Brass

Thickness: 10 mm

Work drawing:

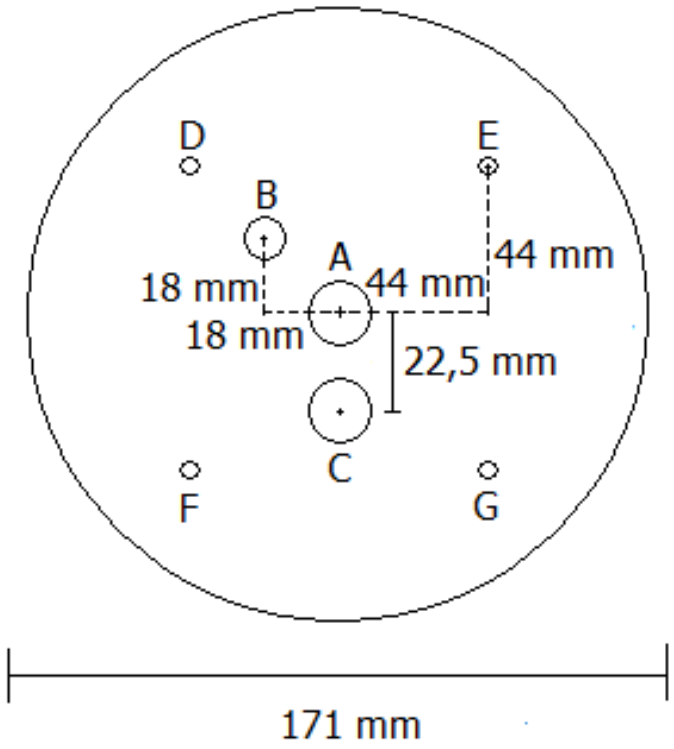

Figure A.4: Top furnace tube fittings

Description: Circular brass plate (diameter 171 mm, or next standard size up) with 7 holes.

Hole A:	Center. Hole diameter 10.5 mm, 3 mm deep indentation 12.4 mm in diameter. (Visualized in Figure A.5)
Hole B:	Shifted 18 mm to the left and 18 mm up from center. Hole diameter 10 mm.
Hole C:	Shifted 22.5 mm down from center. Hole diameter 8.5 mm, 3 mm deep indentation 10.4 mm in diameter . (Visualized in Figure A.6)
Holes D, E, F, G:	Shifted 44 mm right/left and 44 mm up/down from center. Hole diameter 7 mm. 4 holes will be on a circle 62 mm from center.

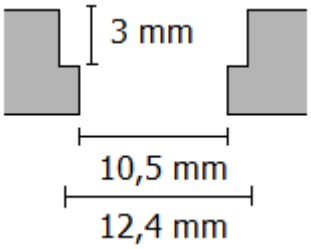

Figure A.5: Hole A

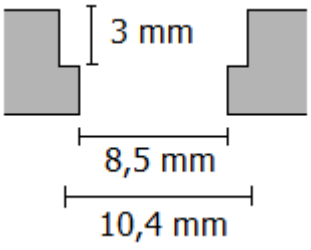

Figure A.6: Hole C

Bottom furnace tube fittings:

Material: Brass

Thickness: 10 mm

Work drawing:

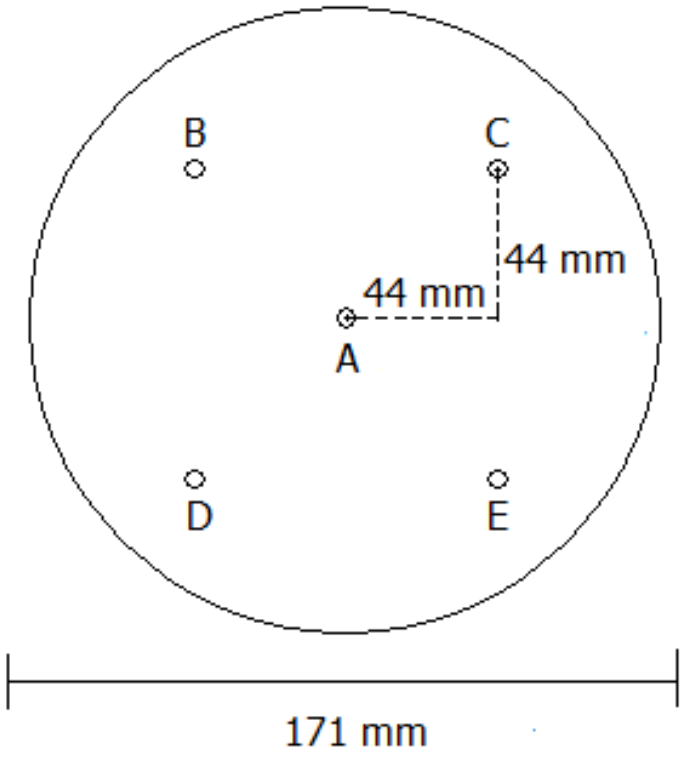

Figure A.7: Bottom furnace tube fittings

Description: Circular brass plate (diameter 171 mm, or next standard size up) with 5 holes.

Hole A:	Center. Hole diameter 6 mm. Threaded NPT thread to fit model swage lock.
Holes B, C, D, E:	Shifted 44 mm right/left and 44 mm up/down from center. Hole diameter 7 mm. 4 holes will be on a circle 62 mm from center.

Appendix A.3: ***Raw material analyses***

Tables A.1 through A.8 present results from raw material analyses. Presence of tungsten carbide in SiC tap block reported in Table A.3 is most likely present from milling.

Table A.1: XRD results for slag compositions

Species	SiMn slag I [wt%]	SiMn slag II [wt%]	SiMn slag III [wt%]	SiMn slag IV [wt%]
Alabandite, MnS	0.87	0.86	1.45	0.9
Augite, $(Ca_{0.61}Na_{0.25}Fe_{0.07}Mg_{0.07})(Mg_{0.65}Fe_{0.10}Al_{0.22})(Si_2O_6)$	-	-	70.44	-
Bustamite, $Ca_{0.228}Mn_{0.772}SiO_3$	-	4.53	3.99	1.54
Enstatite, $Mg_{1.13}Fe_{0.8}Mn_{0.03}Al_{0.14}Si_2O_6$	5.56	-	5.09	3.21
Plagioclase anorthite, $CaAl_2Si_2O_8$	-	-	1.96	3.44
Diopside, $Ca(Mg_{0.5}Al_{0.5})(Al_{0.5}Si_{1.5}O_6)$	3.94	3.34	-	24.69
Moissanite, SiC-3C	2.4	1.84	-	-
Amorphous	87.22	89.43	17.07	66.22
Total	99.99	100.00	100.00	100.00

Table A.2: XRF results for slag compositions

Species	SiMn slag I [wt%]	SiMn slag II [wt%]
SiO_2	40.09	40.07
CaO	21.36	27.79
Al_2O_3	19.91	19.14
MnO	7.37	2.94
MgO	6.55	5.96
BaO	1.50	1.35
SO_3	0.31	0.46
K_2O	0.98	0.81
Na_2O	0.26	0.20
SrO	0.27	0.18
TiO_2	0.23	0.14
Fe_2O_3	0.34	0.11
ZrO_2	0.04	0.05
WO_3	0.05	0.10
MoO_3	0.02	0.01
CeO_2	0.02	0.03
Co_3O_4	0.01	0.02
Y_2O_3	0.01	0.01
S	0.62	0.60
Cl	0.01	0.03
Total	99.94	99.97

Table A.3: XRD results for SiC tap block

Species	SiC [wt%]
Cristobalite, SiO_2 tetragonal	2.97
Quartz, SiO_2 hexagonal	0.91
Moissanite rhombohedral, SiC – 15R	17.21
Moissanite hexagonal, SiC – 4H	12.92
Moissanite hexagonal, SiC – 6H	64.49
Tungsten carbide, WC	1.5
Total	100.00

Table A.4: XRD results for green tap hole clay ash

Species	Taphole clay A [wt%]	Taphole clay B [wt%]
Biotite, $K_{0.78}Na_{0.22}Mg_{1.63}Fe_{0.85}Ti_{0.33}Al_{1.35}Si_{2.84}O_{11}OH$	5.43	-
Chlorite, $(Mg_5Al)(Si, Al)_4O_{10}(OH)_8$	3.82	-
Corundum, Al_2O_3	23.9	-
Kaolinite, $Al_2Si_2O_5(OH)_4$	17.24	31.67
Quartz, SiO_2	49.6	54.17
Muscovite, $(K_{0.727}Na_{0.170}Ca_{0.011})(Al_{0.933}Fe_{0.016}Mg_{0.011})_2(Si_{0.782}Al_{0.221}Ti_{0.005})_4O_{10}(OH)_2$	-	14.16
Total	99.99	100.00

Table A.5: Results from short analyses of C-based refractories

	Ramming paste	Electrode paste	Tap hole clay A	Carbon tap block
Surface moisture [%]	3.15	-	3.60	-
Moisture content, air-dried [%]	2.5	1.0	2.5	0.2
Ash content, air-dried [%]	7.3	4.7	73.8	22.8
Ash content, dry basis [%]	7.5	4.8	75.7	-
Volatile matter content, air-dried [%]	5.9	15.8	9.9	0.8
Volatile matter content, dry basis [%]	6.1	15.9	10.2	-
Calculated fixed carbon, air dried	84.3	78.5	13.8	76.2
% Carbon, LECO	88.9	93.7	23.9	75.7

Table A.6: Results from XRD analyses of ash from C-based refractories

Species	Ramming paste ash [wt%]	Electrode paste ash [wt%]	Tap hole clay ash [wt%]	Carbon tap block ash [wt%]
Anhydrite, $CaSO_4$	13.05	-	-	-
Corundum, Al_2O_3	10.96	8.73	20.28	32.79
Diaoyudaoite, $NaAl_{11}O_{17}$	0.24	-	-	-
Hematite, Fe_2O_3	14.82	20.71	1.46	2.48
Moissanite cubic, SiC-C	12.50	16.96	-	-
Mullite, $Al_6Si_2O_{13}$	13.58	23.34	-	7.33
Quartz, SiO_2	20.53	7.08	77.1	9.69
Cristobalite, SiO_2	-	-	-	39.65
Moissanite hexagonal, SiC-2H	14.32	19.35	-	-
Moissanite rhombohedral, SiC-15R	-	-	-	8.07
Muscovite, $KAl_2(AlSi_3O_{10})(F,OH)_2$	-	3.82	1.15	-
Total	100.00	99.99	99.99	100.01

Table A.7: Results from XRF analyses of ash from tap hole clay

Species	Tap hole clay ash [wt%]
SiO_2	68.20
Al_2O_3	26.05
Fe_2O_3	1.44
K_2O	0.82
SO_3	0.69
TiO_2	0.60
CaO	0.53
ZrO_2	0.46
Na_2O	0.32
MgO	0.25
Cr_2O_3	0.16
WO_3	0.15
P_2O_3	0.08
NiO	0.04
MnO	0.03
V_2O_5	0.03
ZnO	0.03
Co_3O_4	0.03
MoO_3	0.02
BaO	0.01
CuO	0.01
PbO	0.01
HfO_2	0.01
CeO_2	0.01
SrO	0.01
Total	99.98

Table A.8: Results from metal analyses

Species	SiMn metal I [wt%]			SiMn metal II [wt%]		
	A	B	C	A	B	C
Mn	74.64	74.65	74.74	61.66	61.66	61.66
Si	18.20	18.07	18.02	30.26	30.34	30.25
Fe	5.44	5.44	5.44	7.53	7.53	7.51
C	1.27	1.24	1.28	0.0443	0.0566	0.0518
Total	99.55	99.40	99.48	99.49	99.59	99.47

Appendix A.4: ***Crucible/plate design***

Figure A.8 through A.10 show work drawings for manufacture of refractory crucibles and plates:

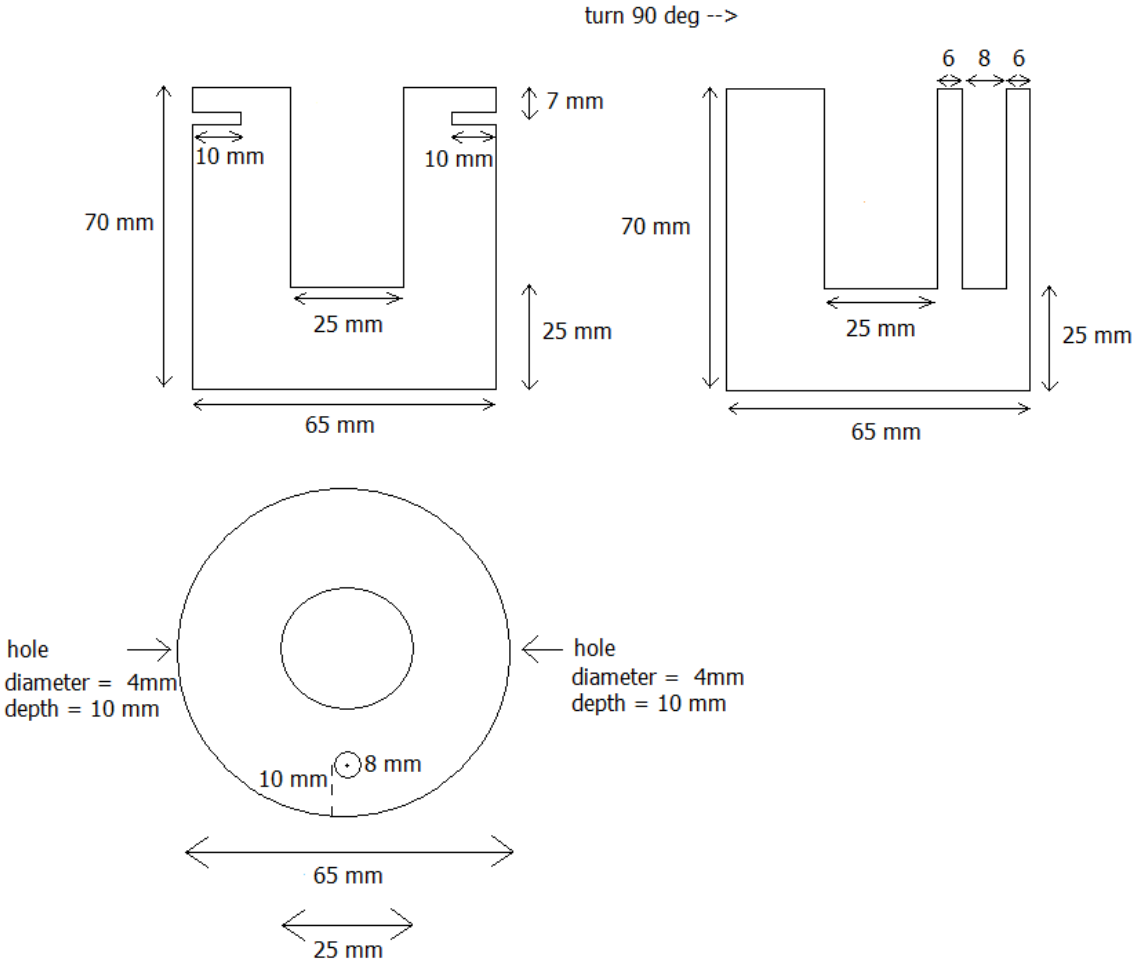

Figure A.8: Work drawing SiC/carbon tap block crucible

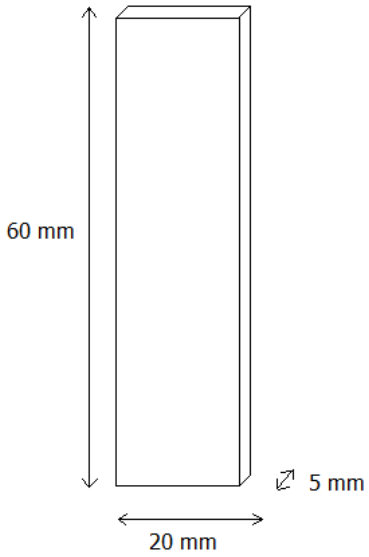

Figure A.9: Work drawing electrode paste plate

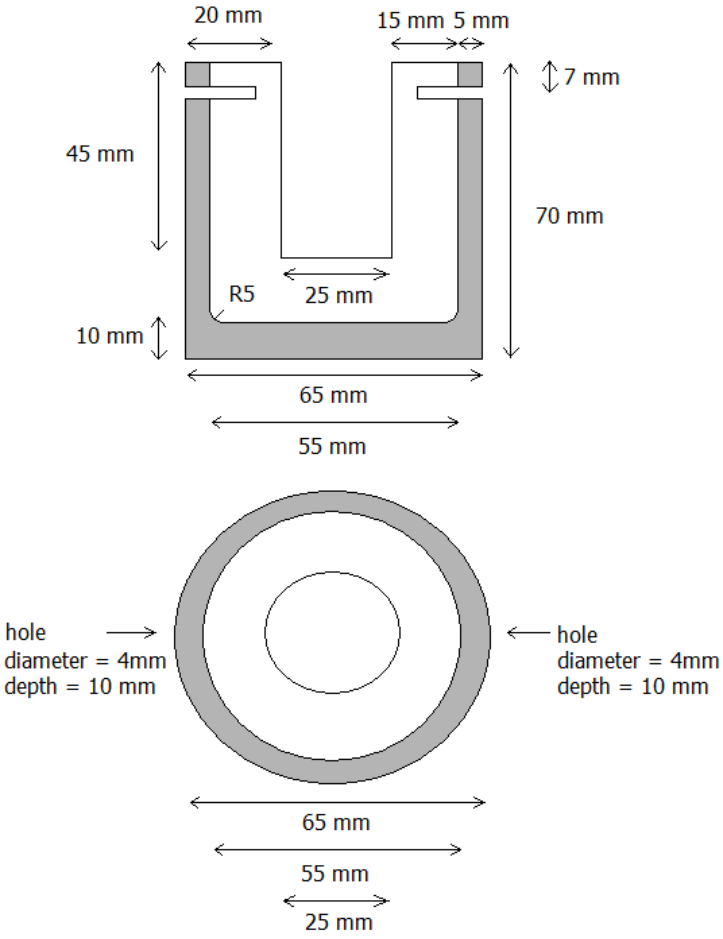

Figure A.10: Work drawing tap hole clay/ramming paste crucible inside graphite shell

Appendix A.5: ***p_{O2} measurements***

Figure A.11 presents p_{O2}-data measured during an experiment holding a ramming paste crucible at 1367°C for 4 hours:

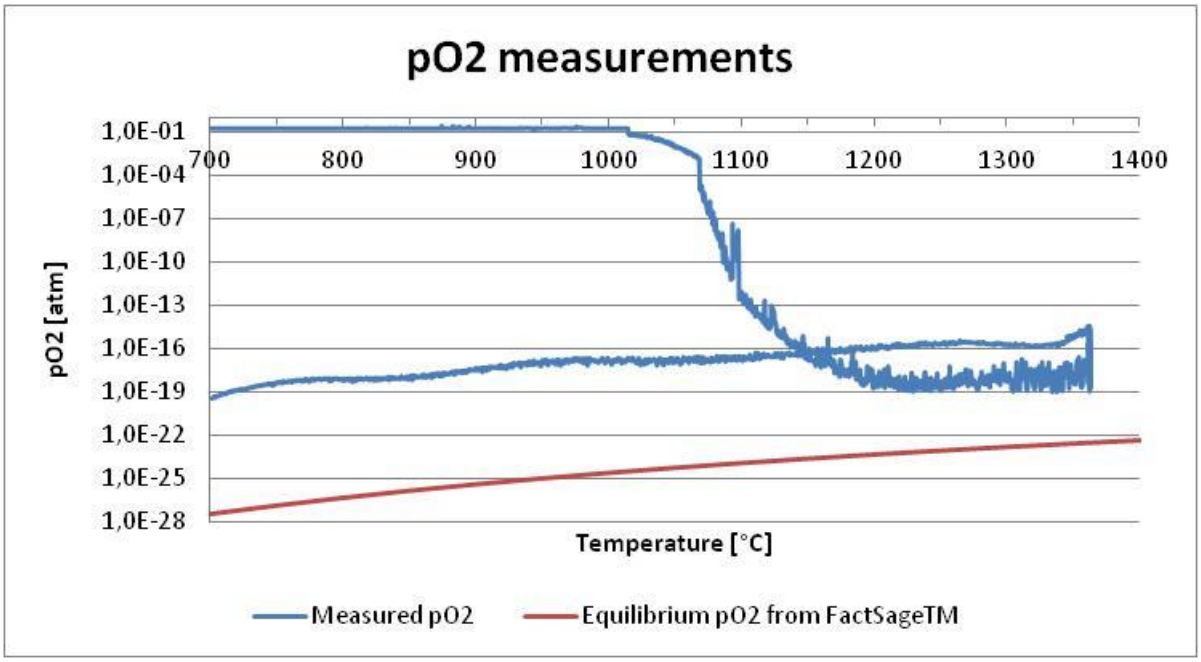

Figure A.11: p_{O2} measurements during ramming paste experiment

The blue curve shows actual p_{O2} measurements during heating, holding and cooling in the accuracy area of the p_{O2} sensor, 700 – 1300°C. Measurements start from the bottom left corner. The sudden rise in p_{O2} upon cooling may be explained through signal wire degradation, or through tube contraction causing air to leak into the system at the bottom tube fittings. A combination of both explanations is most probable.

The red curve indicates equilibrium p_{O2} under the experimental conditions. Equilibrium p_{O2} from reaction (3.1) at 300°C in the gas purifier can be calculated according to equation (A.1) from estimates of Gibbs free energy using Factsage[32], assuming activities of Zr and ZrO_2 equal to unity:

$$Zr(s) + O_2(g) = ZrO_2(s) \tag{3.1}$$

$$K_{eq} = \exp\left[\frac{\Delta G^0}{-RT}\right] = \frac{a_{ZrO_2}}{a_{Zr} \cdot p_{O_2}} \approx \frac{1}{p_{O_2}} \quad \rightarrow \quad p_{O_2,eq} = \frac{1}{\exp\left[\frac{\Delta G^0}{-RT}\right]} \tag{A.1}$$

Since $p_{O2,eq} = 1.08 \times 10^{-90}$ atm, the presence $O_2(g)$ in the input gas can be neglected after the gas purifier. The input gas can therefore be assumed to consist of 99.9% Ar(g), 0.025% CO(g), 0.025% CO_2(g), 0.025% N_2(g) and 0.025% He(g), and equilibrium p_{O2} in the furnace can be estimated using Factsage taking the presence of C(s) into consideration.

Measured p_{O2} in the furnace higher than $p_{O2,eq}$ for equation (3.1) at 300°C indicates that complete equilibrium was not established in the Zr gas purifier.

As observed in Figure A.11, measured p_{O2} values were higher than calculated equilibrium p_{O2} at all temperatures, and oxidation according to equations (A.2), (A.3) and (A.4) was expected:

$$C(s)+\frac{1}{2}O_2(g)=CO(g) \quad \text{(A.2)}$$

$$C(s)+O_2(g)=CO_2(g) \quad \text{(A.3)}$$

$$CO(g)+\frac{1}{2}O_2(g)=CO_2(g) \quad \text{(A.4)}$$

Appendix A.6: ***EDS analyses***

Tables A.9 through A.14 present the results from quantitative EDS analyses of slag and metal prill compositions after the experiments. Compositions are normalized, and must be considered rough estimates of the actual slag and metal compositions. EPMA can provide more accurate quantitative analyses. Due to the thickness of the X-ray detector window, light elements C and O could not be detected using the JSM-6200 Scanning Electron Microscope. Oxide contents of slags were therefore calculated based on the content of elements Al, Ca, Si, Mn, Mg and Fe. Metal prills were expected to contain C not detectable with the equipment utilized during this investigation.

Table A.9: Average bulk slag compositions after experiments

Oxide / Experiment	Al_2O_3 [wt%]	CaO [wt%]	SiO_2 [wt%]	MnO [wt%]	MgO [wt%]	Fe_2O_3 [wt%]	Total [wt%]
SiMn slag I	20.8	22.4	41.9	7.7	6.9	0.3	100.0
C.1	17.4	31.1	42.1	4.2	5.2	0.1	100.1
C.3	16.7	29.7	42.8	4.4	6.3	0.2	100.0
C.5	15.7	30.9	43.6	4.2	5.4	0.3	100.0
C.7	14.9	31.8	43.6	5.3	4.4	0.0	100.0
P.1a)	15.9	31.7	43.2	3.5	5.4	0.1	99.8
SiMn slag II	19.9	29.0	41.8	3.0	6.3	0.1	100.0
C.2	15.2	37.0	40.8	1.6	5.2	0.2	100.0
C.4	15.1	35.4	42.1	2.4	4.9	0.1	99.9
C.6	15.2	35.8	41.2	2.7	4.8	0.3	100.0
C.8	13.7	37.1	43.2	1.6	3.9	0.3	99.9
P.2	15.4	35.8	41.0	2.8	4.9	0.1	100.0

Table A.10: Average slag compositions close to slag-refractory interface after experiments

Oxide / Experiment	Al_2O_3 [wt%]	CaO [wt%]	SiO_2 [wt%]	MnO [wt%]	MgO [wt%]	Fe_2O_3 [wt%]	Total [wt%]
SiMn slag I	20.8	22.4	41.9	7.7	6.9	0.3	100.0
C.1	19.6	30.7	42.5	1.5	5.4	0.0	99.6
C.3	16.3	30.5	43.7	4.3	5.1	0.1	100.0
C.5	15.7	30.9	43.6	4.2	5.4	0.3	100.0
C.7	28.0	23.5	46.8	0.4	1.2	0.3	100.1
P.1a)	17.3	34.9	40.6	1.7	5.5	0.1	100.1
SiMn slag II	19.9	29.0	41.8	3.0	6.3	0.1	100.0
C.2	15.4	38.2	39.3	1.9	5.1	0.1	100.1
C.4	13.9	39.1	42.2	2.0	2.8	0.0	100.0
C.6	13.1	36.9	41.6	1.9	6.3	0.1	100.0
C.8	12.9	33.5	47.7	1.2	4.7	0.0	100.0
P.2	14.7	37.9	40.2	2.4	4.5	0.1	99.9

Table A.11: Average slag compositions after SiC tap block experiments

Oxide / Experiment	Al_2O_3 [wt%]	CaO [wt%]	SiO_2 [wt%]	MnO [wt%]	MgO [wt%]	Fe_2O_3 [wt%]	Total [wt%]
SiMn slag I	20.8	22.4	41.9	7.7	6.9	0.3	100.0
C.3 bulk	16.7	29.7	42.8	4.4	6.3	0.2	100.0
C.3 close to refractory	16.3	30.5	43.7	4.3	5.1	0.1	100.0
C.3 slag-ref. interface	18.4	28.5	45.7	1.3	6.1	0.0	100.0
C.3 far inside refractory	18.5	28.0	46.3	1.0	6.1	0.1	100.0
SiMn slag II	19.9	29.0	41.8	3.0	6.3	0.1	100.0
C.4 bulk	15.1	35.4	42.1	2.4	4.9	0.1	99.9
C.4 close to refractory	13.9	39.1	42.2	2.0	2.8	0.0	100.0
C.4 inside refractory	15.0	35.7	44.1	1.1	3.8	0.2	99.9

Table A.12: Average compositions of large metal prills close to slag-gas interface after experiments

Element / Experiment	Mn [wt%]	Si [wt%]	Fe [wt%]	Total [wt%]
SiMn metal I	76.0	18.4	5.5	100.0
C.1	76.8	17.6	5.5	99.9
C.3	77.5	17.4	5.0	99.9
C.7	80.6	11.1	8.2	99.8
P.1a)	76.7	17.3	5.7	99.7
SiMn metal II	62.0	30.4	7.6	100.0
C.4	44.7	17.9	37.2	99.7
C.6	61.6	14.8	23.4	99.8
C.8	25.0	15.5	59.1	99.6
P.2	74.6	13.4	11.6	99.7

Table A.13: Average compositions of large metal prills close to slag-refractory interface after experiments

Element / Experiment	Mn [wt%]	Si [wt%]	Fe [wt%]	Total [wt%]
SiMn metal I	76.0	18.4	5.5	100.0
C.1	36.0	12.1	51.5	99.6
C.3	53.3	21.2	25.2	99.7
C.5	76.3	17.7	5.9	99.9
C.7	58.4	16.6	24.3	99.3
P.1a)	65.3	16.1	18.3	99.6
SiMn metal II	62.0	30.4	7.6	100.0
C.2	55.2	16.0	28.6	99.8
C.6	71.6	12.3	15.8	99.7
C.8	24.1	14.5	61.1	99.7

Table A.14: Average compositions of small metal prills present inside refractories after experiments

Element / Experiment	Mn [wt%]	Si [wt%]	Fe [wt%]	Total [wt%]
SiMn metal I	76.0	18.4	5.5	100.0
C.1	36.0	12.1	51.5	99.6
C.3	13.8	20.5	65.5	99.8
C.5	80.0	18.3	1.7	100.0
C.7	33.6	14.8	50.6	99.0
P.1a)	82.8	14.1	2.1	99.0
SiMn metal II	62.0	30.4	7.6	100.0
C.2	39.7	16.7	42.7	99.1
C.4	32.2	18.8	48.7	99.7
C.6	73.8	13.4	12.7	99.9
C.8	5.0	15.2	79.5	99.7
P.2	56.4	16.8	26.7	99.9

SiC phases in the slags and on slag-refractory interfaces were identified with a Zeiss Ultra 55 Limited Edition Field Emition SEM at NTNU. Phase compositions are presented in Table A.15:

Table A.15: Average compositions of SiC phases in slags and on slag-refractory interfaces

Element / Experiment	Si [atom%]	C [atom%]	Total [atom%]
C.1	59.0	41.0	100.0
C.2	61.2	37.5	98.7
C.6	54.1	45.5	99.6
P.1a)	62.6	36.1	98.7
P.2	57.7	41.1	98.8

A 50 – 50 atom ratio is expected in SiC, but considering that the EDS measurements only give rough quantitative estimates, it can be assumed that the Si- and C-rich phases observed were SiC. The differences from 100 atom% in samples C.2, C.6, P.1a) and P.2 were detected as tin, Sn, although the peak was most likely the double peak of Si, increasing the Si-content further.